Interactions between water-bodies and atmosphere at regional to global scales

A network analysis and climate modeling approach

D I S S E R T A T I O N

zur Erlangung des akademischen Grades

d o c t o r r e r u m n a t u r a l i u m
(Dr. rer. nat.)
im Fach Physik

eingereicht an der
Mathematisch-Naturwissenschaftlichen Fakultät
der Humboldt-Universität zu Berlin

von
M.Sc.-Phys. Nikoo Ekhtiari

Präsidentin der Humboldt-Universität zu Berlin:
Prof. Dr.-Ing. Dr. Sabine Kunst

Dekan der Mathematisch-Naturwissenschaftlichen Fakultät:
Prof. Dr. Elmar Kulke

Gutachter:

1. Prof. Dr. Dr. h.c. mult. Jürgen Kurths
2. Prof. Dr. Samia Calheiros
3. Dr. Dim Coumou

Tag der mündlichen Prüfung: 29th August 2019

To my beloved sister Minoo, who left me much too early.
1993-2005

Abstract

This dissertation aims at improving our understanding of the mechanisms of interactions between physical processes within the climate system via two different approaches.

In the first part I have studied and utilized climate networks. These networks are a new application of complex networks to study climate variability. They consist of nodes representing the geographical location and links presenting the connections between those geographical locations. Climate networks have been proven to serve as an alternative for data representation, an analysis framework and a visualization tool for understanding the complexity of the Earth's climate system all at once. Among many mechanisms, the mutual interdependence between sea surface temperatures (SST) and precipitation (PCP) has not been completely studied so far in terms of global characteristics and spatial patterns. In this context, the globally most relevant phenomenon is the El Niño Southern Oscillation (ENSO), which strongly affects large-scale SST variability as well as PCP patterns all around the globe. Although significant achievements have been made to improve our understanding of ENSO's global teleconnections and climate impacts, there are many processes associated with ocean-atmosphere interactions in tropics and (extra)tropics, as well as remote effects of SST changes on PCP patterns that have not yet been unveiled or fully understood. Therefore, I have employed the recently introduced framework of coupled climate network analysis for characterizing dominating global co-variability patterns between SST and PCP. My analysis uncovers both local and remote statistical connections and demonstrates their dependence on the current ENSO phase (El Niño, La Niña or neutral phase). Thereby, the results allow identifying teleconnections between SST variations and global precipitation patterns, highlighting the potential of the employed methodology in improving climate variability diagnostics and statistical forecasts in future works. However, this knowledge is limited in terms of the evolution of interactions between SST and PCP. Many climatological processes happen among timescales, so in order to identify and interpret them, I needed to focus on different timescales. Therefore, I have extended the application of coupled climate networks to capture the interdependence between SST and PCP at multi-temporal scales. The results reveal that combining time-scale decomposition by means of a discrete wavelet transform with the concept of coupled climate network analysis unravel the scale-specific connections that are often overlooked at the original resolution of the data. The results show that the strongest correlations between SST and PCP at the scale of 8-16 month concentrate primarily at the Pacific ocean, while the corresponding pattern disappears gradually when increasing the timescale.

In the second part of this thesis, I have focused on simulations with the COnsortium for Small scale MOdeling (COSMO) Climate Limited-area Model (CCLM) and investigate the effects of Lake Sobradinho, a large reservoir in Northeastern Brazil, on the local near-surface atmospheric and boundary layer conditions.

In general, lakes are characterized by an elevated heat capacity and thermal inertia as well as a reduced roughness length and albedo. Therefore, their interaction with the atmospheric surface layer plays a significant role in the

development of meteorological conditions, especially for synoptic scale processes. Despite the importance of considering lakes as a part of numerical weather prediction (NWP) systems, most methods fail to capture their specific interactions with the atmosphere and surrounding land. Either these methods attribute a single value of temperature to the whole water column of the lake (which is simple, but produces large errors in reproducing lake features), or they use turbulence closure models (a better method but computationally very expensive). In this thesis, the FLake model (Freshwater Lake model) is applied for obtaining the lake's vertical temperature profile, as it incorporates much of the essential physics and offers a reasonable compromise between physical realism and computational economy. By including FLake in CCLM, I was able to study Lake Sobradinho, the presence of which has a major effect on the regional climate of in Northeastern Brazil. I have simulated two alternative scenarios: (1) with the lake being replaced by the average normal native vegetation cover and (2) with the lake as it exists today, for two different two-month periods reflecting average and very dry conditions, respectively. The performance of the simulation is compared with data from surface meteorological stations as well as satellite data to ensure the model's ability to capture atmospheric conditions in the vicinity of Lake Sobradinho. The obtained results demonstrate that the lake affects the near-surface air temperature of the surrounding area as well as its humidity and wind patterns. Specifically, Lake Sobradinho cools down the air during the day and warms it during the night by 7 degrees depending on the large-scale meteorological conditions. Moreover, the humidity is significantly increased as a result of the lake's presence and causes a lake breeze. The observed effects on humidity and air temperature also extend over areas relatively far away from the lake. This results show that the FLake model presents important lake effects that otherwise would have been ignored, and leads to a correct interpretation of climate processes within the lake's surroundings.

Zusammenfassung

Ziel dieser Dissertation ist es, mithilfe zweier Herangehensweisen, das Verständnis der Zusammenhänge verschiedener physikalischer Prozesse des Klimasystems zu verbessern.

Im ersten Teil verwende ich Klimanetzwerke, welche eine neue Anwendung komplexer Netzwerke zur Untersuchung der Klimavariabilität darstellen. Solche Netzwerke bestehen aus Knoten, die geografische Positionen repräsentieren, und Kanten, die deren Verbindung beschreiben. Klimanetzwerke wurden nicht nur erfolgreich als eine Alternative für die Repräsentation von Daten verwendet, sondern sind auch in einen mathematischen Rahmen eingebettet und ein Werkzeug zur Visualisierung der Komplexität des Klimasystems der Erde. Von den vielen Mechanismen des Klimasystems wurde die gemeinsame Abhängigkeit von Meeresoberflächentemperaturen (SSTs) und Niederschlägen bisher noch nicht in Hinsicht auf globale Charakteristiken und räumlichen Muster vollständig untersucht. In diesem Kontext ist die El Niño Southern Oscillation (ENSO) das wichtigste Phänomen, welches großskalig SSTs und Niederschläge beeinflusst. In früheren Arbeiten wurden viele Erkenntnisse über ENSOs globale Fernwirkungen und deren Klimaauswirkungen erlangt, jedoch sind die globalen Zusammenhänge von Ozean-Atmosphären-Interaktionen in den (Extra-)Tropen und Fernwirkungen von Meeresoberflächentemperaturänderungen auf Niederschlagsmuster während der verschiedenen ENSO-Phasen nicht kohärent beschrieben. Daher benutze ich die erst kürzlich eingeführten gekoppelten Klimanetzwerke, um die Kovariabilität zwischen Meeresoberflächentemperaturen und Niederschlägen zu charakterisieren. Durch meine Analyse decke ich kurz- und weitreichende Verbindungen auf und zeige deren Abhängigkeit von der jeweiligen ENSO-Phase (El Nino, La Nina, neutrale Phase). Damit erlauben die Ergebnisse Fernwirkungen zwischen Meeresoberflächentemperaturänderungen und globalen Niederschlagsmustern zu identifizieren, was das Potenzial der benutzten Methode zur zukünftigen Verbesserung von Klimaanalysen und statistischen Vorhersagen unterstreicht.

Trotzdem ist das Wissen bezüglich der zeitlichen Entwicklung der Zusammenhänge begrenzt. Viele Klimaprozesse beeinflussen sich auf verschiedenen Zeitskalen, weswegen ich jene beachten muss, um diese Prozesse zu identifizieren, zu verfolgen und zu interpretieren. Daher erweitere ich die Anwendung gekoppelter Klimanetzwerke, um auch die Zusammenhänge zwischen den SSTs und den Niederschlägen erfassen zu können. Die Resultate zeigen, dass die Kombination aus Zeitskalenzerlegung, mithilfe diskreter Wavelet-Transformation, und gekoppelten Klimanetzwerken skalenspezifische Verbindungen, die in der ursprünglichen Repräsentation der Daten nicht sichtbar waren, offenlegen. Die stärksten Korrelationen zwischen den SSTs und den Niederschlägen befinden sich im Pazifischen Ozean mit einer Zeitskalenzerlegung von 8 bis 16 Monaten, während das zugehörige Muster bei Vergrößerung der Zeitskala schrittweise verschwindet.

Im zweiten Teil der Arbeit verwende ich Simulationen des COnsortium for Small scale MOdeling (COSMO) Climate Limited-area Modell (CCLM) und untersuche die Auswirkungen des Sobradinho-Stausees, eines großen Wasserreservoirs im Nordosten Brasiliens, auf die lokalen, bodennahen Atmosphärenschichten und die Grenzschicht. Generell zeigen Seen eine erhöhte Wärmekapazität

und thermische Trägheit als auch eine verringerte Rauigkeitslänge und Albedo. Insbesondere auf synoptischen Zeitskalen ist daher das Zusammenspiel von Seen mit den atmosphärischen Oberflächenschichten ein entscheidender Faktor für die Entwicklung von meteorologischen Verhältnissen. Trotz der Relevanz von Seen für die numerische Wettervorhersage, versagen die meisten Methoden bei der Erfassung der spezifischen Zusammenhänge mit der Atmosphäre und den umliegenden Landmassen. Solche ordnen entweder der gesamten Wassersäule eines Sees einen Temperaturwert zu (und vereinfachen, aber verfälschen Ergebnisse durch die Nichtbeachtung der Seeeigenschaften) oder sie benutzen Turbulenzmodelle (die zwar besser geeignet sind, aber große Rechenleistung benötigen). In dieser Arbeit benutzen wir das Flake Modell (Freshwater Lake model), um das vertikale Temperaturprofil des Sees zu bestimmen, da es die meisten wichtigen physikalischen Vorgänge abbildet und somit einen Kompromiss zwischen physikalischer Realität und Rechenleistung darstellt. Durch die Einbettung des Flake Modells in das CCLM konnte ich den Sobradinho-Stausee untersuchen, der einen großen Einfluss auf das regionale Klima im Nordosten Brasiliens hat. Dabei simuliere ich zwei verschiedene Szenarien: Einerseits ersetze ich den See durch die lokale Durchschnittsvegetation und andererseits analysiere ich den tatsächlichen Zustand, wobei ich für 2-Monats-Perioden jeweils zwei verschiedene klimatische Bedingungen, eine trockene und eine durchschnittliche, teste. Die Simulationsergebnisse verifiziere ich mithilfe meteorologischer Daten von Oberflächen- und Satellitenmessungen, um sicherzugehen, dass die atmosphärischen Verhältnisse in der Nähe des Sobradinho-Stausees richtig abgebildet wurden. Die Ergebnisse zeigen, dass der See sowohl die bodennahe Temperatur als auch Wind- und Luftfeuchtigkeitsmuster der Umgebung beeinflusst. Insbesondere kühlt (erwärmt) der Sobradinho-Stausee die Luft während des Tages (Nacht) um bis zu 7 Grad Celsius, was jeweils durch die großskaligen meteorologischen Verhältnisse moduliert wird. Zudem wird die Luftfeuchtigkeit durch den See erhöht und bewirkt Seewinde. Die Effekte des Sees auf die Luftfeuchtigkeit und -temperaturen beschränken sich nicht nur auf die Nähe des Sees, sondern auch auf relativ weit entfernte Gebiete. Diese Resultate zeigen, dass das FLake Modell wichtige Seeeigenschaften korrekt abbildet, die sonst nicht beachtet werden und kohärent klimatische Prozesse in Seenähe reproduziert.

List of publications

This dissertation is partly based on the following publications. The identifiers, *e.g.*, P1, given below are cited in the text to highlight passages that are connected to one or more of these papers.

Papers

P1 Ekhtiari, N.; Grossman-Clarke, S.; Koch, H.; Meira de Souza, W.; Donner, R.V.; Volkholz, J. Effects of the Lake Sobradinho Reservoir (Northeastern Brazil) on the Regional Climate. *Climate* 2017, 5, 50. doi: 10.3390/*cli*5030050

P2 (In Review) Ekhtiari, N.; Agarwal, A.; Marwan, N.; Donner, R.V. Disentangling the multi-scale effects of sea-surface temperatures on global precipitation: A coupled networks approach.

P3 (In Preparation) Ekhtiari, N.; Ciemer, C.; Kirsch, C; Donner, R.V. Global monthly-scale co-variability patterns between sea-surface temperatures and precipitation in dependence on the ENSO state.

Acknowledgements

I would like to acknowledge everyone who played a role in my academic accomplishments. First of all, my parents, who supported me with love and understanding. Without you, I could never have reached this current level of success. Secondly, I thank Prof. Jürgen Kurths for his support and Reik Donner for providing me the possibility to pursue my research. Last but not least I would like to express my gratitude to my committee members, each of whom has provided patient advice and guidance throughout the research process. Thank you all for your unwavering support.

Contents

List of Figures

List of Tables

List of frequently used mathematical symbols and abbreviations

Mathematical Symbols

V	node
E	link
G	network
τ	length of time series
$X(t)$	a time series
x	a function
N	number of nodes in a network
pc	pearson correlation coefficient
MI	mutual information
ρ_l	link density
k	n.s.i cross-degree
s	link-weighted n.s.i cross degree
$\tilde{M}$	long-term mean
M	number of communities
λ^p	latitudinal position
S	similarity matrix
Tr	threshold
σ	standard deviation
C	covariance matrix
J	total number of scales
$\phi_{J,k}(t)$	approximating wavelet function
$\Psi_{j,k}$	detailed wavelet functions
A	adjacency matrix
W	weighted adjacency matrix
w	weight
δ	kronecker delta
Θ	heaviside step function
ALD	n.s.i cross-average-link-distance
ψ	localized oscillatory function
$\tilde{\alpha}$	average
$\tilde{A}$	average at specific scale and time
λ	scale
t	time

$\tilde{D}$	variation of averages
$\tilde{W}$	wavelet coefficient
ω	a real-valued matrix
$\tilde{V}$	scaling coefficient
$\vec{v}$	velocity vector
$\vec{\Omega}$	three-dimensional angular velocity vector
ρ	density
p	pressure
$\vec{g}$	gravitational acceleration vector
$\vec{f}$	three dimensional friction force
∇	gradient vector in three spatial dimensions
α	specific volume
e	specific internal energy
T	temperature
Q	amount of heat per unit of mass
c_ν	specific heat at constant volume
$\vec{V_g}$	geostrophic wind
$\bar{p}$	standard pressure
ρ_w	water density
θ	temperature of water
ρ_r	maximum density of water
a_T	empirical coefficient
β	buoyancy parameter
Φ_θ	dimensionless function of dimensionless depth
ζ	dimensionless depth
z	depth of water column
h	upper layer of mixed layer depth
D	basin bottom depth
θ_s	temperature of the upper mixed layer
θ_b	bottom temperature
C_θ	shape factor
I	heat flux caused by short-wave radiation
c_w	specific heat of water
Q_s	vertical turbulent heat flux at surface of lake
I_s	heat flux caused by short-wave radiation at surface of lake
Q_b	heat flux through the lake bottom
α_w	albedo of water surface
Q_h	heat flux at the bottom of mixed layer
C_Q	shape factor of heat flux
$C_{\theta\theta}$	dimensionless parameter
psi	a prognostic variable
μ_i	exponentially decaying coefficient
u	wind component in zonal direction

v	wind component in meridional direction
w	wind component in vertical direction

Abbreviations

EOF	empirical orthogonal functions
PCA	principal component analysis
ENSO	El Niño–Southern Oscillation
SST	sea-surface temperatures
PCP	Precipitation
SLP	sea level pressure
MJO	Madden-Julian Oscillation
NAO	North Atlantic Oscillation
PNA	Pacific-North American pattern
PDO	Pacific Decadal Oscillation
AMO	Atlantic Multidecadal Oscillation
PMM	Pacific Meridional Mode
SAM	Southern Annular Mode
ASL	Amundsen Sea Low
AAO	Antarctic Oscillation
ACC	Antarctic Circumpolar Current
IOD	Indian Ocean Dipole
AEM	Atlantic Equatorial Mode
WES	a feedback loop between surface wind, evaporation and sea surface temperature
IPO	Interdecadal Pacific Oscillation
SOI	Southern Oscillation Index
ITCZ	Intertropical Convergence Zone
SPCZ	South Pacific Convergence Zone
MOC	Meridional Overturning Circulation
STC	Subtropical Cell
DJF	December, January, February
MAM	March, April, May
JJA	June, July, August
SON	September, October, November
EN	El Niño
LN	La Niña
NE	neutral phase
ONI	Oceanic Niño Index
n.s.i	node-splitting-invariant
MODWT	maximal overlapping discrete wavelet transform
DWT	discrete wavelet transform
CWT	continuous wavelet transform
NWP	numerical weather prediction
COSMO	COnsortium for Small scale MOdeling

CCLM	Climate Limited-area Model
FLake	Freshwater Lake model
CORDEX	COordinated Regional climate Downscaling EXperiment
RAM	regional climate model
RAMS	Regional Atmospheric Modeling System
RCM	regional climate model
GCM	global climate model
LAM	limited area modeling
LM	Local Model
ANN	artificial neural network
IFS	Integrated Forecasting System
TERRA-ML	multi-layer soil model
BATS	biosphere-atmosphere transfer scheme
FAO	Food and Agriculture Organization of the United Nations
RMSE	root mean square error

Chapter 1.

Introduction

Interactions between water bodies such as oceans or large lake and atmosphere constitute some of the most important couplings in the climate system. Different types of water bodies interact with the atmosphere via various types of energy fluxes and thereby exchange heat via conduction and convection [Woolnough et al., 2001]. In this thesis, specifically, I focus on two different types of water bodies, oceans and lakes and investigate their interactions with the atmosphere on global and regional scales via two different approaches, coupled climate networks and regional climate modeling.

Ocean-atmosphere interaction plays an essential role for explaining various key climate phenomena, ranging from the seasonal cycle characteristics in the tropics over the El Niño–Southern Oscillation (ENSO) to various patterns of decadal-scale climate variability [Alexander et al.,2002, Trenberth and Hurrell, 1994]. Lakes and reservoirs, on the other hand, can affect the regional climate and are equally affected by weather patterns. Lakes interact with the atmosphere by exchanging mass, energy and momentum, despite their small fraction of coverage of the Earth's surface. For instance, regional patterns of atmospheric circulation can be influenced by the variations in heat and moisture transfers between the inland waters and the atmosphere.

To get an overall picture of ocean-atmosphere interaction, I use coupled climate networks, a rather new application of complex system theory in climate. Climate networks have been proven to serve as an alternative for data representation, a proper analysis framework and a visualization tool for unraveling the complexity of the Earth's climate system all at once. By using coupled climate networks, the regions where ocean and atmosphere affect each other statistically are identified. Although in this empirical approach, the exact physical processes that occur between oceans and atmosphere are not explicitly considered, the observed patterns are in good accordance with their possible physical mechanisms. Subsequently, I additionally employ wavelet analysis for studying coupled climate networks, to gain a distinct picture of how ocean-atmosphere interaction patterns appear and disappear during different time scales.

On the other hand, to get an insight into the physical processes coupling water bodies and atmosphere, I use the COnsortium for Small scale MOdeling (COSMO) Climate Limited-area Modell (CCLM), and focus on the Sobradinho Lake in North-eastern Brazil. Although lakes have crucial effects on their surrounding atmosphere

at regional scale, generally, they are not well presented in climate models [Mironov et al., 2008]. To address this issue, I use the FLake model (a parameterization scheme for small to mid-size lakes) within CCLM to evaluate its ability for capturing the regional effects of Sobradinho Lake.

In the following, I will explain both theoretical frameworks in detail and present the corresponding results. Accordingly this thesis divided into two parts, each of which contains several chapters detailing the respective background, methods and results.

Part I.

Complex network analysis of climate variability

Chapter 2.

Introduction

A complex system is as a system with diverse parts that interact with each other. It is usually difficult to model such a complex system due to the large number of dependencies and relationships between the parts or between the system and its environment. Also, several distinct properties can be attributed to complex systems: Non-linearity, diversity, autonomy, adaptation and self-organization are just a few to name. There are several tools that have been developed to study complex systems, such as wavelet analysis [Torrence and Compo, 1998a; Farge, 1992; Weng and Lau, 1994], empirical mode decomposition [Huang et al., 1998], singular spectrum analysis [Ghil et al., 2002; Broomhead and King, 1986; Fraedrich, 1986], or recurrence plots [Eckmann et al., 1987; March et al., 2005; Marwan et al., 2007b]. Furthermore for spatially extended complex systems which are embedded in some metric space, empirical orthogonal functions (EOFs) [Hannachi et al., 2007], spatial recurrence plots [Marwan et al., 2007a, Agustí et al., 2011], and complex networks [Strogatz, 2001; Newman and Park, 2003; Albert and Barabási, 2002a] have been used so far.

In this thesis I mainly focus on climate application of complex networks. These days, networks are widely used as a representation tool of many real-world systems [Boccaletti et al., 2006, Newman, 2003] and have proven to be a successful concept for understanding these systems. Social networks, such as herds of one or more species of animals [Croft et al., 2008 , McGregor, 2005], transportation systems, such as road networks [McGregor, 2005,Kaiser and Hilgetag, 2004], power grids and supply chain networks [Danila et al., 2006, Y.-H. Chen et al., 2010], or neural network [Bullmore and Sporns, 2009a, Sporns et al., 2005] are a few examples of such systems to name. Complex networks are made of nodes and the corresponding links. Each node indicates a single entity in the complex system, like the individual animals or humans in a social network or airports in an airline network. A link, on the other hand, is a way to show the presence of the interactions between the two separate entities. In human social networks, for instance, a link can indicate friendship while in the airline network, it represent a connection between two airports. Complex networks are a powerful tool for representing a complex system, since they provide a methodological framework to study the structure of complex systems [Albert and Barabási, 2002b, Goh et al., 2002, Newman, 2010].

Recently, the complex network approach has been also used in climate studies. The so-called climate networks provide an alternative approach to study climate phenomena [Tsonis and Roebber, 2004, Yamasaki et al., 2008; Donges et al., 2009a,

Steinhaeuser et al., 2010, M. Paluš et al., 2011, Boers et al., 2014b]. In climate networks, the nodes are representing climatic variability at different grid points or measurement sites on the Earth's surface. The links, on the other hand, represent functional interdependencies. These interdependencies can be identified based on different statistical similarity measures. Some popular approaches are the correlation coefficient, [Donges et al., 2009a, Donges et al., 2009b, Paluš et al., 2011] and the synchronous occurrence of extreme events [Stolbova et al., 2014, Boers et al., 2013, Malik et al., 2012, Boers et al., 2015]. Climate networks have been used for studying extreme events [Boers et al., 2014a], to predict a specific climate mode of the variability like the El Niño-Southern Oscillation [Ludescher et al., 2014, Martin et al., 2013], to discriminate between different event types [Wiedermann et al., 2016b; Radebach et al., 2013, Tsonis and Swanson, 2008, Yamasaki et al., 2008] and even to study the temporal evolution of climate processes [Barreiro et al., 2011, Deza et al., 2015, Arizmendi et al., 2014]. Also, climate networks can be used to construct directed links by reconstructing a causal pairwise (or non-pairwise) interactions between different climate processes [Runge et al., 2012a, Runge et al., 2014]. By studying these networks, one can differentiate the relevant interdependencies among the different nodes from potentially misleading effects such as auto-dependencies, common drivers, or indirect couplings [Ebert-Uphoff and Deng, 2012, Runge et al., 2012b, Runge et al., 2015].

Furthermore, climate networks have several advantages in comparison to the widely used methods such as Empirical Orthogonal Functions (EOFs). EOFs are obtained by principal component analysis (PCA) and work as a form of dimensionality reduction to obtain spatial features. Despite the fact that this method can identify the relevant spatial structures, the difficulty of inferring the subset of EOFs for a physical process of interest is a disadvantage of this method. Climate networks are more general and are not restricted to a certain type of similarity matrix to study spatial features of climate data. Also, new insights about the topology of climate networks can be achieved by applying suitable statistics (from graph theory) to them and then using these statistics as a way to interpret climate processes.

So far, most climate network studies have focused solely on the dynamics within a single climatological field or layer. Since the climate system usually incorporates interactions between different physical processes at a wide range of spatial temporal scales, a single climate network cannot give a complete picture of the climate system. Recently, a multivariate extension of this framework has been introduced in terms of so-called interdependent or coupled climate networks, which allows studying the spatio-temporal interdependence patterns among two or more variables from a complex network perspective Donges et al., 2011a; Feng et al., 2012; Wiedermann et al., 2016a. However, a detailed analysis of the multi-scale spatial characteristics of two interdependent climate variables has not yet been provided in the literature.

For instance, ocean-atmosphere coupling is one of the most important aspects of the climate system. Generally, ocean and atmosphere interact via different types of energy fluxes and thereby exchange heat via conduction and convection [Woolnough et al., 2001]. Therefore for explaining various key climate phenomena, ranging from

the seasonal cycle characteristics in the tropics over the El Niño–Southern Oscillation (ENSO) to various patterns of decadal-scale climate variability [Alexander et al., 2002, Trenberth and Hurrell, 1994], ocean-atmosphere coupling plays an essential role. Among many climatological fields that interact with each other, I focus in this thesis on sea-surface temperatures (SST) and precipitation (PCP). The dynamical patterns of SST exchange energy and moisture fluxes from the ocean towards the lower atmosphere which in turn affect pressure and, hence, the circulation pattern, thereby causing emerging spatiotemporal patterns of PCP around the globe [Fedorov, 2008]. In turn, given the multiplicity of known (almost periodic to broad-banded irregular) oscillatory variability modes in different atmospheric and ocean variables from intra-seasonal (e.g., the Madden-Julian Oscillation (MJO)) over inter-annual (e.g., North Atlantic Oscillation (NAO) and ENSO) to multi-decadal scales (e.g., Pacific Decadal Oscillation (PDO) or Atlantic Multidecadal Oscillation (AMO)), it is pivotal to explicitly account for the associated distinct scales in order to unveil potential physical mechanisms explaining the resulting spatial interdependence patterns.

Hence, the aim of the first part of this thesis is the application of coupled climates network to study the co-variability of SST and PCP. I first follow the approaches provided by previous studies for creating a coupled climate network [Donges et al., 2011b, Feng et al., 2012, Tirabassi et al., 2014, Wiedermann et al., 2016a] to perform a systematic study on the effect of the ENSO teleconnections on the co-variability of SST and PCP. I also propose two further measures, for studying the SST-PCP coupled climate network, cross average link distance and cross-community. In the following step, I utilized the discrete wavelet transform to study SST-PCP co-variability at different timescales to gain a more complete picture of their interactions. By combining the wavelet analysis and the coupled climate networks, I incorporate two main aspects of the climate system, namely its multivariate and multi-scale nature, at the same time.

The body of this thesis is organized as follows. Chapter 2 covers the theoretical framework. It is divided into a section on the general theory of complex network construction and another section focus on the construction and utilizing the climate network for studying climatic variabilities. In chapter 3, I present a short overview of the ocean-atmosphere interaction, in order to capture the main idea behind this kind of climatic interaction. Finally, in chapter 4, I present the application of climate networks tool introduced in the previous chapters to study the interactions between the SST and the PCP in the context of multivariate and multi-scale climatic process.

Chapter 3.

Theoretical background

In this chapter, I will introduce the theoretical tools that I have used in the first part of this thesis. Specifically, I explain complex networks and notions that are generally used in studying them. Furthermore, I will mention a few measures associated with the adjacency matrix $\mathbf{A}$ or the weighted adjacency matrix $\mathbf{W}$ in order to study real-world networks. Next, I will introduce climate networks as an application of complex network theory. Moreover I will give a short overview about wavelet analysis, and focus on two types of it, continuous wavelet transform and discrete wavelet transform. Wavelet transforms can be used to decompose a time series into contributions at different scales to study its variation over these scales.

Further methodological details used in each study that go beyond the general theoretical framework of complex networks, climate networks, and wavelet analysis, will be discussed in the respective chapter related to it.

3.1. Complex networks

A network $G = (V, E)$ is based on a set of nodes V that can represent different entities or systems. For instance, nodes can represent intersections in a road network [S. H. Y. Chan et al., 2011], distinct neurons in a neural network [Bullmore and Sporns, 2009b], or simply different geographic locations in a climate network. Different nodes in a system can interact with each other. These interactions can be physical or functional [Costa et al., 2007; Newman, 2003] and can be expressed by link set E.

The adjacency matrix $\mathbf{A}$ of the network G provides a generic representation of its linkage structure. The elements of $\mathbf{A}$ are either 0 or 1. If node i and node j are connected to each other, then $A_{ij} = 1$, otherwise $A_{ij} = 0$. Besides, if the links between the nodes possess no direction, then the network is called an *undirected*. The adjacency matrix $\mathbf{A}$ of an undirected network is symmetric such that: $\mathbf{A} = \mathbf{A}^T$ and $A_{ij} = A_{ji}$. Moreover, a network G can have *self-loops*, such that $A_{ii} = 1$ for $i \in \{1, ..., N_x\}$, where N_x is the number of nodes in the network.

To study the topological characteristics of the network G, several measures can be estimated based on its adjacency matrix $\mathbf{A}$ [Boccaletti et al., 2006]. These measures either refer to each node separately to give an insight of its specific role, or quantify the macroscopic structure of the whole network G.

In many situations it can be beneficial to introduce additional wights to a network. In this regard, there are two types of weights that can be associated with a network.

The first one are weights that characterize each link in the network G. Such weights indicate the strength of the connection between two nodes. In this case, one can study a weighted version of the adjacency matrix $\mathbf{W}$ with $W_{ij} > 0$ if two nodes i and j are connected through a weighted link, and $W_{ij} = 0$ otherwise. The measures for an unweighted network can often be generalized to a link-weighted network by simply replacing the adjacency matrix $\mathbf{A}$ with the weight matrix $\mathbf{W}$ in the corresponding calculations.

A second type of weights is attributed to each node. These weights can, for example, indicate the share of each node on the specific domain of interest [Heitzig et al., 2012; Wiedermann et al., 2013]. The total weights of all the nodes in a network is written as follow:

$$\varpi = \sum_{i \in V} w_i. \tag{3.1}$$

Various measures can be redefined by considering the weights for each node. However, the implementation is not as straightforward as for link-weighted networks. Heitzig et al. (2012) proposed a systematic way to consider a weight for each node and transform an unweighted metrics into their node-weighted versions. These node-weighted metrics are called *node-splitting invariant* (*n.s.i*) metrics and can be defined by applying these four steps:

(a) Sum up weights w_i whenever the unweighted measure counts nodes.

(b) Treat every node $i \in V$ as connected with itself.

(c) Allow equality for i and j wherever the original measure involves a sum over distinct nodes i and j.

(d) "Plug in" n.s.i. versions of measures wherever they are used in the definition of other measures.

The n.s.i metrics are particulary useful for studying networks, in which nodes are distributed inhomogeneously over the domain of the interest.

In the following I will introduce the metrics I used to study the climate networks in this thesis. However, there are a variety of other widly used metrics that can be found in the literature [Albert and Barabási, 2002a; Newman, 2003].

3.1.1. Node degree

The *node degree* k_i measures the total number of the links connected with a certain node i. Mathematically, it is written as follows:

$$k_i = \sum_{j \in V} A_{ij}. \tag{3.2}$$

The node degree k_i is a local measure which is computed individually for each node in the network G. It demonstrates the importance of each node and its function as

a part of the whole network G. For an undirected network without self-loops, the node degree takes an integer value between 0 and $N_x - 1$. The upper limit $N_x - 1$ is for a node that is connected with all the other nodes in the network.

The link-weighted version of the node degree k is obtained by rewriting equation (3.2) as follows:

$$s_i = \sum_{j \in V} W_{ij}. \tag{3.3}$$

s_i is called the strength of node i. A node with a large number of weak connections is considered as important as a node with few but very strong connections.

For the node-weighted version of the node degree k, equation (3.2) is modified as:

$$k_i^* = \sum_{j \in V} w_j A_{ij}^+. \tag{3.4}$$

The $(+)$ sign in the $A_{\bullet\bullet}^+$ indicates that for the node-weighted version of k, self-loops are considered (i.e., step (b) in the section 3.1).

Link and node weights can also be applied simultaneously. The corresponding mathematical form for a node-weighted strength reads as follows:

$$s_i^* = \sum_{j \in V} w_j W_{ij}^+. \tag{3.5}$$

Here, $W_{\bullet\bullet}^+$ is the extended weight matrix taking unto account also self-loops, which is required for node-weight network. Defining the W_{ii} can be challenging. For instance, Zemp et al. (2014) defined W_{ii} based on degree of self-similarity of a node i in a functional network.

3.1.2. Average link distance

The *average link distance* ALD is the average of the geographical distances associated with a node's links in a spherically embedded network. For an undirected and unweighted network, the average link distance ALD is given as follows:

$$ALD_i = \frac{\sum_{j \in V} D_{ij} A_{ij}}{k_i}, \tag{3.6}$$

where D_{ij} is the geographical distance between node i and node j. ALD metric is also a local metric. It indicates whether a node, on average, has short or long distance connections.

One can also introduce the node or link weights into the ALD measure. For instance, for link-weighted networks, equation (3.6) will look as follows:

$$ALD_i^s = \frac{\sum_{j \in V} D_{ij} W_{ij}}{s_i}, \tag{3.7}$$

where $W_{\bullet\bullet}$ are the entries of the weight matrix and $s_{\bullet}$ is the strength of a node as defined in equation (3.3). For a node-weighted network, equation (3.6) can be written as follows:

$$ALD_i^* = \frac{\sum_{j \in V} D_{ij} w_j A_{ij}^+}{k_i^*}, \tag{3.8}$$

where $k_{\bullet}^*$ is the node-weighted degree (n.s.i. node degree) and $A_{\bullet\bullet}^+$ is the extended adjacency matrix of a network with self-loops.

Note again that the (n.s.i) degree and the (n.s.i) average link distance are just two among many other local and global measures that can be used in studying the complex networks [Albert and Barabási, 2002a; Newman, 2003; Boccaletti et al., 2014].

3.2. Coupled networks

In the previous section 3.1, only single networks were considered. However, there are networks which are composed of different single networks (sub-network). Several sub-networks can create a so-called coupled network system and interact with each other. As Donges et al. (2011a) proposed these interactions can be studied through a new framework which is an extension to the single network system.

A coupled network $G = (V, E)$ is defined with a set of the nodes V, the links E and the number of nodes $N = |V|$. The G is composed of several sub-networks $G_n = (V_n, E_{nn})$ each with set of the nodes V_n such that $V = V_1 \cup V_2 \cup V_3 ... \cup V_n$ and $V_1 \cap V_2 \cap V_3 ... \cap V_n = \emptyset$. Also, there are two types of sets of the links associated with G. The first contains the internal links E_{nn} that connect the nodes within each sub-network. The second are the sets of external links or cross-links E_{nm} that connect the nodes among different sub-networks (i.e., $i \in V_n$ and $j \in V_m$) [Donges et al., 2011a]. Likewise, the adjacency matrix $\mathbf{A}$ for a coupled network G consists of adjacency matrices corresponding to each sub-network $\mathbf{A}^n$ (which represent the internal links) and the 'cross'-adjacency matrices $\mathbf{A}^{nm}$ (which represent the external links among two different sub-networks). $\mathbf{A}$ thus has the following form:

$$\mathbf{A} = \begin{pmatrix} \mathbf{A}^1 & \mathbf{A}^{1,2} & \dots & \mathbf{A}^{1,N_G} \\ \mathbf{A}^{2,1} & \mathbf{A}^2 & \dots & \mathbf{A}^{2,N_G} \\ \vdots & \vdots & \ddots & \vdots \\ \mathbf{A}^{N_G,1} & \mathbf{A}^{N_G,2} & \dots & \mathbf{A}^{N_G} \end{pmatrix}. \tag{3.9}$$

Note that for each cross-adjacency matrix $\mathbf{A}^{nm} = (\mathbf{A}^T)_{mn}$ as an analogue to an adjacency matrix for a single network. Also the similar metrics (i.e., see sections 3.1.1 and 3.1.2) can also be adjusted for the coupled networks [Donges et al., 2011a]. Furthermore, the n.s.i version of the metrics for the coupled network can be defiend by implementing the same four steps [Heitzig et al., 2012] that were mentioned earlier

in section 3.1. Here the extension of the n.s.i node degree k^* and the n.s.i average link distance ALD^* for coupled network will be introduced.

We measure the connectivity of each node within one subnetwork with respect to the nodes of the other subnetwork with the n.s.i cross-degree k_i^{m*} [Feng et al., 2012; Donges et al., 2011a]:

$$k_i^{m*} = \sum_{j \in V_m} w_j A_{ij}^{+}. \tag{3.10}$$

Note that in the case of an unweighted cross-degree, equation (3.10) is simply written as follows:

$$k_i^{m} = \sum_{j \in V_m} A_{ij}. \tag{3.11}$$

Once more, the $w_\bullet$ in equation (3.10) is the weight of each specific node and $A_{\bullet\bullet}^{+}$ represents the cross adjacency matrix between two sub-network i and j. Note that k_i^m gives the number of nodes $j \in V_m$ that are connected with the node $i \in V_n$. Similar to the k_i^{m*}, the cross average link distance ALD_i^{m*} measures whether a node in one sub-network is more locally connect to the set of nodes in the other sub-network, or interacts with remote nodes within the other sub-network. With a minor modification of equation (3.8), the n.s.i cross average link distance ALD_i^{m*} can be written as follows:

$$ALD_{i \in V_n}^{m*} = \frac{\sum_{j \in V_m} w_j D_{ij} A_{ij}^{+}}{k_i^{m*}}, \tag{3.12}$$

where D_{ij} is the geographical distance between the nodes $i \in V_n$ and $j \in V_m$.

Throughout this section, I prepared the framework for the following sections and chapters. In the next section 3.3, I will explain the application of complex networks in the context of climate network and the necessary tools for the two follow up studies.

3.3. Climate networks

In this chapter, I will discuss the use of complex networks in climate science [Tsonis et al., 2006; Donges et al., 2009a]. Using the network analysis in the climate science can provide complementary information hidden to classical statistical approaches. In a climate network, the nodes represent geographical locations on or above the Earth surface and associated time series related to a specific climatic variable. The statistical interactions between these time series replaced by the links in the network.

Before constructing a climate network for a specific climate data set, pre-processing is usually required. Next, the statistical inter-dependencies between the different nodes are calculated via similarity measures. At the last step, the adjacency matrix $\mathbf{A}$ (or the weight matrix $\mathbf{W}$) is calculated for the particular climate variable under

the study. Afterwards, by applying the measures such as degree and ALD, the resulting network can be quantitatively studied. Furthermore, one can generalize these steps to two or more climate variables to study their interactions with so-called coupled climate network. In the following, I briefly explain each of those three steps individually.

3.3.1. Data preprocessing

Generally, in order to study a complex system, the available data should be prepared such that they can provide meaningful insights into that specific system. Depending on the type of data, there are different pre-processing methods. In climate, the data should be free from any underlying trends, periodicities or trivial dominant modes [Donner et al., 2017]. Also, it should contain a reasonable amount of information for studying the variability in the climate system. The underlying periodicities such as annual solar cycle or large scale climatic modes usually play a dominant role in climate data and further statistical assessments can therefore get biased. Here, I will focus on climate data with monthly resolution. At a monthly resolution, the annual cycle induces a strong seasonality of the data and overcast the variations at the finer resolutions. Therefore, the annual cycle is better to be removed from the data.

Let us Suppose that there is a time series X associated to a specific climate variable such that for each year, there are $m = 12$ numbers of temporal sampling (monthly scale). In order to remove the seasonality, first the long-term mean for each month (i.e., separately for all Januaries, Februaries and so on) should be calculated as follows:

$$\tilde{M}_m = \frac{1}{N} \sum_{n=1}^{N} x_{m,n}, \tag{3.13}$$

where N is the total number of years and $x_{m,n}$ is the value of X at month m and year n. Then this mean is subtracted from each month:

$$x^*_{m,n} = x_{m,n} - \tilde{M}_m. \tag{3.14}$$

Note that such pre-processing of climate data is not only necessary for the construction of climate networks. Other common methods for studying the climate phenomenon also apply pre-processing methods to obtain a clear picture of the climate's dynamics [Feng and H. Dijkstra, 2013; Handorf and Dethloff, 2012].

The next requirment is related to the spatial distribution of observations points. Due to the sphercal shape of the Earth, the nodes are distributed unevenly such that their density increases toward the poles. This uneven distribution of nodes produces a bias in the resulting network properties since those areas with higher node density overcast the effect of the less dense areas. There are two approaches in order to tackle this problem. One approach is to redistribute the nodes on a sphere with a homogeneous node distance such that the density of the nodes becomes homogeneous [Radebach et al., 2013]. Another approach assigns a weight to each node based on

its spatial share over the Earth surface [Tsonis and Roebber, 2004; Donges et al., 2011a; Feng et al., 2012]. For instance, in areas with a higher amount of the nodes, their associated weights are considered to be small due to a low share of the available space, but in regions with fewer nodes, the weights are larger to account for the larger represented areas. This approach leads to more robust results such that the areas with lower node density will be considered as important as those areas with higher node density. Since I used gridded climate data, I apply the weight for each node [Tsonis et al., 2006; Wiedermann et al., 2016a]. Each weight is related to the node's latitudinal position λ_i on the Earth surface as:

$$w_i = \cos \lambda_i^p. \tag{3.15}$$

3.3.2. Similarity measures

The next step for constructing a climate network is to quantify the statistical dependencies between every each pair of nodes in the system. These calculations lead to an $N_x \times N_x$ similarity matrix $\mathbf{S}$ such that each entry S_{ij} represents the inter-dependency between node i and node j. Depending on the specific application, one can choose between different methods for the corresponding similarity matrix (e.g., Pearson correlation, mutual information, etc). Based on previous studies on climate networks [Donges et al., 2009a; Tsonis et al., 2011; Radebach et al., 2013], considering linear methods such as a pairwise Pearson correlation at zero lag p_{ij} is often sufficient. This measure can be written as follows:

$$pc_{ij} = \frac{\sum_t (X_i(t) - \bar{X}_i)(X_j(t) - \bar{X}_j)}{\sqrt{\sum_t (X_i(t) - \bar{X}_i)^2}\sqrt{\sum_t (X_j(t) - \bar{X}_j)^2}}, \qquad i, j = 1, ..., N_x, \tag{3.16}$$

where $\bar{X}_i$ and $\bar{X}_j$ are the temporal mean values of the time series at each node. Note that, at lag zero, the Pearson correlation coefficient is symmetric so that $pc_{ij} = pc_{ji}$. Therefore, the corresponding similarity matrix $\mathbf{S}$ will be also symmetric, as follows: $\mathbf{S} = \mathbf{S}^T$ ($\mathbf{S}_T$ is the transpose of $\mathbf{S}$).

Moreover, the Pearson correlation coefficients can be either positive or negative. A single climate variable at point i can affect the same variable at point j positively or negatively. Nevertheless, in climate studies, the strongest statistical interactions among climate variables at different places are the goal. Therefore both positive and negative interaction should be considered at the same time. Mathematically, both positive and negative interactions are considered by taking the absolute value of the pairwise correlation coefficients such that:

$$S_{ij} = |pc_{ij}| \,. \tag{3.17}$$

The pairwise Pearson correlation is just one similarity method, which has been used in most of the classical climate studies [Ashok et al., 2007; Handorf and Dethloff, 2012]. However, other similarity measures can also bring new insights into the climate dynamics. For instance, if one prefers to employ nonlinear methods, mutual

information has been proven to be a useful tool to use [Donges et al., 2009b]. Also, for extreme events such as heavy rainfall, event synchronization has been applied as a similarity measure [Boers et al., 2014a; Boers et al., 2013; Boers et al., 2014b]. Moreover, Runge et al. (2012a) developed a novel idea based on quantifying causal pairwise (or non-pairwise) interactions between different climate processes that are represented by directed links. This method is useful to eliminate autocorrelation, indirect couplings, or common drivers [Ebert-Uphoff and Deng, 2012; Kretschmer et al., 2016; Runge et al., 2015].

In the last step of the climate network construction, the matrix of pairwise values of the similarity measure will be converted into an either weighted or unweighted adjacency matrix, $\mathbf{W}$ or $\mathbf{A}$, respectively. Note that studying the similarity matrix directly can cause two main problems. The first issue is that maybe not all the elements of $\mathbf{S}$ are significant. For instance, in the most classical climate studies, it should be proven that a specific interrelations between two points is significant by applying the t-test [Tsonis et al., 2006]. The second issue is that representing all available similarity coefficients as links for the network will produce lots of trivial information. Therefore other interesting patterns within the network can be suppressed. To tackle these two issues, it has been proposed to introduce a global threshold Tr such that only a certain fraction of the strongest absolute correlation coefficients can be represented as links in the network [Tsonis and Roebber, 2004; Tsonis et al., 2006; Donges et al., 2009b]. In another words, only those absolute correlation coefficients which are larger than the threshold Tr are considered as a link between two nodes in the network. Therefore, one can define the adjacency matrix as follows:

$$A_{ij} = \Theta(S_{ij} - Tr)(1 - \delta_{ij}). \tag{3.18}$$

where δ_{ij} represents the Kronecker delta with $\delta_{ij} = 1$ when $i = j$ and $\delta_{ij} = 0$ otherwise and Θ is a step function. In practice, the threshold Tr is obtained by considering the desired link density d and computing the quantile of the entries $S_{\bullet\bullet}$ of the similarity matrix $\mathbf{S}$ based on d. In most climate network studies, the link density d is of the order of 0.01 in order to ensure all the weak and insignificant values of the similarity coefficient are ignored [Donges et al., 2009b; Radebach et al., 2013]. However, defining Tr is not nessecarliy the only solution. For instance, one can consider per-link threshold Tr_{ij} for each link between node i and j. This approach is computationaly expensive since each Tr_{ij} is calculated by comparing the actual S_{ij} with the corresponding values for time series obtained from surrogate data techniques such as Fourier based surrogates [Schreiber and Schmitz, 2000]. This approach can be used when statistical significance of S_{ij} for pairs of time series is crucial [Paluš et al., 2011]. Finally, the corresponding adjacency matrix $\mathbf{A}$ can then be studied by applying the relevant weighted or unweighted network measures as were introduced earlier in the section 3.1.

3.3.3. Coupled climate network

So far, I have discussed climate networks as a representation of a single climate variable. However, climate networks can also be used for studying more than one variable. Donges et al. (2011a) proposed a framework that extends the climate network construction to study the interaction between two different climate variables. In this case, each variable is considered as a sub-network G_n with N_{x_n} nodes as described in section 3.2. This approach is called *coupled climate network* [Donges et al., 2011a; Wiedermann et al., 2016a]. The terminology *coupled climate network* implies that this climate network describes more than one variable and usually does not give any information about the causality or directionality between them.

For the construction of *coupled climate networks*, the similarity measure can be calculated in the same way as described for the single-variable climate network in section 3.3.2. The only difference is that for *coupled climate networks*, there are different sets of links: one E_{nn} describe the interdependencies within each sub-network, while the E_{nm} are associated with the interdependencies among the two different sub-networks G_n and G_m. The similarity matrix of a coupled climate network is the combination of the $N_{x_n} \times N_{x_n}$ similarity matrices $\mathbf{S}_n$ for each variable (sub-network) and the $N_{x_n} \times N_{x_m}$ similarity matrices $\mathbf{S}_{nm}$, which represent the interaction between the two variables (two sub-networks). The $N_x \times N_x$ super-similarity matrix $\mathbf{S}$ is written as follow:

$$\mathbf{S} = \begin{pmatrix} \mathbf{S}^1 & \mathbf{S}^{1,2} & \dots & \mathbf{S}^{1,N_G} \\ \mathbf{S}^{2,1} & \mathbf{S}^2 & \dots & \mathbf{S}^{2,N_G} \\ \vdots & \vdots & \ddots & \vdots \\ \mathbf{S}^{N_G,1} & \mathbf{S}^{N_G,2} & \dots & \mathbf{S}^{N_G} \end{pmatrix}, \tag{3.19}$$

where $N_x = \sum_{n=1}^{N_G} N_{x_n}$. Again, different methods can be used for calculating the similarity matrix depending on the specific application. So far, in previous coupled climate network studies, the Pearson correlation coefficient at lag zero has been used [Donges et al., 2011a; Feng et al., 2012; Wiedermann et al., 2016a]. In order to calculate the cross-correlation between node i in sub-network G_n and node j in sub-network G_m, one can rewrite equation (3.16) as follows:

$$p_{nm,ij} = \frac{\sum_t (X_i(t) - \bar{X}_i)(X_j(t) - \bar{X}_j)}{\sqrt{\sum_t (X_i(t) - \bar{X}_i)^2}\sqrt{\sum_t (X_j(t) - \bar{X}_j)^2}}, \qquad i = 1, ..., N_{x_n}, j = 1, ..., N_{x_m}. \tag{3.20}$$

Considering the strongest correlation between the two variables, the positive and negative $p_{nm,ij}$ are considered simultaneously such that:

$$S_{nm,ij} = |p_{nm,ij}|. \tag{3.21}$$

At last the super-adjacency matrix is created by thresholding separately the *internal* and the *cross*-similarity matrices $\mathbf{S}_n$ and $\mathbf{S}_{nm}$, such that:

$$\mathbf{A} = \begin{pmatrix} \Theta(\mathbf{S}^1 - T_1) & \Theta(\mathbf{S}^{1,2} - T_{1,2}) & \dots & \Theta(\mathbf{S}^{1,N_G} - T_{1,N_G}) \\ \Theta(\mathbf{S}^{2,1} - T_{2,1}) & \Theta(\mathbf{S}^2 - T_2) & \dots & \Theta(\mathbf{S}^{2,N_G} - T_{2,N_G}) \\ \vdots & \vdots & \ddots & \vdots \\ \Theta(\mathbf{S}^{N_G,1} - T_{N_G,1}) & \Theta(\mathbf{S}^{N_G,2} - T_{N_G,2}) & \dots & \Theta(\mathbf{S}^{N_G,N_G} - T_{N_G,N_G}) \end{pmatrix}. \tag{3.22}$$

Note that, the correlations between nodes within one sub-network associated with a climate variable might be naturally stronger than the correlations between the nodes of two different sub-networks. On the other hand, more nodes within one sub-network should be connected with each other than among two sets of nodes from two different sub-networks. Thus, the internal thresholds T_n for each variable and the cross-thresholsd $T_{n,m}$ for two interacting variable are considered based on different values for the internal link densities d_n and the cross-link densities $d_{n,m}$, respectively.

3.4. Wavelet analysis

In this section, I will give a short overview about the mathematical concept of *wavelets* analysis which is widly used in time series analysis. In many cases, the wavelet analysis is a complementary tool to other existing analysis techniques such as correlation and the spectral analysis [Percival and Walden, 2000]. Generally, there are two types of the wavelet analysis. The first one is based on the continuous wavelet transform (CWT). As the name suggests, the CWT is useful for decomposing the time series into a continuous set of scales (frequencies). The second one is called the discrete wavelet analysis (DWT) and it is used to decompose the time series into a discrete set of scales. In Fig. 3.1 three of such wavelets are plotted.

A wavelet is a *localized oscillatory function* $\psi(\bullet)$ (in contarst to a *global oscillatory function* such as sine function [Percival and Walden, 2000]) that grows and decays in a limited time frame and should satisfy two main properties [Percival and Walden, 2000]:

[1]
$$\int_{-\infty}^{\infty} \psi(u)du = 0 \tag{3.23}$$

[2]
$$\int_{-\infty}^{\infty} \psi^2(u)du = 1 \tag{3.24}$$

In the following subsections 3.4.1 and 3.4.2, I will explain the CWT and the DWT, respectively in more detail. Subsequently, in subsection 3.4.3, I will cover an

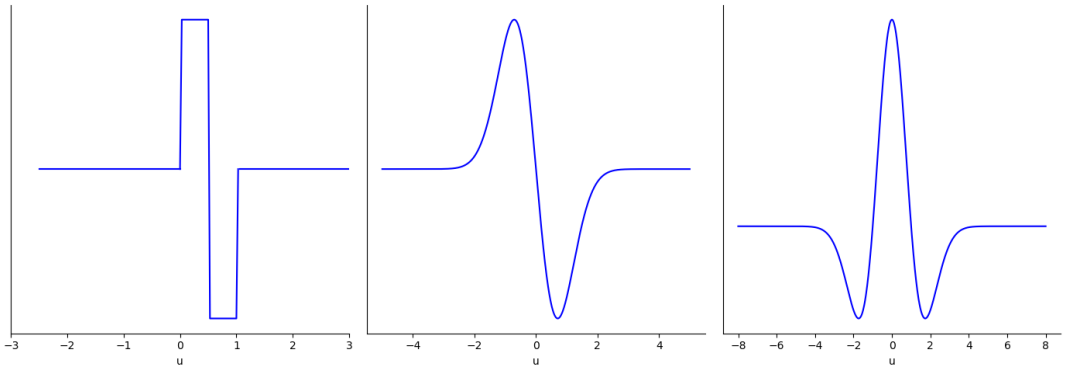

Figure 3.1.: Three example of wavelets. The left one is the Haar wavelet, the middle one is the first derivative of the Gaussian probability density function wavelet and the right one is the Mexican hat wavelet.

extension to the DWT which is called maximum overlap discrete wavelet analysis (MODWT).

3.4.1. Continuous wavelet analysis

As Percival and Walden (2000) explain, wavelet analysis tells us about the variation in the average of a desired function. For instance, for a specific function $x(\bullet)$ which is a real-valued function of an arbitrary independent variable like t, its average over a specific interval $[a, b]$ is calculated as follows:

$$\tilde{\alpha}(a,b) \equiv \frac{1}{b-a}\int_a^b x(u)du. \tag{3.25}$$

If $\lambda = b - a$ and $t = \frac{(a+b)}{2}$, then equation (3.25) can be rewritten as follows:

$$\tilde{A}(\lambda,t) \equiv \tilde{\alpha}(t-\lambda/2, t+\lambda/2) = \frac{1}{\lambda}\int_{t-\lambda/2}^{t+\lambda/2} x(u)du. \tag{3.26}$$

λ is the *scale* which is associated with the length of the interval used for averaging the function $x(\bullet)$ and t is the center of that interval [Percival and Walden, 2000]. Although the average of a specific function within a certain interval is relevant in many applications, studying how such averages fluctuate within a specific scale would provide more information. The variation of these averages can be calculated as follows:

$$\tilde{D}(\lambda,t) \equiv \tilde{A}(\lambda, t+\lambda/2) - \tilde{A}(\lambda, t-\lambda/2) = \frac{1}{\lambda}\int_t^{t+\lambda/2} x(u)du - \frac{1}{\lambda}\int_{t-\lambda/2}^{t} x(u)du. \tag{3.27}$$

Equation (3.27) can be written in the following compact form:

$$\tilde{D}(\lambda, t) = \int_{-\infty}^{\infty} \tilde{\psi}_{\lambda,t}(u)x(u)du, \tag{3.28}$$

where

$$\tilde{\psi}_{\lambda,t}(u) \equiv \begin{cases} -1/\lambda, & t-\lambda < u \leq t; \\ 1/\lambda, & t < u \leq t+\lambda; \\ 0, & \text{otherwise.} \end{cases} \tag{3.29}$$

If $\lambda = 1$ and $t = 0$,

$$\tilde{\psi}_{1,0}(u) \equiv \begin{cases} -1, & -1 < u \leq 0; \\ 1, & 0 < u \leq 1; \\ 0, & \text{otherwise.} \end{cases} \tag{3.30}$$

Equation (3.30) defines the *Haar wavelet function* as $\tilde{\psi}_{1,0}(u) = \sqrt{2}\psi^{(H)}(u)$. Hence, integrating the product of a wavelet function and a specific function can tell us how the averages of this function vary at the desired scale [Percival and Walden, 2000]. For instance, $\int_{-\infty}^{\infty} \psi^{(H)}(u)x(u)du \equiv W^{(H)}(1,0)$ gives the variation in the averages of the function $x(\bullet)$ at unit scale ($\lambda = 1$) with the center at $t = 0$.

By modifying equation (3.30), the changes in the average for the different t is written as follows:

$$\psi_{1,t}^{(H)}(u) \equiv \psi^{(H)}(u-t) \tag{3.31}$$

with:

$$\psi_{1,t}^{(H)}(u) \equiv \begin{cases} -1/\sqrt{2}, & t-1 < u \leq t; \\ 1/\sqrt{2}, & t < u \leq t+1; \\ 0, & \text{otherwise.} \end{cases} \tag{3.32}$$

Equation (3.32) is merely just a shifted version of equation (3.30) and therefore satisfies the two main properties of the wavelet, the integration to zero and the square-integrability to unity, respectively [Percival and Walden, 2000]. The same analysis can be done also for any other desired scale. For instance, by rewriting equation (3.32) as follow:

$$\psi_{\lambda,t}^{(H)}(u) \equiv \frac{1}{\sqrt{\lambda}}\psi^{(H)}\Big(\frac{u-t}{\lambda}\Big) = \begin{cases} -1/\sqrt{2\lambda}, & t-\lambda < u \leq t; \\ 1/\sqrt{2\lambda}, & t < u \leq t+\lambda; \\ 0, & \text{otherwise} \end{cases} \tag{3.33}$$

And therefore:

$$\tilde{W}^{(H)}(\lambda,t) \equiv \int_{-\infty}^{\infty} \psi_{\lambda,t}^{(H)}(u)x(u)du. \tag{3.34}$$

The collection of $\tilde{W}^{(H)}(\lambda,t)$ for t between $(-\infty,\infty)$ is called the Haar continuous wavelet transform (CWT). By analogy, any other wavelet function can be plugged inside equation (3.34) to compute the CWT as:

$$\tilde{W}(\lambda,t) \equiv \int_{-\infty}^{\infty} \psi_{\lambda,t}(u)x(u)du, \tag{3.35}$$

where

$$\psi_{\lambda,t}(u) \equiv \frac{1}{\sqrt{\lambda}}\psi\Big(\frac{u-t}{\lambda}\Big). \tag{3.36}$$

Note that the CWT preserves all information of the function $x(\bullet)$ [Percival and Walden, 2000]. For this we need to consider two more main criteria. First, the wavelet function $\psi(\bullet)$ has to satisfy the *admissibility* condition (i.e., the Fourier transform of $\psi(\cdot)$ obeys $0 < C_\psi \equiv \int_0^\infty \frac{|\Psi(f)|^2}{f} < \infty$) and second, the function $x(\bullet)$ should satisfy the following condition:

$$\int_{-\infty}^{\infty} x^2(t)dt < \infty. \tag{3.37}$$

Then, the function $x(\bullet)$ is recovered from the CWT as follows:

$$x(t) = \frac{1}{C_\psi}\int_0^\infty \Big[\int_{-\infty}^{\infty} \tilde{W}(\lambda,u)\frac{1}{\sqrt{\lambda}}\psi\Big(\frac{t-u}{\lambda}\Big)du\Big]\frac{d\lambda}{\lambda^2}. \tag{3.38}$$

Also note that:

$$\int_{-\infty}^{\infty} x^2(t)dt = \frac{1}{C_\psi}\int_0^\infty \Big[\int_{-\infty}^{\infty} \tilde{W}^2(\lambda,t)dt\Big]\frac{d\lambda}{\lambda^2}. \tag{3.39}$$

The left-hand side of the equation (3.39) is the energy of the function $x(\bullet)$ and the right-hand side $\frac{\tilde{W}^2(\lambda,t)}{\lambda^2}$ is considered as the energy density function. In other words, it shows the energy decomposition of the function $x(\bullet)$ into the different scales and times [Percival and Walden, 2000].

The CWT does not only give a clear picture of how the average and the energy of a specific function behave at the different time scales but also preserves all essential information for reconstructing that function.

3.4.2. Discrete wavelet analysis

Despite the information obtaind via CWT in studying the time series, it also carries a lot of redundancy especially at the larger scales where the average difference

between the two adjacent intervals is insignificant [Percival and Walden, 2000]. As an alternative approach, often the discrete wavelet analysis is preferred.

The DWT mainly preserves all the features of the CWT as explained in the section 3.4.1. However, the main difference is that DWT decompose the time series into a set of discrete scales. Specifically, the DWT produces the $\tilde{W}(\lambda, t)$ only at *dyadic* scales. Hence, λ can get values of 2^{j-1} for $j = 1, 2, 3, ..., J$ and within each scale, the t is chosen to be a multiple of 2^j [Percival and Walden, 2000]. Let us consider $X_n, n = 0, 1, ..., N-1$ to be the nth element of a specific time series. As analog to the CWT, the DWT also produces wavelet coefficients $[\tilde{W}_n : n = 0, ..., N-1]$. Therefore for each n one has $\tilde{W}_n = \omega_n X$ where ω_n is the $N \times N$ real-valued matrix that define the nth DWT and $\omega^T \omega = I_N$. Same as the CWT, W_n^2 in the DWT represents the amount of the energy at a specific scale since: $\left\|\tilde{W}^2\right\| = \|X\|^2$.

For instance for a time series $X(t)$ with $t = 1, ..., 16$, the 16 Haar DWT coefficients can be written as follows [Note that $X_{-1} \equiv X_{15}$, $X_{-2} \equiv X_{14}$ and so on, which is based on the *circularity* assumption. The assumption is used to treat the boundary by considering that the time series is circular.]:

$$\tilde{\mathbf{W}} = \begin{pmatrix} \tilde{W}_0 \\ \vdots \\ \tilde{W}_7 \\ \tilde{W}_8 \\ \vdots \\ \tilde{W}_{11} \\ \tilde{W}_{12} \\ \tilde{W}_{13} \\ \tilde{W}_{14} \\ \tilde{W}_{15} \end{pmatrix} = \begin{pmatrix} \frac{1}{\sqrt{2}}(X_1 - X_0) \\ \vdots \\ \frac{1}{\sqrt{2}}(X_{15} - X_{14}) \\ \frac{1}{2}(X_3 + X_2 - X_1 - X_0) \\ \vdots \\ \frac{1}{2}(X_{15} + X_{14} - X_{13} - X_{12}) \\ \frac{1}{\sqrt{8}}(X_7 + \ldots + X_4 - X_3 - \ldots - X_0) \\ \frac{1}{\sqrt{8}}(X_{15} + \ldots + X_8 - X_7 - \ldots - X_8) \\ \frac{1}{4}(X_{15} + \ldots + X_8 - X_7 - \ldots - X_0) \\ \frac{1}{4}(X_{15} + \ldots + X_0) \end{pmatrix}. \tag{3.40}$$

By defining the means at a specific scale λ over the set of times from $t - \lambda + 1$ to t as follows [Percival and Walden, 2000; Torrence and Compo, 1998b]:

$$\bar{X}_t(\lambda) \equiv \frac{1}{\lambda} \sum_{l=0}^{\lambda-1} X_{t-l}, \tag{3.41}$$

the DWT coefficients can be expressed as:

$$\tilde{W}_0 = \frac{1}{\sqrt{2}}[\bar{X}_1(1) - \bar{X}_0(1)] \quad \ldots \quad \tilde{W}_7 = \frac{1}{\sqrt{2}}[\bar{X}_{15}(1) - \bar{X}_{14}(1)]$$

$$\tilde{W}_8 = \bar{X}_3(2) - \bar{X}_1(2) \quad \ldots \quad \tilde{W}_{11} = \bar{X}_{15}(2) - \bar{X}_{13}(2)$$

$$\tilde{W}_{12} = \sqrt{2}[\bar{X}_7(4) - \bar{X}_3(4)] \quad \ldots \quad \tilde{W}_{13} = \sqrt{2}[\bar{X}_{15}(4) - \bar{X}_{11}(4)]$$

$$\tilde{W}_{14} = 2[\bar{X_{15}}(8) - \bar{X_7}(8)]$$

$$\tilde{W}_{15} = 4\bar{X_{15}}(16)$$

The first 8 coefficients, $\tilde{W}_0, ..., \tilde{W}_7$, show the variation in the adjacent mean of $X(t)$ at a scale of 1 (i.e., $\lambda = 1$). The $\tilde{W}_8, ..., \tilde{W}_{11}$ coefficients are the differences in the averages at the scale of two, the $\tilde{W}_{12}$ and $\tilde{W}_{13}$ coefficients are the differences in the averages at the scale of four, the $\tilde{W}_{14}$ coefficient is the difference in the average at the scale of eight and the last one, the $\tilde{W}_{15}$ coefficient is the average of the whole data. In general, for a time series of length $N = 2^J$, the first $\frac{N}{2}$ DWT coefficients describe the variation of the averages over scale 1, The next $\frac{N}{4}$ coefficients are for scale two and so on until the $\tilde{W}_{N-4}$ and $\tilde{W}_{N-3}$ are associated to the scale $\frac{N}{4}$, $\tilde{W}_{N-2}$ is related to the scale $\frac{N}{2}$ and finally the last one, $\tilde{W}_{N-1}$ is the average of the whole time series [Percival and Walden, 2000]. The last coefficient is called the *scaling coefficient* while the others are called *wavelet coefficients*.

Like the CWT, the DWT also decomposes the energy of a time series into contributions at different scales. Therefore for the above example and considering $\tilde{W}_{j,n}$ as the nth wavelet coefficient at the scale 2^{j-1} and $\tilde{V}_n$ as the nth scaling coefficient, the energy equation can be obtained as:

$$\sum_{t=0}^{16} \|X\|_t^2 = \sum_{j=1}^{4} \left\|\tilde{\mathbf{W}}_j\right\|^2 + \left\|\tilde{\mathbf{V}}_4\right\|^2 \tag{3.42}$$

where

$$\begin{aligned}
\tilde{\mathbf{W}}_1^T &= [\tilde{W}_0, \tilde{W}_1, \tilde{W}_2, \tilde{W}_3, \tilde{W}_4, \tilde{W}_5, \tilde{W}_6, \tilde{W}_7] \\
\tilde{\mathbf{W}}_2^T &= [\tilde{W}_8, \tilde{W}_9, \tilde{W}_{10}, \tilde{W}_{11}] \\
\tilde{\mathbf{W}}_3^T &= [\tilde{W}_{12}, \tilde{W}_{13}] \\
\tilde{\mathbf{W}}_4^T &= [\tilde{W}_{14}] \\
\tilde{\mathbf{W}}_4^T &= [\tilde{W}_{15}]
\end{aligned} \tag{3.43}$$

Note that in the DWT the scale λ has a unitless value. However, for real data which has δt as an interval between the sampling points, the specific scale will be redefined as $\lambda \delta T$, which has a meaningful physical unit.

3.4.3. Maximum overlap discrete wavelet analysis

The MODWT is an extension to the DWT [Percival, 2008]. It also analyses the time series within *dyadic* scales, but in contrast to the DWT, all t are considered instead of only the multiples of $2^j t$. For the MODWT, at each scale, N wavelet coefficients are produced. Therefore the total number of coefficients are $(J + 1)N$. The J sets of coefficients are the *wavelet coefficients* and the rest the *scaling coefficients*. By considering all possible t, the MODWT creates a suitable summary of the CWT and

removes the *alignment* artifact that is normally attributed to the DWT [Percival and Walden, 2000]. The *alignment* artifact means that the DWT is sensitive to a time shift. If the DWT were shift invariant, it would preserve the initial time shift in the original time series. In contrary, the original shift distance is not preserved through different scales and varies in an unpredictable way [Maheswaran and Khosa, 2012].

3.5. Summery

In this chapter, I covered the main framework for the construction of climate networks for a single variable and also more than one variable. I also gave a short overview about wavelet analysis and how it can be implemented to decompose a certain time series into the several desirable scales. Having this theoretical background, in the following chapter 3,I will briefly give a short overview of one of the main climatic interaction mechanisms the so-called ocean-atmosphere interaction. Then, in the chapter 5, I will use the presented framework to study the ocean-atmosphere interaction through coupled climate networks and wavelet analysis.

Chapter 4.

Ocean–atmosphere interaction: An overview

The Sun is the main source of energy for the Earth. This energy reaches the Earth in the form of short-wave radiation (light). The Earth surface mostly absorbs this radiation and further emits long-wave radiation (heat) into the atmosphere. The incoming radiation from the Sun is distributed differently over the latitudes on the Earth's surface. In other words, due to the tilt of the Earth's axis, its shape, atmosphere, clouds, polar ice and snow, and albedo, different parts of the world heat up differently. This causes a big temperature difference between the poles and the equator, such that there is excessive heat in the tropics while a deficit in the polar regions [Hartmann, 2015]. However, there are two main mechanisms in the Earth's climate system that prevent the equator from becoming hotter and hotter, and poles becoming colder and colder. The first one are ocean currents transporting warm surface water to the poles and cold subsurface water to the tropics, which is largly driven by tempreture gradients and salinity. The second one is the large-scale atmospheric circulation which creates the global wind patterns. In the both Hemispheres there are three main atmospheric circulation cells namely, the Hadley (between about 0° and 30° latitude), Ferrell cells (between about 30° and 60° latitude) and Polar cells (between about 60° and 90° latitude). These circulation cells transport heat from the tropical to polar latitudes in order to reduce the meridional imbalance between the poles and equator [Bjerknes, 1964; Wyrtki, 1973]. While the oceanic mechanism mostly dominates in the tropics, meridional heat transport in the mid-to-high latitudes contains a considerable atmospheric component [Fedorov, 2008].

In general, the ocean and atmosphere interact via different types of energy fluxes such as long and short-wave radiation or latent and sensible heat and thereby exchange heat via conduction and convection [Woolnough et al., 2001]. For instance, a positive feedback loop between surface wind, evaporation and sea surface temperature (WES) is one example of the role of surface heat fluxes. The WES feedback is a result of an initial southward cross-equatorial SST gradient above and below the equator (cooler SST on the northern side and warmer SST on the southern side). This SST gradient initiates wind anomalies toward the south. However due to the Coriolis force, the southward winds, turn westward (eastward) on the Northern (Southern) Hemisphere. These winds will furthur interact with the existing northeasterly

(southeasterly) winds. Therefore, the total wind speed increases (decreases), which leads to increasing (decreasing) amounts of latent heat release from the oceans into the atmosphere. The higher amount of released latent heat flux causes the surface of the ocean to become cooler and further intensifies the inital SST gradient (positive feedback) [Xie and Philander, 1994]. The WES feedback can enhance the northward displacement of the Intertropical Convergence Zone (ITCZ) over the Atlantic and eastern Pacific [Xie and Philander, 1994]. The ITCZ is a belt of a low atmospheric surface pressure near the equator where northern and southern air masses converge.

The ocean–atmosphere coupling has been found essential for explaining various key climate phenomena, ranging from the seasonal cycle characteristics in the tropics over the inter-anual variability of the El Niño–Southern Oscillation (ENSO) to various patterns of decadal-scale climate variability such as Pacific Decadal Oscillation (PDO) or Atlantic Multidecadal Oscillation (AMO) [Alexander et al., 2002; Trenberth and Hurrell, 1994]. With the improvements of data collection methods such as satellite-based observations or space-borne microwave sensors, more reliable climate data for SST, surface wind, precipitation, etc. have been collected, which in turn lead to new insight into air-sea interaction [Xie, 2004]. Moreover, after the first implementation of coupled ocean-atmosphere general circulation models [Manabe and Bryan, 1969], they became an important tool not only to study air-sea interactions but also their changes over the time.

This chapter provides a short overview about the ocean-atmosphere interaction and its role in the Earth climate system. I will first explain the mechanisms of these interactions over the tropical oceans, namely tropical Pacific ocean, tropical Atlantic ocean and tropical Indian ocean, as well as over mid-latitude oceans. Next, I will provide a glimpse of the possible connections between different tropical oceans and also between tropical and mid latitude oceans.

4.1. Seasonal cycle of ocean-atmosphere interaction

The largest variation of ocean-atmosphere interaction happens at the seasonal scale and affects humankind socially and economically [Wells, 2011]. Solar radiation is the main driver for seasonal changes in ocean-atmosphere interaction. Although the solar irradiation does not change much within one year at the top of the atmosphere, on the Earth's surface, the winter or summer weather can be different from one year to the other. The reason is that due to the interactions between the ocean, land, and atmosphere, solar irradiation that reaches the Earth' surface varies at different times and regions which leads to anomalies in the seasonal cycle. For instance, the monsoon in Africa and Asia is a consequence of seasonal changes in solar irradiation [Wells, 2011]. The mid-latitudes have a more variable climate than the tropics, yet the seasonal cycle has an important role and leads to more intense storm systems in winter than in summer [Wells, 2011].

In the tropical ocean, even a small change in SST can induce an anomalous evaporation rate which leads to changes in water vapour pressure over the ocean

[Wells, 2011]. The ocean's mixed layer (the upper 50-200 meters) mainly interacts with the atmosphere and stores the heat available in different seasons [Wells, 2011]. Therefore any changes in the depth and temperature of this layer can lead to an anomalous behavior in the atmosphere. In addition, the heat transport in tropical and mid-latitude oceans has a seasonal variation. In the tropics, the seasonal cycle of oceanic heat transport is much stronger than in the mid-latitudes [Wells, 2011]. The main reason for stronger seasonal changes of heat transport in lower latitudes are the strong trade winds. Trade winds exert a strong wind shear on the mixed layer of the ocean, which leads to the enhancement of the Ekman transport [Wells, 2011]. The Ekman transport represents the movement of the surface layer of the ocean due to the surface wind (here trade winds). The Coriolis force makes the direction of the Ekman transport perpendicular to the direction of the surface wind. In the Northern Hemisphere the Ekman transport is directed towards the North Pole and in the Southern Hemisphere is towards the South Pole. The warm water movement towards the poles, brings cooler subsurface water to the surface to create a mass balance in the ocean at lower latitude.

There are several examples of regional effects of the seasonal cycle on air-sea interaction. In the northeastern Pacific, it has been found that the warmer SST during summer can persist toward the autumn and winter, which leads to more intense mid-latitude cyclones [Namias, 1969]. The warmer SST produces more latent and sensible heat. As a consequence, the energy of storms increases during autumn and winter [Wells, 2011]. However, these interactions are self-destructive in the end and the moment the anomalous source of heat in the ocean wipe out, the atmosphere reacts accordingly and its anomalous circulation will be seized. Nevertheless, the anomalous SST during summer can remain in the mixed layer of the ocean and trigger an atmospheric response in the subsequent autumn and winter [Wells, 2011]. The North Atlantic has been shown to behave similar to the North Pacific [Rodwell, 2002]. During winter the warmer SST in the North Atlantic can remain in the mixed layer of the ocean and decay in the following spring and summer. This can be used for a seasonal prediction of the weather over Europe with higher level of confidence [Rodwell, 2002; Wells, 2011].

4.2. Ocean-atmosphere interaction in the tropics

In the following I will focus mainly on climate variability over the tropical oceans and the corresponding mechanisms of regional air-sea interaction.

4.2.1. Tropical Pacific

The most important consequence of the air-sea interaction over the whole equatorial Pacific Ocean is ENSO [Wang et al., 2013]. It has been shown that the Bjerknes positive ocean–atmosphere feedback (which describes the interaction between thermocline adjustment, upwelling, SST, atmospheric convection and winds) plays the main role for the onset of positive (El Niño) or negative phases (La Niña) of ENSO

[C. Wang and Picaut, 2013]. Furthermore, mass exchange due to the wind shear in the tropics is also considered as another mechanism which determines the interannual variability of ENSO [Wang et al., 2013].

The positive phase of ENSO is called El Niño and corresponds to an anomalous warming of SST in tropical eastern Pacific during December or January. El Niños appear irregularly between two and seven years. The classical El Niño, which occurs near to the coast of Ecuador and Peru, leads to a weak upwelling in the eastern Pacific Ocean and therefore less productive coastal water [Wells, 2011]. Specifically, in a normal year, the coastal upwelling of the water in thermocline, which originate from the cool northward Peru Current, transports the cold sub-surface water to the surface. This cold current is the most productive of the eastern boundary currents globally [Penven et al., 2005]. It is very rich in nutrients and can absorb large amounts of solar radiation, which provides the perfect conditions for the growth of phytoplankton and in turn increase in fishery yields [Wells, 2011]. In El Niño years, due to a lack of upwelling, the nutrients in the coastal waters decrease. Hence the situation is not anymore favorable for fishery, which affects the economy of Peru and Ecuador [Wells, 2011]. The SST warming during El Niño years extends from the international dateline toward the South American coast up to 20°S [Wells, 2011]. This area covers almost 10 percent of the Earth's surface. Therefore during El Niño phases the global mean temperature can rise by a few tenths degrees in the following months [Wells, 2011]. The negative phase of ENSO is called La Niña. It represent periods of below-average sea surface temperatures across the east-central Equatorial Pacific and warmer then average sea surface temperatures in western Equatorial Pacific. Impact of La Niña on global scale tend to be opposite those of El Niño impacts. For instance, Indonesia and Australia can get much more rain than usual during La Niña phases. However, the cold water in the eastern Pacific causes less clouds to form there. Therefore, places like the southwestern United States can be much drier than usual. Associated with the oceanic compound of ENSO, the atmospheric counterpart called the Southern Oscillation is often described as the seasonal pressure difference between Indonesia and Tahiti in the south-east Pacific. Due to a steady pressure difference, a persistent south-east trade wind flows from Tahiti towards Indonesia [Wells, 2011]. However, during El Niño years the surface pressure in Indonesia increases while the pressure over the south-east Pacific Ocean decreases. Therefore, these trade winds become weaker. Usually, the Southern Oscillation Index is used to characterize the pressure difference fluctuations between these two areas [Wells, 2011]. A negative index value is associated with the weakening of south-east trade winds and the presence of El Niño. On the other hand, a positive index is attributed to higher pressure over the south-east Pacific Ocean and lower surface pressure over Indonesia (La Niña phase).

The strengths and position of pressure system between Indonesia and Tahiti can lead to variations in the position of the tropical convergence zones. These zones correspond to regions of heavy rainfall because of the uplifting of warm moist air masses. This air is transported by trade winds towards the tropics in the lower troposphere. There are two main tropical convergence zones in the normal ENSO

phase, one is the ITCZ [described in the begining of section 4] which over the Pacific extends from Indonesia in the west and reaches South America in the east between 5 to 10°N and further north over land masses of Africa and Asia (up to 30°N in eastern Asia) during July and August. In January, the ITCZ remains mainly south of the equator over the Atlantic and moves additionally southward over South America, Southern Africa and Australia. The second important convergence zone is called South Pacific Convergence Zone (SPCZ), which covers areas over northern Australia to the south-eastern part of the central South Pacific. As the trade winds bring moist air into the convergence zones, a parcel of air with low water vapor content flows in the upper troposphere toward the south-east Pacific to balance the total mass of air in the atmosphere. As the air in the upper troposphere reaches the south-east Pacific, it begins to descend and due to adiabatic warming, it gets warmer, which leads to the formation of an area with clear sky and low precipitation [Wells, 2011]. Usually, this region is called the 'dry zone' between the two convergence zones. The resulting circulation cell can be decomposed into two components, one in north-south direction which is called the 'Hadley Circulation' (Figure 4.1) and one in east-west direction which is known as the 'Walker Circulation' (Figure 4.2) [Wells, 2011].

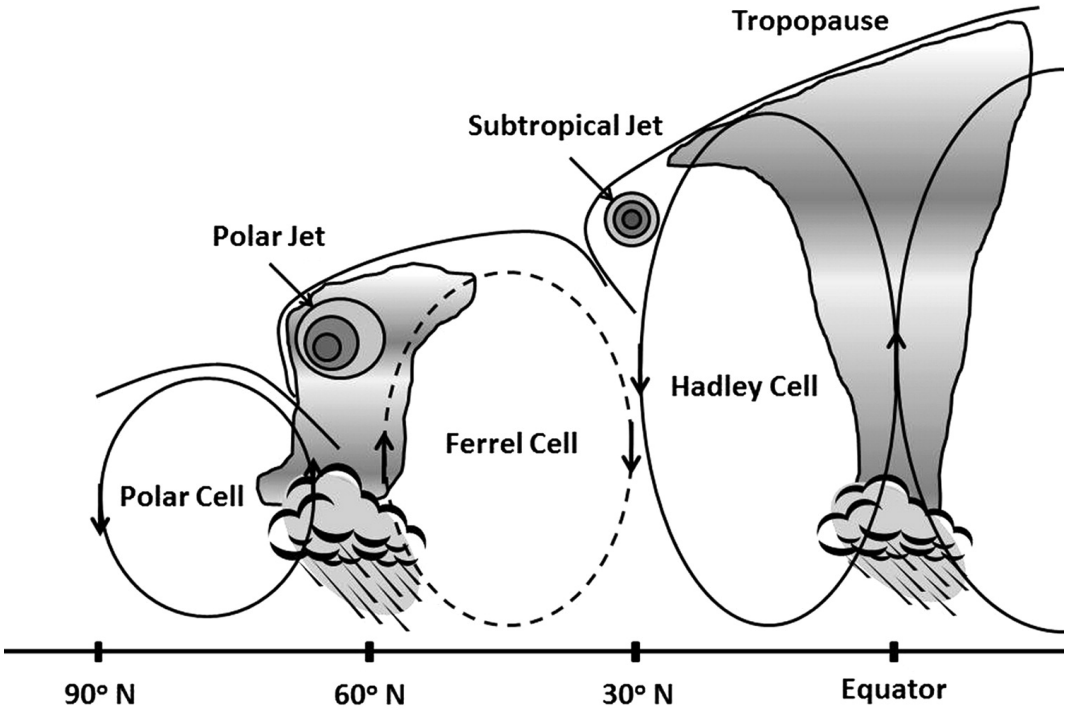

Figure 4.1.: Illustration of Hadley circulation cells adopted from Sun et al., 2014.

Trade winds are also responsible for upwelling along the coast of South America. These winds bring the cooler sub-surface water to the surface and create a large cold tongue of water in the eastern tropical Pacific Ocean [Wells, 2011]. The onset

of the negative phase of ENSO, La Niña, is associated with stronger trade winds. During El Niño, on the other hand, trade winds become weaker which leads to the replacement of the cold tongue by warmer water. In strong El Niño years, the cold tongue can even disappear completely. Furthermore, the weaker trade winds shift the tropical convergence zones, i.e., the ITCZ moves southward towards the equator and the SPCZ moves more to the east. This displacement causes less rain and more droughts over Indonesia and northern Australia on the one hand, and more heavy rain over the islands in the central and eastern equatorial Pacific ocean on the other hand.

Although ENSO is mainly a tropical phenomenon, it can have great impacts well beyond this region. For instance, the anomalous pressure system of the Southern Oscillation can affect the atmospheric circulation at mid-latitudes or the monsoon systems over Asia and Africa [Wells, 2011]. During El Niño years, western North America can experience a warmer than usual winter because the atmospheric circulation over the North Pacific is affected by the anomalous warming of the eastern tropical Pacific ocean. These long-range influences of ENSO, which go beyond the tropical Pacific ocean, are related to 'teleconnections'.

Although ENSO is the most prominent climate phenomenon in the tropical oceans, both the tropical Atlantic ocean and the tropical Indian ocean also possess their specific characteristics which are a direct result of the air-sea interaction.

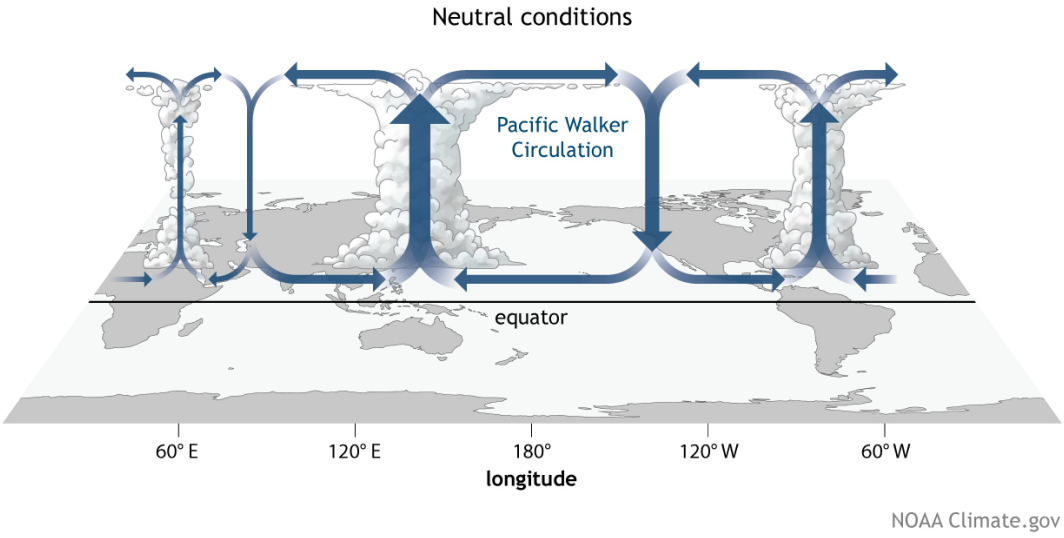

Figure 4.2.: Illustration of Walker circulation cells adopted from *The Walker Circulation: ENSO's atmospheric buddy | NOAA Climate.gov* 2018.

4.2.2. Tropical Atlantic ocean

The Tropical Atlantic ocean circulation has (in comparison with Pacific oceans) a stronger northward component at upper and intermediate depth to balance the

strong southward flow of deep level water (i.e., Meridional Overturning Circulation (MOC) in the North Atlantic Ocean). The climate variability in the tropical Atlantic ranges from seasonal up to decadal time scales and a significant part of the variability [Carton et al., 1996; Chang et al., 1997]. The tropical Atlantic also has a Bjerknes-type feedback mechanism similar to the Pacific Ocean which leads to the Atlantic Niño phenomenon. Although Atlantic Niños are much weaker than their Pacific counterparts, their occurrances are more frequent [Zebiak, 1993]. In Atlantic Niños, the cold tongue of water in the eastern tropical Atlantic disappears and is replaced by warmer water moving to the south along the southwestern coast of Africa. The anomalous warm SST at the eastern part of the ocean, causes a weakening of trade winds and a displacement of the convection zone towards the warmer region in the east [Wang et al., 2013].

However, Atlantic Niños are not the only source of variability in the tropical Atlantic. For instance, a displacement of the ITCZ over the western part of the tropical Atlantic ocean can affect the weather systems in north-eastern Brazil drastically [Wang et al., 2013]. A small displacement of the ITCZ's latitude towards the north (south) can cause floods (droughts) in this sensitive region [Wang et al., 2013]. It has been shown that the displacement of the ITCZ is a direct consequence of an anomalous cross-equatorial SST gradient in the Atlantic ocean which resembles a 'dipole' pattern [Wang et al., 2013]. The fluctuations in the latitudinal position of the ITCZ influence the amount of heat flux entering into the ocean, which in turn enhance the initial anomalous pattern of SST in the tropical Atlantic ocean. ENSO can also affect the SST and wind direction over the tropical Atlantic especially in the northern part [Curtis and Hastenrath, 1995; Enfield and Mayer, 1997]. The effects of ENSO can reach the Atlantic basin by changing the temperature of the troposphere or influencing the Walker circulation [Xie and Carton, 2013].

4.2.3. Tropical Indian ocean

In the past, the Indian ocean was generally considered to have a more passive role in coupled climate modeling. However, during the recent years, it has been recognized that the variability in thermocline depth and ocean currents in the Indian ocean can also influence the heat transport among ocean and atmosphere [Wang et al., 2013]. The Bjerknes feedback mechanism is also noted in the Indian ocean during boreal summer and fall with weaker easterlies. These weaker easterlies can lead to upwelling near the coast of Indonesia. However, the easterlies can become stronger during a strong Indian Niño (Indian Ocean dipole). Hence, during an Indian Niño, the eastward equatorial jet (Wyrtki jet) which is normally active during fall, disappears and results in more cooling at the eastern part of the Indian ocean [Saji et al., 1999].

In comparison to the other two tropical oceans, the thermocline in the equatorial Indian ocean is deep but it gets shallow in the so-called *dome* located south of the equator. This shallow thermocline is favors frequent upwelling and cooler SST. The dome is formed as a result of the ocean's response (Sverdrup response) to the wind

curl created by the equatorial westerlies and southeast trades in the southern Indian ocean [Wang et al., 2013].

The coupling between oceanic Rossby waves and the atmosphere is another rather strong process which occurs in the Indian Ocean. Oceanic Rossby waves are a direct result of the wind shear gradient and are excited by ENSO and Indian Niño. These Rossby waves create large SST anomalies in the southern Indian Ocean dome, which in turn cause variability in atmospheric convective processes [Xie et al., 2002].

Also, in the Indian ocean, there are two other main regions which induce atmospheric variability. One is the Bay of Bengal, in which SST anomalies are connected to the onset or retreat of the Indian summer monsoon [Sengupta et al., 2012]. The other is the western Arabian Sea with anomalous SSTs during summer time due to the instability of the Somali Current and the Great Whirl, which in turn cause variability in surface wind speed and wind curl [Vecchi et al., 2004].

4.3. Ocean-atmosphere interaction in the mid-latitudes

The ocean-atmosphere interaction in the mid-latitudes can be complex due to several reasons. For instance, the complex meteorology in the mid-latitudes makes it hard for wind and local SST anomalies to interact with each other. Also, SSTs are much cooler than in the tropics, the mixed layers are deeper, and the response of the ocean to atmospheric anomalies takes longer time. Furthermore, due to a larger Coriolis term, there are stronger momentum constraints.

Three mechanisms have been proposed to govern the ocean-atmosphere interactions in the mid-latitudes [Latif et al., 1998], each based on different theories. Here, I briefly explain these mechanisms to understand the ocean-atmosphere interaction in the mid-latitudes.

The first mechanism explains the ocean-atmosphere interaction through connecting mid-latitudes and tropics. In the conceptual model based on this theory, the SST anomaly, either negative or positive is transmitted into the mixed layer of the subtropical Pacific ocean [Gu and Philander, 1997]. Then, the water with anomalous temperature subducts into the thermocline and follows the Subtropical Cell (STC) and moves to the equator. The equatorward movement tilts to the west due to the effect of the Coriolis force [McCreary and Lu, 1994]. This water eventually gets into the equatorial thermocline and changes the stratification along the equator. This alternation influences the SST in the tropics, which in turn changes the wind reaching to the subtropics and intensifies the initial SST anomalies in the mid-latitudes. The anomalous stratification in the equatorial thermocline can also affect the onset of ENSO [Neelin et al., 1994].

The second mechanism focuses on changes in gyre circulation. Gyres are large systems of circulating ocean currents. The corresponding theory is based on the analysis of Latif and Barnett (1996) who noted a decadal ($\tilde{2}5$ year) mode of variability involving the Aleutian Low and the subtropical Pacific gyre. Based on this theory, as the subtropical gyre gets intensified, it can transport more warm water to the center

of the North Pacific. This water then interacts with the atmosphere and creates a positive feedback to elevate the initial SSTs through a reduction of meridional temperature gradients and amplification of net heat flux from the atmosphere.

In the third possible process, variations in the thermohaline circulation can affect the way ocean and atmosphere interact with each other. Such a mechanism has been well studied in the North Atlantic ocean [Delworth et al., 1993]. The North Atlantic is the only basin with a source of deep water in the north [Wang et al., 2013]. There is a direct relation between the formation rate of this deep water and the salinity of the North Atlantic and Arctic ocean basins [Mann and Park, 1996]. The mid-latitude gyre can influence this interaction by affecting the properties of the water that enters the Arctic basin. Due to atmospheric anomalies, the amount of freshwater entering the Arctic basin through the mid-latitude gyre can fluctuate, which eventually causes anomalies in the salinity of the water in the basin [Lazier, 1988].

In general, the internal fluctuations of the atmosphere increase as the air moves towards the poles but are well localized such as in the Pacific-North American (PNA) pattern or the North-Atlantic Oscillation (NAO) [Wang et al., 2013]. This level of variation can impose a challenge to studing the influence of SST patterns on the atmosphere. For instance, it was claimed that SST and wind speed are normally correlated negatively in the mid-latitudes especially in winter [Wang et al., 2013]. In turn, recent studies have shown that near surface ocean currents such as the Kuroshio, the Gulf Stream, and circumpolar currents (the main sources of SST anomalies), wind and SST can be correlated positively [Xie, 2004].

4.4. Interaction between tropical oceans

The SST anomalies associated with the three tropical oceans can be related to each other [Lanzante, 1996; Tourre and White, 1995]. The tropical forcing in the Pacific during ENSO has a major role in the interaction between the tropical oceans. The effect of ENSO can reach the other two oceans normally almost 1-2 season later via the atmopheric circulation [Alexander et al., 2002]. The main footprint of El Niño is a warming of the tropical North Atlantic and the entire tropical Indian Ocean.

The atmospheric circulation or 'atmospheric bridge' is the main source of bridging the anomalies from the tropical Pacific ocean to the tropical Atlantic and Indian oceans. For instance, both Walker and Hadley circulations interact with ENSO [Klein et al., 1999]. During El Niño, the warming in the eastern equatorial Pacific displaces the convective activities from the western equatorial Pacific eastward towards the center of equatorial Pacific. Due to this displacement, the Walker circulation ascends over the central and eastern of equatorial Pacific and descends over the equatorial Atlantic and the equatorial Indo–western Pacific region. At the same time, the Hadley circulation becomes stronger over the eastern Pacific but weaker over the Atlantic and Indo–western Pacific sectors. The alternations in Walker and Hadley

circulation cause anomalies in surface wind speed, humidity, cloud cover, surface heat fluxes and SST over the tropical Indian and Atlantic oceans [Su et al., 2013].

Although the tropical Pacific is the dominant player among the tropical oceans, the tropical Indian ocean can also affect tropical Pacific variability. At the interseasonal timescale, the atmospheric Madden–Julian Oscillation develops over the Indian ocean and moves eastward to the Pacific basin and therefore can increase the probability for the onset of the Pacific El Niño [Takayabu et al., 1999]. The Indian Niño is another source of anomalies in the tropical Pacific. For instance, in the positive phase of the Indian Niño (cooler SST in the eastern part of the Indian ocean), due to anomalous surface winds, the Pacific can be affected [Behera and Yamagata, 2003].

4.5. Interaction between tropical and mid-latitude oceans

Besides the interaction among the three tropical oceans, their anomalies can also reach further to the mid-latitudes with the help of atmospheric Rossby waves. For instance, the fluctuations in convection zones caused by ENSO can reach areas beyond the tropical oceans [Alexander et al., 2013]. The PNA pattern is one example of the 'atmospheric bridge' between tropics and mid-latitudes [Wallace and Gutzler, 1981]. The PNA pattern is known to exhibit positive and negative geopotential height anomalies, which are reminiscent of ENSO in the tropical Pacific. These fluctuations start in the tropical Pacific, move towards the north Pacific, then change the direction to the east and reach the northestern United States before moving again southwards to reach the southeastern United States and the Gulf of Mexico.

Another examples are sea level pressure (SLP) and wind variations over the tropical Atlantic that can reach the tropical North Atlantic and the Western Hemisphere warm pool [Enfield and Mayer, 1997].

The interaction between tropics and mid-latitudes can also work in the opposite direction, i.e., the mid-latitudes can influence the atmospheric anomalies in the tropics [Pierce et al., 2000]. Specifically, at decadal time scales, SST anomalies in the mid-latitudes are much larger than in the tropics [Giese and Carton, 1999]. Moreover, the Azores high in the North Atlantic is the main source of influencing north-easterly trades on the one hand and mid-latitude westerlies on the other hand. Both of these wind systems are important for the climate variability in the tropics as discussed earlier (4.2).

4.6. Summery

In this chapter, I have explained one of the main aspects of the Earth's climate system, ocean-atmosphere interactions. The mechanisms behind such interactions vary from the tropics over mid-latitudes to the high-latitudes. Both atmosphere and ocean are complex systems, and yet coupling them, can induce more complexity. So far, I have explained those interactions from oceanographical and meteorological

points of view. However, in the next two chapters, I will use the coupled climate network framework to explore this interaction in more detail.

Chapter 5.

Application

5.1. Co-variability patterns of sea-surface temperatures and precipitation in dependence on the ENSO state

As I mentined in the chapter 4, the heterogeneous latitudinal distribution of incoming solar radiation at the Earth's surface leads to a meridional imbalance with excess energy in the tropics and a corresponding deficit in the polar regions [Hartmann, 2015]. Meridional heat transport balancing this gradient is realized by two main mechanisms: via ocean currents transporting warm surface water towards the poles and cold subsurface water towards the tropics, and by large-scale atmospheric circulation patterns [Bjerknes, 1964; Wyrtki, 1973]. While the oceanic mechanism mostly dominates in the tropics, meridional heat transport in the mid-to-high latitudes contains a considerable atmospheric component [Fedorov, 2008].

In order to better understand ocean–atmosphere coupling mechanisms, there have been many studies investigating which climate variability mode can trigger which spatio-temporal response patterns in different variables, with a particular focus on precipitation. For instance, a body of papers investigated the influence of El Niño (i.e., the warm phase of ENSO) over Southeast Asia, Indonesia, Australia and the United States [Rasmusson and Carpenter, 1982; Rasmusson and Wallace, 1983; Ropelewski and Halpert, 1986]. For Europe, the corresponding effect of the North Atlantic Oscillation (NAO) has raised particular interest [Hurrell et al., 2003; Scaife et al., 2008], whereas for Australia, the precipitation responses to the changing states of the Interdecadal Pacific Oscillation (IPO) and Southern Oscillation Index (SOI) have been studied [Power et al., 1999]. In addition to these mostly regionally focused studies, the effects of the ENSO, North Pacific Oscillation (NPO) and NAO on global precipitation patterns have been explored, revealing distinct regional response patterns to all these modes of climate variability [Kenyon and Hegerl, 2010]. However, especially precipitation extremes are most substantially affected by ENSO [Wiedermann et al., 2017], which can be seen all over the world, including India, Africa, South America, the Pacific Rim, North America, and, more weakly, Europe [Kenyon and Hegerl, 2010].

The aforementioned studies have in common that certain index variables representing different large-scale spatio-temporal climate variability patterns have been taken as references for studying mostly linear responses in terms of correlation or regression maps. Notably, this viewpoint reduces the complexity of the problem

under study considerably, but leads to a systematic loss of information on which parts (i.e., regions) of the addressed climatological field actually correlate strongly with, e.g., rainfall at a specific point in space. This general conceptual limitation can be overcome by considering the recently developed methodological framework of functional climate network analysis [Tsonis and Swanson, 2012; R. V. Donner et al., 2017; H. A. Dijkstra et al., 2019] as I introduced in the chapter 3 This approach takes the established framework of complex network theory as a basis for developing and employing a suite of characteristics describing the placement of strong mutual statistical associations among climate time series which may represent one or more climatological fields.

However, Most of the climate network studies have exclusively focused on the dynamics within a single climatological field or atmospheric layer. Recently, some studies have extended this framework to the study of interdependences among different variables or layers [Donges et al., 2011a; Feng et al., 2012; Wiedermann et al., 2016a]. For this purpose, the idea of correlation-based single-variable networks has been thoroughly generalized in terms of so-called coupled climate networks. This chapter follows the same idea by for the first time focusing on the co-variability between SST and precipitation (PCP) during different seasons and ENSO phases, which is motivated by the known distinct teleconnection patterns triggered by El Niño and La Niña. Thereby, I attempt to systematically characterize the time-dependent ENSO teleconnection patterns with global precipitation variability from a complex network point of view.

This chapter is primarily based on the study that is presented in P3.

5.1.1. Data description

In this study I utilize monthly SST anomalies computed from the global Extended Reconstruction Sea Surface Temperature (ERSST v3) data set with a spatial resolution of $2° \times 2°$ [Smith et al., 2008] and associated precipitation data with a spatial resolution of $2.5° \times 2.5°$ provided by the Global Precipitation Climatology Project (GPCP) Version-2 [Adler et al., 2003]. By considering anomalies for each time series I remove the annual cycle that otherwise would dominate the co-variability patterns among the studied series.

I focus on the common time period of both data sets from 1979–2015. All grid points containing missing values have been removed from the data prior to the further analysis. As a result, the total number of considered SST and PCP grid cells is $N_s = 9,456$ and $N_p = 10,368$, respectively.

As already emphasized in the introduction, the aim of this study is to analyze the spatial placement of strong correlations between ocean (SST) and atmosphere (PCP) variability during different seasons, i.e., boreal winter (DJF), spring (MAM), summer (JJA) and autumn (SON). Therefore, I further differentiate the time series into El Niño, La Niña and neutral ENSO phases based on the Oceanic Niño Index (ONI). El Niño conditions is present when the Oceanic Niño Index is +0.5 or higher, indicating the east-central tropical Pacific is significantly warmer than usual. La

Niña conditions exist when the Oceanic Niño Index is -0.5 or lower, indicating the region is cooler than usual. By using the corresponding years from fall to summer for each ENSO phase, I associate 156 months with El Niño, 120 with La Niña, and 168 with the neutral ENSO phase. Dividing these numbers by the four seasons results in 39, 30 and 42 months for each of the three situations, respectively. In the following, I will consider the corresponding data subsets and, due to their relatively small sizes, focus on linear correlations as a statistical association measure, since more complex measures typically cannot be estimated reliably from the given relatively small sample sizes.

5.1.2. Coupled climate network analysis

I consider the two climatological fields under study (tailored to the specific situation of interest as described above) described by two sets of univariate time series $\{X_n^{(s)}(t)\}_{n=1}^{N^{(s)}}$ (for SST) and $\{X_m^{(p)}(t)\}_{m=1}^{N^{(p)}}$ (for PCP). In what follows, I will use the superscript index s (p) to refer to properties of the SST (PCP) field.

Network construction: In a climate network, each time series is represented by a node embedded at the spatial position of the respective grid or measurement point. In this case, the corresponding links indicate strong linear (Pearson) correlations between pairs of such series. Since I have to consider all time series from both fields, I first estimate the full $N \times N$ lag-zero correlation matrix between all $N = N^{(s)} + N^{(p)}$ time series. This correlation matrix contains all pairwise correlations between SST grid points, between PCP grid points, and between pairs of SST and PCP time series, which can be conveniently represented by a block structure

$$\mathbf{P} = \begin{pmatrix} \mathbf{P}^{(ss)} & \mathbf{P}^{(sp)} \\ \mathbf{P}^{(ps)} & \mathbf{P}^{(pp)} \end{pmatrix}. \tag{5.1}$$

Here, the two sub-matrices $\mathbf{P}^{(ss)}$ (of size $N^{(s)} \times N^{(s)}$) and $\mathbf{P}^{(pp)}$ ($N^{(p)} \times N^{(p)}$) represent the correlation matrices of the SST and PCP fields, respectively, which consist of elements

$$P_{nm}^{(ss)} = \frac{C_{nm}^{(ss)}}{\sigma_n^{(s)} \sigma_m^{(s)}}, \qquad n, m = 1, \ldots, N^{(s)}, \tag{5.2}$$

$$P_{nm}^{(pp)} = \frac{C_{nm}^{(pp)}}{\sigma_n^{(p)} \sigma_m^{(p)}}, \qquad n, m = 1, \ldots, N^{(p)}. \tag{5.3}$$

In the above equations, $\sigma^{(\bullet)}$ and $\mathbf{C}^{(\bullet\bullet)}$ denote the respective standard deviation vectors and covariance matrices of the two considered fields defined in the standard way. In full analogy, I identify the sub-matrices $\mathbf{P}^{(sp)}$ and $\mathbf{P}^{(ps)}$ as containing all correlation coefficients between time series in SST and PCP (respectively, PCP and

SST). Since I use only lag-zero correlations in this study, the two latter matrices can easily be transformed into each other by simple transposition.

In order to transform the correlation matrix $\mathbf{P}$ into the binary adjacency (connectivity) of the associated network representation (describing whether (1) or not (0) a link between two grid points exists), I employ a fixed yet individual threshold to each of the submatrices, retaining only those pairs of grid points for which the correlation exceeds the respective threshold. Here, for the submatrices describing only one field (SST or PCP, respectively), I select these thresholds $Tr^{(ss)}$ and $Tr^{(pp)}$ so that a fraction $\rho^{(s)} = \rho^{(p)} = 0.01$ of all pairs of grid points (the so-called (internal) link density) is represented by links in each of the two subnetworks. This threshold implies that I only consider correlations above the empirical 99th percentile of all correlations between all time series within each field. For the linkages between both fields (i.e., the so-called bipartite or cross-links between SST and PCP nodes in the coupled climate network representation), I proceed in a similar way by choosing a threshold $Tr^{(sp)} = Tr^{(ps)}$ so that a fraction $\rho^{(sp)} = \rho^{(ps)} = 0.005 < \rho^{(s)}, \rho^{(p)}$ (i.e., the corresponding cross-link density) is retained. Taken together, I obtain the coupled network's adjacency matrix as

$$\mathbf{A}^{+} = \begin{pmatrix} \Theta(|\mathbf{P}^{(ss)}| - Tr^{(ss)}) & \Theta(|\mathbf{P}^{(sp)}| - Tr^{(sp)}) \\ \Theta(|\mathbf{P}^{(ps)}| - Tr^{(ps)}) & \Theta(|\mathbf{P}^{(pp)}| - Tr^{(pp)}) \end{pmatrix}, \tag{5.4}$$

where $\Theta(\bullet)$ denotes the Heaviside function. Note that I use here the so-called extended adjacency matrix, which also contains self-loops since each SST (PCP) grid point is trivially correlated with itself at the maximal possible correlation coefficient of 1. This setting is motivated by the further use of area-weighted network measures as discussed below [Heitzig et al., 2012].

In order to justify the choices of internal and cross-link densities, I note that commonly, the correlations within one climatological field tend to be stronger than between two different fields. Therefore, taking just a global common threshold to all submatrices might effectively eliminate all cross-links, which are however the properties of interest in this work. In order to account for this, I enforce the presence of both, internal and cross-links, by imposing the aforesaid constraints via the different link densities, ensuring that the number of cross-links is still generally smaller than the number of internal links within each of the two considered fields. This setting is relevant in order to be able to properly interpret the resulting mathematical structure as the adjacency matrix of two coupled yet still identifiable subnetworks.

Area-weighted cross-degree: By computing certain statistics on the adjacency matrix, different network measures can be obtained that help understanding different aspects of the underlying network structure at either local or global scale [Newman, 2003; Albert and Barabási, 2002a]. In case of climate data, I however need to account for the spatially heterogeneous spacing between neighboring grid points, which commonly decreases towards the poles, in order to avoid overrepresentation of the high latitudes in the climate network characteristics. This can be done by

assigning a weight to each node corresponding to the spatial area it represents, i.e. [Tsonis et al., 2006]:

$$w_n = \cos \lambda_n, \tag{5.5}$$

with the latitudinal position λ_n of node n on the grid. In a more general context, this idea of area-weighting has been formalized in terms of node-weighted network characteristics (so-called node-splitting invariant or shortly n.s.i. measures) [Heitzig et al., 2012].

For this study, I solely focus on the simplest possible network measure, the n.s.i. version of the cross-degree [Donges et al., 2011a] as previously introduced in the chapter 3 [Feng et al., 2012; Wiedermann et al., 2016a], which characterizes the areal share of the entire globe that one node in a given field is connected to in the other field:

$$k_m^{j*} = \sum_{n \in V_j} w_n A_{mn}^{+}, \tag{5.6}$$

where V_i and V_j denote the respective sets of nodes describing the two subnetworks (i.e., SST and PCP field).

5.1.3. Community structure

Communities are groups of nodes within a network, which are relatively tightly connected with each other while only weakly connected to the rest of the network [Newman and Girvan, 2004]. Often, such communities can be considered as meaningful subsystems that are solely determined by the overall connectivity structure [Arenas et al., 2006]. Due to its resulting practical relevance, community detection has become an active area of research within complex network science [Fortunato, 2010; Fortunato and Hric, 2016]. Main challenges, however, concern the speed and efficiency of community detection, which attempts to solve some optimization problem that may have multiple solutions of similar quality.

In the context of climate network analysis, a recent paper [Tsonis et al., 2011] employed an algorithm [Newman and Girvan, 2004] based on the progressive removal of dominant links (in terms of information flow) for identifying the community structure of several climatological fields (500 hPa geopotential height, sea level pressure and surface temperature) derived from the NCEP/NCAR reanalysis [Kistler et al., 2001] and simulations of the Geophysical Fluid Dynamics Laboratory (GFDL) climate model CM2.1 [Delworth et al., 2006].

The quality of a given partitioning of a network into possible communities can be characterized by the associated modularity [Newman and Girvan, 2004]. If a network is divided into M communities, I can define an $M \times M$ symmetric matrix $\mathbf{e}$, such that each element e_{ij} is given by the fraction of links that connects nodes in community i to nodes in community j. Thus, $\sum_i e_{ii}$ gives the fraction of links that connect nodes within the same community, while $a_i = \sum_j e_{ij}$ represents the fraction

of all edges in the network that has at least one end in community i. In a random network, in which edges connect nodes independent of the communities they belong to, it is expected that $e_{ij} = a_i a_j$, so that $\sum_i a_i^2$ would correspond to the fraction of all edges that connect to nodes in the same community. In a modular network, it is requested that the e_{ij} should be high in comparison to the a_i^2. I make use of this requirement for defining the modularity M as [Newman and Girvan, 2004]

$$M = \sum_{i=1}^{n} (e_{ij} - a_i^2). \tag{5.7}$$

In the present work, I extend the concept of communities to the giant adjacency matrix $\mathbf{A}^+$ containing all links within the SST and PCP fields as well as all cross-links between both fields. Thereby, a network community can combine nodes representing different variables, which is different from most previous applications of the network community paradigm. I will refer to such multi-variable dense connectivity structures as cross-communities in the remainder of this work.

In order to obtain as robust communities as possible, I utilize the Infomap algorithm [Tantet and Dijkstra, 2014], which attempts to divide weakly modular regions into small communities. In the context of climate networks, these small communities are more likely to represent physically meaningful spatial co-variability patterns because they are more strongly connected internally.

5.1.4. Results

In the following, I will present the results of the coupled climate network analysis between SSTs and precipitation (PCP) during different seasons and ENSO phases.

5.1.4.1. Area-weighted cross-degrees

First, I investigate the n.s.i. cross-degree patterns of links from nodes in the SST field towards the PCP field (SST $\rightarrow$ PCP) and vice versa (PCP $\rightarrow$ SST). For example, a large n.s.i. cross-degree of SST $\rightarrow$ PCP indicates a grid point in the SST field that is strongly correlated with a large spatial area in the precipitation field.

Absolute correlations: I start by constructing coupled climate networks based on the largest absolute correlation values, indicating the generally strongest linear statistical associations between variables. Figure 5.1 shows the corresponding area-weighted cross-degree patterns for SST $\rightarrow$ PCP.

During boreal fall (SON), El Niño years are characterized by strong cross-connectivity (i.e., strong effects on global precipitation) arising from two regions in the eastern equatorial Pacific and between the western equatorial and southern subtropical Pacific (Fig. 5.1A). Similar yet weaker influence patterns are also observable during La Niña years (Fig. 5.1E), while neutral ENSO years are characterized by the absence

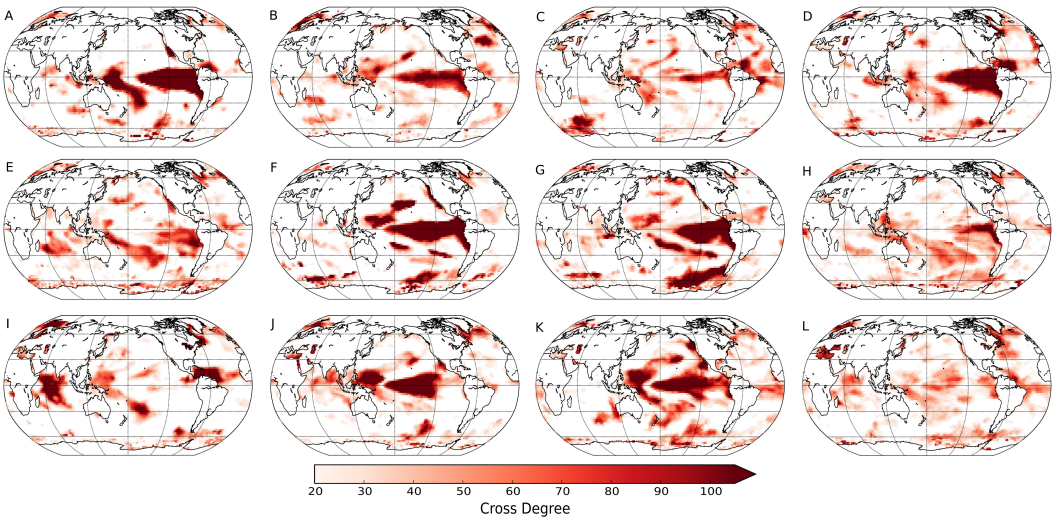

Figure 5.1.: $SST \rightarrow PCP$ cross-degree for EN (up), LN (middle) and the neutral ENSO (bottom). (A,E,I) is for SON, (B,F,J) for DJF, (C,J,K) for MAM and (D,H,L) is for JJA seasons.

of the western equatorial Pacific center of influence, which is replaced by two other patterns in the Indian ocean and equatorial Atlantic (Fig. 5.1I).

With the progressive evolution of El Niño or La Niña conditions, the boreal winter season (DJF) is characterized by particularly strong influence patterns. El Niño years mostly feature the main ENSO region in the central to eastern equatorial Pacific exhibiting particularly strong co-variability with the global precipitation field (Fig. 5.1B), while a second smaller pattern emerges over the westernmost Pacific. Interestingly, the corresponding area-weighted cross-degree patterns are even more strongly pronounced during La Niña conditions (Fig. 5.1F), highlighting in particular the eastern equatorial Pacific and the subtropical western to northern central Pacific. During normal ENSO conditions, mostly connectivity in the central and western equatorial Pacific is found (Fig. 5.1J).

Boreal spring (MAM) experiences the greatest influence of SST on precipitation during El Niño conditions in a small equatorial band spanning from the central Pacific to the eastern Atlantic ocean (Fig. 5.1C). A second region with high cross-connectivity emerges in the southernmost Indian ocean. In comparison with this, during La Niña conditions (Fig. 5.1G), much larger regions are characterized by high cross-connectivity with the precipitation field, including again the ENSO region in the eastern equatorial Pacific, but also the southeastern Pacific (resembling the typical spatial location of the Amundsen low atmospheric circulation pattern). The corresponding patterns become more dispersed during neutral ENSO conditions, resembling closely those already observed during DJF (Fig. 5.1K).

Finally, the boreal summer season (JJA) sees strong effects of eastern equatorial Pacific SSTs on precipitation after El Niño events (Fig. 5.1D), while only relatively

weak patches of elevated cross-degrees are visible during La Niña and neutral ENSO years (Fig. 5.1H,L).

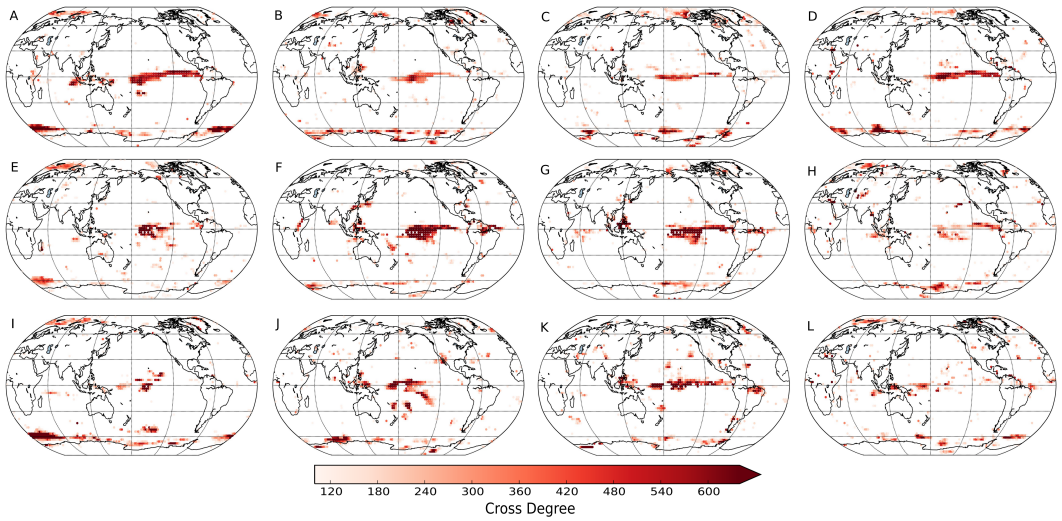

Figure 5.2.: Same as for Fig. 5.1, but for PCP → SST.

Figure 5.2 presents the corresponding area-weighted cross-link density between the precipitation variability at one grid point and all grid points in the global SST field. In comparison with Fig. 5.1, the strongly connected patterns comprise much less grid cells than for the opposite direction and are mostly confined to two small bands in the equatorial Pacific and close to the Antarctic coastline.

For the neutral ENSO phase, PCP patterns in the central equatorial Pacific and over the maritime continent are most strongly correlated with SST during the boreal winter season (Fig. 5.2J). During La Niña years, this season seas mostly a strong pattern over the central equatoral Pacific (Fig. 5.2F), but also another smaller patch over the northern part of Brazil. In turn, during El Niño years (Fig. 5.2B), only a single pattern over the central equatorial Pacific is observed, which is however considerably weaker than during La Niña conditions.

During the boreal fall of neutral ENSO years (Fig. 5.2K), the dominating cross-degree patterns spread over a larger region in the equatorial Pacific. During La Niña (Fig. 5.2G), the patterns are qualitatively the same as during DJF but a bit weaker. Similarly, during El Niño years (Fig. 5.2C), the observed core regions stay qualitatively the same as in winter.

Notably, during both, boreal fall and summer, the cross-degree patterns during neutral ENSO years are very weak and mostly cover some tropical regions (Fig. 5.2I,L). The same applies to La Niña phases, while there are still some stronger patterns over the eastern equatorial Pacific yet much weaker than during DJF and MAM (Fig. 5.2E,H). In turn, during El Niño conditions, the main cross-degree patterns stay confined to the central-to-eastern equatorial Pacific (Fig. 5.2A,D). Due to the imposed equal link densities, the largely visible absence of marked ”cross-hubs” (i.e.,

high cross-degree nodes) in the PCP field suggests a relatively homogeneous effect globally (except for the few discussed patterns), as opposed to the far larger spatially confined patterns in the SST field.

Positive correlations: While having previously considered strong absolute correlations, I have mixed up information on regions where, e.g., strong positive SST anomalies trigger wet and dry conditions. Since both have distinctively different implications for the affected ecosystems and population, I now turn to a separate analysis for positive and negative correlations, respectively. For the positive correlations, Figs. 5.3 and 5.4 reveal strong similarities with the networks constructed based on absolute correlations. This appears understandable, since vast affected areas located are in the tropics and subtropics, where I may expect positive SST anomalies to result in excess evaporation, leading to enhanced convective activity, cloud formation and, subsequently, precipitation.

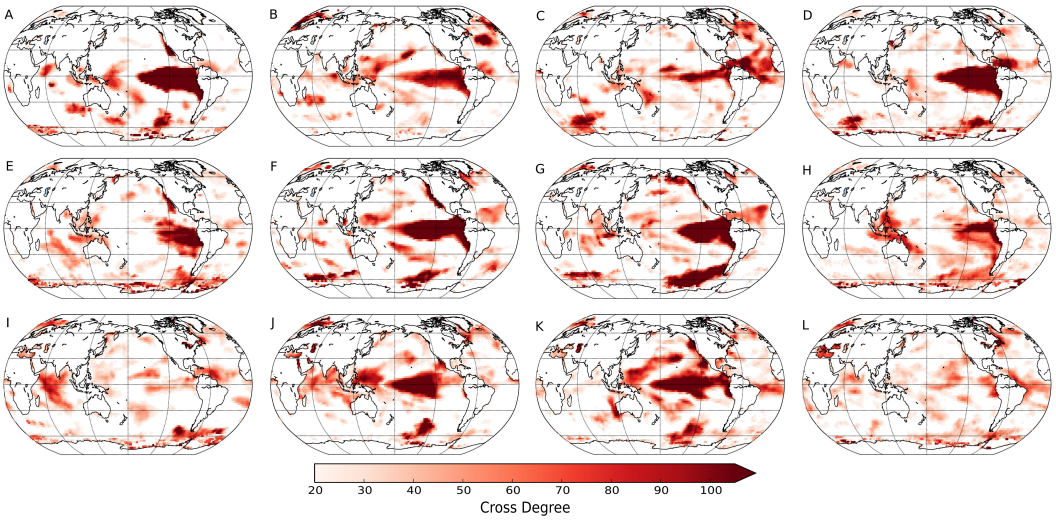

Figure 5.3.: As in Fig. 5.1, but considering only strong positive correlations

Negative correlations: Finally, I study the coupled climate networks obtained using the strongest negative correlations only.

During boreal fall, the neutral ENSO phase is characterized by elevated cross-degree patterns in the tropical North Atlantic, western equatorial towards southwestern Pacific and central Indian ocean (Fig. 5.5I). The associated cross-degree patterns in PCP are mainly weak and concentrated over the central equatorial Pacific (Fig. 5.6I). During La Niña (Fig. 5.5E), high n.s.i. cross-degrees for SST $\rightarrow$ PCP are found in the western equatorial to southwestern Pacific and weakly over the Indian Ocean, while the corresponding largest cross-degrees for PCP $\rightarrow$ SST are still concentrated over the central equatorial Pacific (Fig. 5.6E). El Niño events (Fig. 5.5A) are

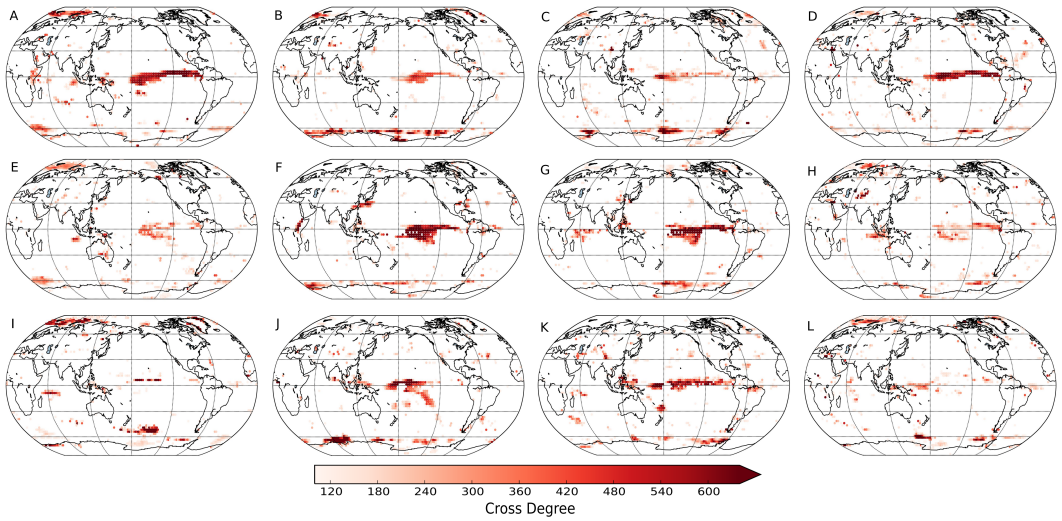

Figure 5.4.: As in Fig. 5.2, but considering only strong positive correlations

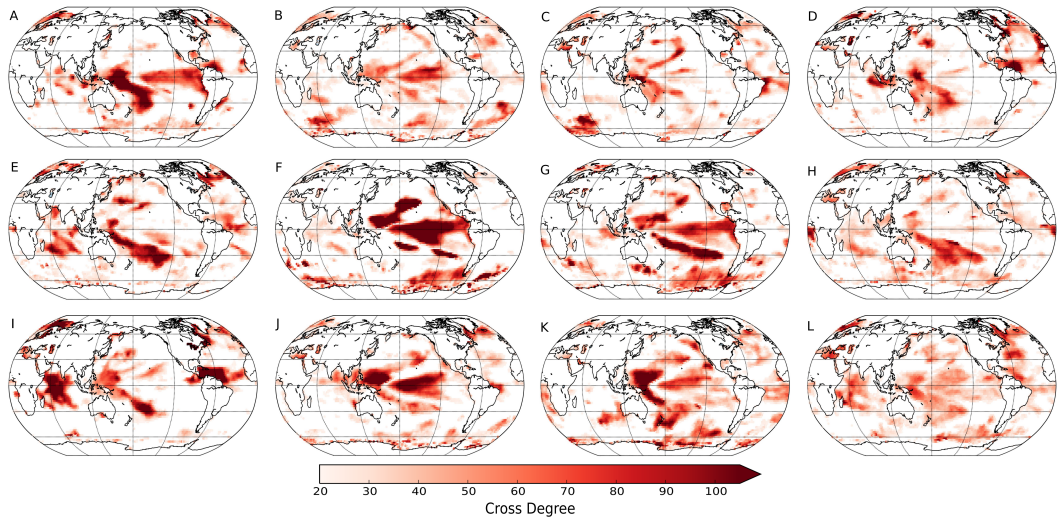

Figure 5.5.: As in Fig. 5.1, but considering only strong negative correlations

characterized by a weak pattern of elevated cross-degrees over the eastern equatorial Pacific, but stronger ones between the estern equatorial and southwestern Pacific. The corresponding PCP patterns (Fig. 5.6A) are mostly concentrated over the western equatorial Pacific and the maritime continent. Interestingly, the previously observed circumpolar Antarctica precipitation pattern is markedly correlated with SST regardless of the ENSO state.

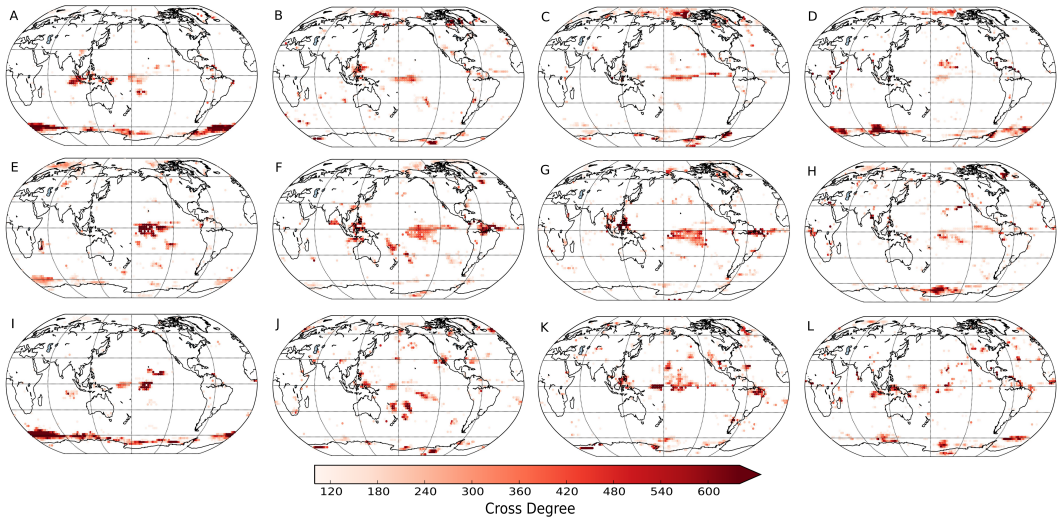

Figure 5.6.: As in Fig. 5.2, but considering only strong negative correlations

5.1.4.2. Communities

As a final step of this analysis, I take a look at the two-variable community structure of the coupled SST/PCP network. Since I expect the most interesting differences between the three types of ENSO phases to arise during boreal winter (where El Niño and La Niña peak), I present here exclusively the results for this season. Moreover, in order to allow for some interpretable visualization, I disregard such communities that include less than 1% of the nodes of the coupled network.

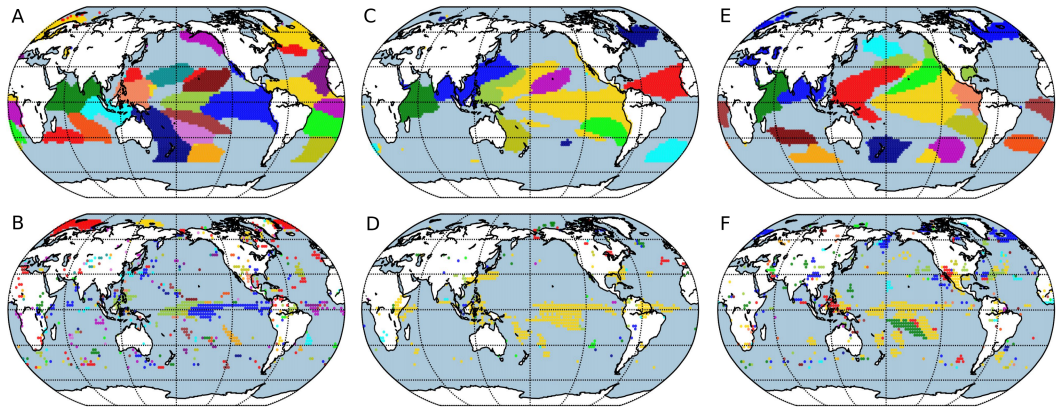

Figure 5.7.: Cross-variable communities for El Niño (left), La Niña (middle) and the neutral ENSO phase (right). (A,C,E) denote community members in the SST field, while (B,D,F) indicate those in PCP.

Figure 5.7 shows the cross-communities for the different ENSO phases as identified with the Infomap algorithm (see Methods section). I first recognize that these

communities in most cases correspond to spatially contiguous regions in the SST field (with a few exceptions where individual communities contain more than one substantially large region), whereas they appear fragmented in the PCP field. In general, in the SST field, many of the larger cross-communities involve those nodes that have been previously identified as appearing as high cross-degree patterns, suggesting that the associated communities indeed also include regions in the PCP field (cf. the different colors in Fig. 5.7).

When comparing especially the respective contributions of the SST field to the individual communities, I observe that El Niño phases appear to exhibit a larger number of relevant communities than during La Niña or neutral ENSO phases. This observation could have two possible yet incompatible reasons: First, the linkage structure within the SST field (representing connections that either directly link different SST grid points or are indirectly mediated via PCP grid points) is more fragmented during El Niño phases. This might however be a contradiction to the established fact that El Niño leads to large-scale synchronization of climate variability due to common trends [Radebach et al., 2013]. More in line with the latter fact, the higher number of communities could also be interpreted as reflecting a generally more homogeneous network structure, for which already very minor differences in the link placement may cause the Isomap algorithm to split larger groups of nodes into different communities.

5.1.5. Discussion

In order to study ocean-atmosphere coupling from a complex network perspective, I have generated coupled network representations of SST and precipitation fields and evaluated the associated n.s.i. cross-degree and cross-community patterns.

In boreal fall, precipitation is linked with SSTs in the Indian Ocean, the Caribbean Sea, the Barents Sea and an area of cyclogenesis near Newfoundland. In the subsequent winter and spring, the n.s.i. cross-degree for absolute correlations (Figs. 5.1 and 5.2) shows that even during the neutral phase of ENSO (which is often considered less relevant in terms of teleconnectivity), SSTs in the central equatorial Pacific are strongly linked to precipitation. Interestingly, the corresponding SST variability is accompanied by both, positive and negative correlations with precipitation patterns, whereby positive correlations are more focused in the eastern central Pacific and negative ones in the western central Pacific. In boreal summer, these pattern are less pronounced and more homogeneously distributed, which could point to a stronger relevance of local-scale (convective) processes. All aforementioned regions are moreover also associated with negative correlations. Positive SST correlations with precipitation can be found in the central Pacific, while negative ones arise particularly over the maritime continent and Central America. Moreover, SST also strongly affects precipitation close to the Antarctic coastline.

During La Niña, the patterns observed for neutral ENSO phases are further enhanced. This particularly applies to the cross-degree values in the equatorial Pacific and especially in boreal winter and spring. A few main patterns can be

identified, including an elongated pattern in the central and eastern tropical Pacific, an arc-shaped pattern in the western Pacific and some pattern close to the Californian coast and in the Amundsen Sea in the South Pacific. Like during the neutral phase, the western Pacific SST anomalies are linked with precipitation with negative correlations and their eastern Pacific counterparts with positive correlations. Strongly affected precipitation can be localized in a large area in the central Pacific (with positive correlations) and over the maritime continent and the Caribbean Sea (negative correlations). Precipitation is mainly associated with one large community involving the SSTs in the central-to-eastern equatorial Pacific.

During El Niño, the Walker circulation is markedly weakened, which causes warmer SSTs in the eastern equatorial Pacific and a cooling in the western equatorial Pacific. These changes in the Walker circulation cause more rain in the central-to-eastern tropical Pacific and less rain over the maritime continent. However, mostly the SST anomalies in the eastern equatorial Pacific are strongly linked to precipitation. The precipitation anomalies are correlated with SST anomalies mostly in the central eastern Pacific, the eastern equatorial Pacific and over the maritime continent. Like during La Niña and the neutral ENSO phase, the western Pacific anomalies are related to negative correlations with precipitation, while the eastern Pacific anomalies exhibit positive correlations. Communities in the SST field are spatially reorganized and focused on the western Pacific, while associated precipitation components commonly link to more than one SST pattern.

By studying the n.s.i. cross-degree not only for absolute correlations, but also separately for strong positive and negative correlations, I have demonstrated that it is possible to distinguish different patterns of variability from each other. Moreover, cross-community analysis can be employed to classify the nodes of the coupled SST-PCP network representation into distinct groups of strongly co-varying grid point time series. Accordingly, the proposed cross-community analysis provides additional information as compared with using only the n.s.i. cross-degree, which can be utilized in order to further characterize the main regions in both climate fields that mutually influence and interact with each other.

Interestingly, SST $\rightarrow$ PCP patterns that are pronouncedly visible in the neutral ENSO phase are weakened during La Niña and even suppressed during El Niño. This particularly applies to the Indian ocean (with variability largely characterized by the Madden-Julian Oscillation and Indian Ocean Dipole, the Mediterranean Sea to Caspian Sea, some region near Newfoundland, and the Caribbean Sea (reduced during El Niño, suppressed during La Niña). In turn, during El Niño phases the natural links between SST and precipitation are interrupted and dominated by the SST variability of the tropical Pacific (and southern Pacific for La Niña).

This analysis has also recovered known teleconnections between SST and PCP triggered by El Niño, which however mostly correspond to wet anomalies over the Philippines, Uganda and near the US-Mexican border. Known dry areas (including Indonesia, northern Australia and the Amazonas region) do not match the obtained patterns, which could be partially resulting from the strong links to the circumpolar Antarctic area. During La Niña, nearly all regions that are known to be markedly

influenced by ENSO teleconnections exhibit a high cross-degree, including wet regions in northeastern South America and over the maritime continent as opposed to dry areas over Taiwan and Uganda.

From the methodological perspective, this study was restricted to a specific setting involving linear correlations and a particular choice of thresholds. According to my experiences from other studies, I expect that the main patterns discussed above should not be altered qualitatively when employing different thresholds, while a detailed investigation of the associated impacts would be beyond the scope of the present study. Moreover, I emphasize that I have chosen to employ monthly data and focus on lag-zero (i.e., quasi-instantaneous) interrelationships between SST and PCP. While a corresponding extension to lagged dependencies would be straightforward, it would add a considerable level of complexity to this study, so that I have refrained from addressing this aspect explicitly here.

5.1.6. Conclusions

I have used the coupled climate network approach to systematically study ocean-atmosphere interactions along with mutual effects between SST and precipitation. I have particularly investigated how the co-variability patterns between ocean and atmosphere change at monthly time-scales during different seasons and ENSO phases. I specifically focused on the n.s.i. cross-degree and cross-community structure between SST and precipitation for absolute, as well as for positive and negative Pearson correlations. By studying the n.s.i. cross-degree, I have demonstrated that mainly the tropical oceans affect global precipitation in a speatially coherent way, yet differently during different phases of ENSO. By comparing positive and negative values of correlations, I found out that, during the neutral phase of ENSO, the western (west of 180°E) Pacific, Indian ocean and Atlantic SSTs (in boreal fall) have negative effects on precipitation and vice versa, whereas the eastern regions like the central-to-eastern equatorial Pacific rather experience a positive SST effect on precipitation. Similar observations can be made during La Niña phases. As expected, the cross-degree patterns during El Niño phases reveal positive correlations between SST and precipitation especially in the eastern equatorial Pacific. Only during boreal fall, western equatorial Pacific SSTs can exhibit negative correlations with precipitation.

Complementary to the cross-degree fields, cross-communities depict interacting regions between SST and precipitation, ignoring how each individual node interacts with the whole climate system. Communities highlight the main areas in which SST and precipitation are strongly connected among each other. Accordingly, during neutral ENSO phases the main interaction zone between SST and precipitation is located in the central equatorial Pacific. In turn, during La Niñas, the main community in the SST fields covers much of the central-to-eastern equatorial Pacific, while the corresponding precipitation region mostly coincides with the central equatorial Pacific. These patterns are thus in general agreement with the findings for the n.s.i.

cross-degree. During El Niño phases, two separate patches in the eastern and central equatorial Pacific denote the most relevant regions.

Finally, This analysis has shown how the interaction between two different climatological fields can be studied with network tools during different ENSO types and seasons. One possible subject of future work could be extending this approach to more than two variables, or considering two variables but focusing on two or more distinct regions in order to capture their interactions. On the other hand, for studying climate dynamics one should also consider the effect of different time scales, i.e., how the interactions among different climate variables evolve across time and scale and how this is related with the network topology, including the community structure. For the latter purpose, one could use different methods (e.g., wavelet analysis) to decompose the time series into different time scales and study the interaction between two or more climate variables at separate time scales or between different scales to capture cross-scale variability.

Beyond its specific climatological focus, this study provides another example for the potential usefulness for diagnosing and attributing spatio-temporal patterns of climate variability across variables and regions. Future studies shall further take up these potentials of the employed methodology and investigate to which extent the thus gained knowledge can be further utilized for improving climate model diagnostics and statistical climate forecasts.

5.2. Disentangling the multi-scale effects of sea-surface temperatures on global precipitation

As it is been mentioned in the section 5.1 The study of the climate system using complex networks provides new insights into spatiotemporal climate dynamics. However accounting for the multivariate and multi-scale nature of climate variability introduces a new challenging perspective that could help to improve the understanding of the underlying physical mechanisms. In this study, I focus on the aforementioned two aspects of multiple variables and time-scales contributing to the variability of the climate system and show that cross-variable statistical relations evolve differently at different time-scales. In the previous study I already applied the climate networks for studying the multi-variable climate dynamics. In this study, I follow up on the previous study by combining time series decomposition for SST and PCP into contributions at different time scales.

Specifically, in order to disentangle the multi-scale interdependence between SST and PCP globally, I first employ the discrete wavelet transform, which provides a method to process data at different time-scales [Bradshaw and McIntosh, 1994; Lau and Weng, 1995; Jajcay et al., 2016; Paluš, 2018; Paluš, 2014]. This technique allows decomposing the local variability of SST and PCP individually into contributions with different characteristic time-scales.

This chapter is primarily based on the study that is presented in P2.

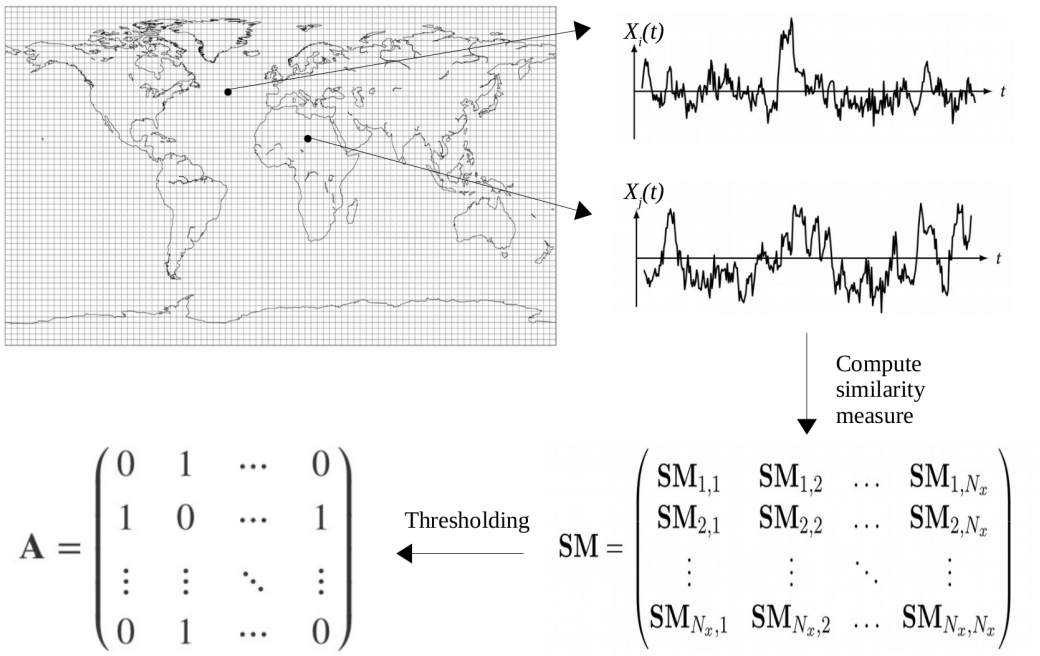

Figure 5.8.: Schematic illustration of the construction of a functional network from global gridded climate data sets (see text for details).

5.2.1. Data and method

5.2.1.1. Description of the data

I use global monthly SST and precipitation data for the period of 1979–2015 provided by the US National Oceanic and Atmospheric Administration – Earth System Research Laboratory's Physical Sciences Division (NOAA/OAR/ESRL PSD), which are freely available at `https://www.esrl.noaa.gov/psd/`. Specifically, I employ the ERSST v3b gridded SST dataset with a spatial resolution of $\Delta\lambda = \Delta\phi = 2°$, and the GPCP version 2.3 global precipitation dataset with a resolution of $\Delta\lambda = \Delta\phi = 2.5°$.

Since the goal is to capture long-term climate variability, monthly averages are generally preferred, because the high-frequency variability of daily data products might blur relevant variability at longer time-scales. As a preprocessing step, I first remove all grid points of SST and PCP with missing values or gaps, resulting in $9,456$ (SST) and $10,368$ (PCP) grid points, respectively. In a second step, I calculate the resulting anomaly series for each grid point by subtracting the climatological mean for each month of the year from the respective time series. Note that while the SST data set by definition only covers the oceans (without those parts that have been captured by sea-ice during at least one month of the study period), the PCP data have global coverage including both, the oceans and continents.

5.2.1.2. Analysis strategy

The following two subsections briefly explain the details of the two main ingredients of this analysis framework, wavelet decomposition and functional climate network analysis. Figure 5.8 presents a schematic view of this approach. Initially, I decompose the monthly SST and PCP data into their respective contributions at different time-scales (up to decadal scales) using the maximum overlap discrete wavelet transform (see below). Then, I compute the pairwise lag-zero correlation coefficients between the resulting scale-specific variations of each SST grid cell and all considered PCP grid cells. I repeat this procedure at each time-scale of interest. It is important to highlight that I am mainly interested in the effects of SST on precipitation, i.e., how the SST variability at different scales influences PCP at different time-scales around the globe. Thus, I do not study here possible effects of PCP on SST, which I have found to be generally less spatially coherent. Finally, by defining a global threshold to all cross-correlations between the SST and PCP fields at each time-scale, I obtain binary adjacency matrices that represent the connectivity structure of a coupled climate network based on which the corresponding network topology can be conveniently studied in terms of selected characteristics.

Maximum Overlap Discrete Wavelet Transform: I use the Maximal Overlapping Discrete Wavelet Transform (MODWT) which is a modification of the Discrete Wavelet Transform (DWT) [Maheswaran et al., 2014; Percival, 2008]. MODWT decomposes the time series into different time scales or frequency components. The wavelet decomposition is realized using the two basis functions known as father wavelet and mother wavelet. Any function $x(t)$ can be expressed through these basis functions and their scaled and translated versions are:

$$x(t) = \sum_k \tilde{V}_{J,k}\phi_{J,k}(t) + \sum_k \tilde{W}_{J,k}\Psi_{J,k}(t) + \sum_k \tilde{W}_{J-1,k}\Psi_{J-1,k}(t) + \ldots + \sum_k \tilde{W}_{1,k}\Psi_{1,k}(t) \quad (5.8)$$

where J is the total number of scales to be analyzed and k is in the range of 1 to T (the length of the time series). The coefficients $\tilde{V}_{J,k}$ are called approximation coefficients and $\tilde{W}_{J,k}$,...,$\tilde{W}_{1,k}$ wavelet transform coefficients at scales from J to 1, while the functions $\phi_{J,k}(t)$ and $\{\Phi_{j,k}|j = 1,\ldots,J-1,J\}$ are the approximating wavelet function and detail wavelet functions, respectively. These basis functions are defined in terms of father and mother wavelets as follows:

$$\phi_{j,k}(t) = 2^{\frac{-j}{2}}\phi(2^{-j}t - k) \quad (5.9)$$

$$\Psi_{j,k}(t) = 2^{\frac{-j}{2}}\Psi(2^{-j}t - k) \quad (5.10)$$

Further, the values of the wavelet transform coefficients at each of the scale and the approximation coefficients at scale J are estimated by:

$$\tilde{W}_{j,k} \approx \int \Psi_{j,k}(t) f(t) dt, \quad j = 1, \ldots, J-1, J \tag{5.11}$$

and

$$\tilde{V}_{j,k} \approx \int \phi_{J,k}(t) f(t) dt \tag{5.12}$$

respectively, where the scaling coefficients $\tilde{V}_{J,k}$ capture the smooth trend of the time series at the coarse scale 2^J, which are also called smooth coefficients; and the wavelet coefficients $\tilde{W}_{j,k}$, also known as detail coefficients can detect deviations from the coarsest scale to the finest scale. The original series $x(t)$ can be reconstructed by summing up the detailed components and the smooth components.

$$x(t) = \tilde{V}^k_{J,k} + \tilde{W}^k_{J,k} + \tilde{W}^k_{J-1,k} + \ldots + \tilde{W}^k_{1,k} \tag{5.13}$$

where

$$\tilde{V}^k_{j,k} = \sum_k \tilde{V}_{J,k} \phi_{J,k}(t),$$
$$\tilde{W}^k_{J,k} = \sum_k \tilde{W}_{J,k} \Psi_{J,k}(t), \ldots, \tilde{W}^k_{1,k} = \sum_k \tilde{W}_{1,k} \Psi_{1,k}(t). \tag{5.14}$$

Coupled climate networks: Let us denote the SST and PCP anomaly fields as $\{X_i(t)\}_{i=1}^{N_i}$ and $\{X_j(t)\}_{j=1}^{N_j}$, respectively, with $t = 1, \ldots, T$ indicating time steps with monthly mean values and i and j the specific grid points on the Earth from which the respective series have been taken. By applying the MODWT, I first decompose each SST and PCP time series at each grid point into seven distinct time series, each representing a specific time-scale (i.e., 1–2, 2–4, 4–8, 8–16, 16–32, 32–64, and 64–128 months).

For any of these scales, each time series is considered as a node in a climate network, which is identified with the spatial position of the corresponding grid point. Links between node i in the SST field and node j in the PCP field exist if some similarity measure SM_{ij} between the corresponding time series exceeds some given threshold Tr. Thus, the resulting climate network representation is given by the adjacency matrix

$$A_{ij} = \Theta(|SM_{ij}| - Tr) - \delta_{ij}, \tag{5.15}$$

where $\Theta(\cdot)$ denotes the Heaviside step function and δ is the Kronecker delta. As a similarity measure, I employ the classical Pearson correlation coefficient (pc) at lag zero as one of the simplest possible statistical association measures. The restriction to this linear characteristic does not contradict that fact that the climate system exhibits

a great variety of nonlinear relationships among its components. However, previous works have often shown that the most characteristic network patterns are already well visible in case of the linear pc and, thus, do not require the more computationally demanding estimation of nonlinear counter-parts like mutual information [Radebach et al., 2013].

To keep only the strongest statistical relationships, I consider Tr as the empirical 99% quantile value of all pairwise correlation values at a given MODWT scale. This choice is motivated by recent studies, where it was found that the 99% quantile is adequate for representing atmospheric teleconnections [Arizmendi et al., 2014]. In turn, I do not explicitly account for the increasing persistence of the individual records at coarser time-scales, since the latter affects all grid points in a similar way. In what follows, I will exclusively study the statistical linkages between the SST and PCP fields, while ignoring those between different grid points of the same field (as also considered in previous works [Donges et al., 2011a; Wiedermann et al., 2016a]), making the resulting network representations bipartite graphs where links exist exclusively between nodes (grid points) of different types (variables).

One important point in studying climate networks based on data given on a regular latitude–longitude grid (also called angularly regular grids, as used in this study) is that by moving towards the poles the spatial density of nodes systematically increases as it has been mentined in the secition 5. This problem can be accounted for by using specific node-weighted versions of the network measures of interest, so-called *node splitting invariant (n.s.i.)* measures [Heitzig et al., 2012]. Here, each node is weighted by the area on the Earth's surface it represents, so that nodes closer to the poles get gradually lower weights. It can be shown that a proper node weight for angularly regular grids is given by [Tsonis et al., 2006]

$$w_n = \cos \lambda_n, \tag{5.16}$$

where λ_n is the latitude associated with grid point/node n.

Having thus obtained the network's adjacency matrix and introduced proper node weights, I can now estimate different network measures. In this study, I restrict my attention to two characteristics that will be further described in the following. For quantifying local cross-variable interactions, I use the n.s.i. cross-degree [Donges et al., 2011a; Feng et al., 2012], which will be complemented by the n.s.i. cross-average link distance which measures the mean spatial distance between any pair of mutually connected (i.e., strongly correlated) SST and PCP grid points.

N.s.i. cross-degree: The n.s.i. cross-degree is defined as

$$k_m^{j*} = \sum_{n \in V_j} w_n A_{mn}, \tag{5.17}$$

where V_i and V_j denote the sets of nodes of two sub-networks (here, SST and PCP) and w_n is the weight of node n as defined in Eq. (7.12). k_m^{j*} gives the spatial area

represented by those nodes $n \in V_j$ that are connected with $m \in V_i$. By studying the n.s.i. cross-degree, I identify which areas of the SST field are strongly correlated with PCP variations. Those regions in the SST field that exhibit high values of the n.s.i. cross-degree can be interpreted as having particularly strong influence on PCP anomalies around the globe.

N.s.i. cross-average link distance: The second measure of interest in this study is the n.s.i. cross-average link distance

$$ALD_i^* = \frac{\sum_{n \in V_j} D_{mn} A_{mn}}{k_m^{j*}}, \tag{5.18}$$

where D_{mn} is the geodesic distance at the Earth's surface between two nodes $m \in V_i$ and $n \in V_j$ that are connected within the two climatological fields. This measure quantifies whether a specific SST node interacts more locally with the nodes of the PCP field, or whether there are long-distance interactions between them.

5.2.2. Results and discussion

Cross-degree at integrated time-scales: Figure 5.9 shows the spatial pattern of cross-degrees in the SST field with respect to global gridded precipitation data as the link targets. At the original monthly resolution of the data (Fig. 5.9a), it is evident that there are three main SST regions that are characterized by very strong effects on the precipitation field. Two of these regions are located in the equatorial Pacific (eastern-to-central and western tropical Pacific, respectively), while a third one is found in the southern Pacific ocean.

Regarding the pattern formed by the two tropical regions, it is noticeable that these closely resemble the known anomaly patterns of SST and sea-level pressure associated with ENSO. In this context, it should be highlighted that ENSO controls the time-dependent magnitude and spatial extent of the atmospheric Walker circulation over the Pacific, which is responsible for the zonal wind fields transporting moist air from areas with large evaporation (i.e., warm SSTs) to others that are characterized by condensation of water vapor followed by cloud formation and, finally, precipitation. The two areas with high cross-degree coincide with the main region that is directly affected by ENSO, but (especially on longer time scales) also partially the PDO as a strong mode of Pacific ocean-atmosphere coupled variability at decadal time-scales.

Notably, the spatial centers of action of ENSO and PDO are known to partially overlap. Specifically, while the PDO has its prime center in the Northern Pacific region, it also exhibits considerable co-variability patterns in the equatorial Pacific. This is distinctively different from ENSO, which primarily affects climate in the low latitudes, but has less clear linear co-variability patterns in the North Pacific [Mantua and Hare, 2002], although the existence of corresponding teleconnections has been studied in various papers, e.g., ref. [Yeh et al., 2018]. Taken together, due to their spatial overlap it is reasonable to consider ENSO and PDO as two mutually

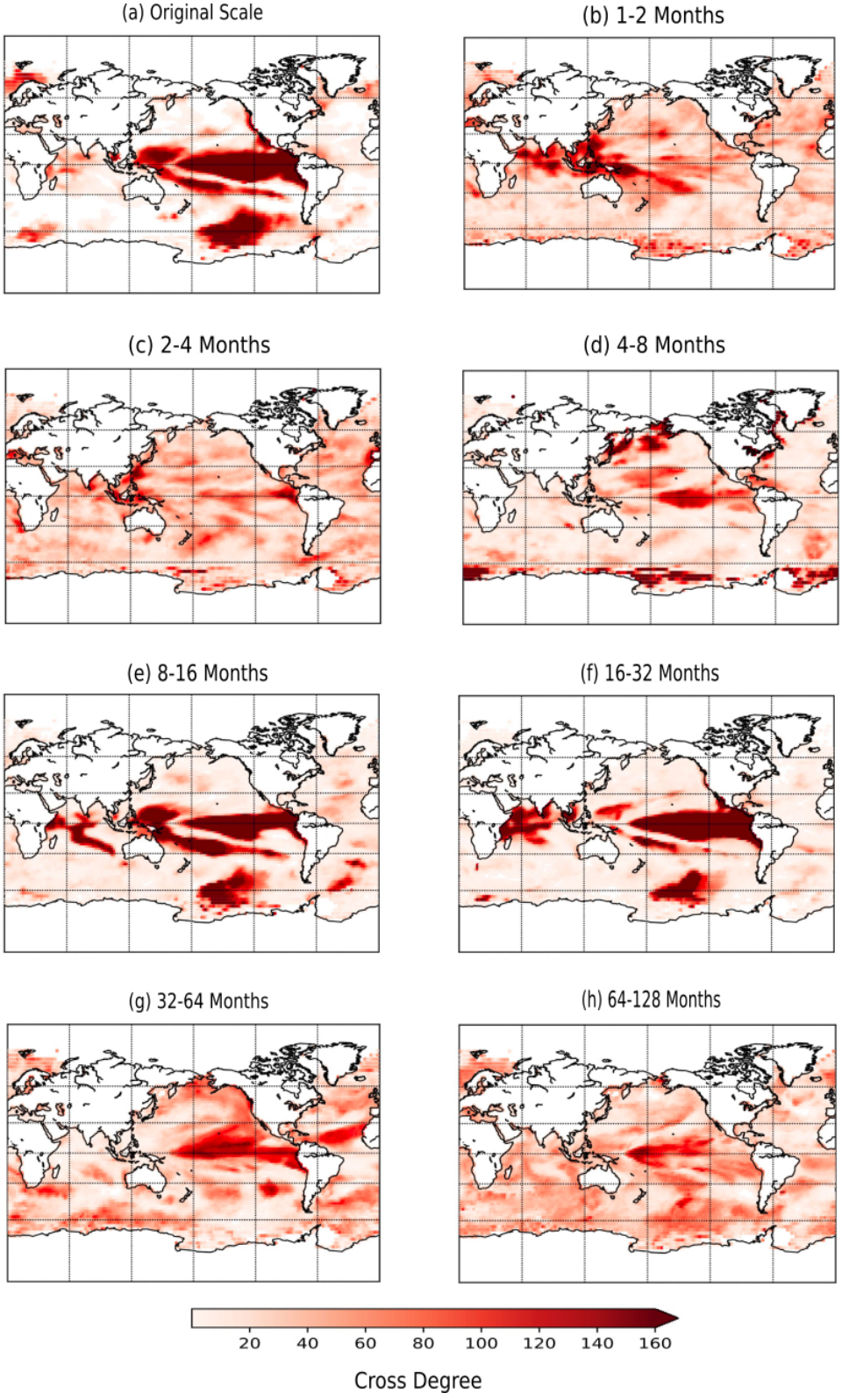

Figure 5.9.: N.s.i. cross-degree of $SST \rightarrow P$ for (a) the original anomaly time series and (b-h) the seven scales obtained by MODWT (1–2, 2–4, 4–8, 8–16, 16–32, 32–64 and 64–128 months), respectively.

interdependent phenomena, which are, however, relatively well separated in terms of their characteristic time scales (with ENSO varying considerably faster than the PDO). The corresponding interactions across space and time are likely mediated via different processes including the so-called Pacific Meridional Mode (PMM) [Chiang and Vimont, 2004; Lorenzo et al., 2015]. In turn, disentangling spatio-temporal SST patterns solely attributable to any of these modes has been proven a challenging task that is a subject of ongoing work [Wills et al., 2018]. Regarding the results presented in Fig. 5.9a, I tentatively conclude that when investigating climate variability at the original (monthly) resolution without separating the effects of different time-scales, the spatial signatures associated with the impacts of ENSO and PDO on global precipitation overlap spatially in the tropical and subtropical Pacific and can thus hardly be distinguished from each other based on the cross-degree pattern alone.

The third SST region with high n.s.i. cross-degree is located in the southern Pacific and appears closely related with the so-called Southern Annular Mode (SAM). Specifically, the spatial position of the identified region coincides well with the Amundsen Sea Low (ASL), a quasi-stationary atmospheric low pressure system over the Amundsen-Bellingshausen-Ross Sea. Previous works have already demonstrated that the ASL is often intensified or weakened in the presence of different ENSO phaes [Yiu, 2018]. However, the signatures of different time-scales in the ENSO-ASL teleconnection have hardly been studied explicitly in previous works, which is why I shall proceed next with considering the cross-degree fields from SST to PCP at the different frequency bands provided by the MODWT-based time series decomposition.

Scale-specific cross-degree patterns: At time-scales of 1 to 2 months (Fig. 5.9b), the most prominent cross-degree patterns are found in a region comprising the northern Indian ocean, maritime continent and westernmost tropical Pacific, implying that SST anomalies in that region have the strongest impacts on global precipitation variability. Both time-scale and spatial signature suggest that these patterns are associated with the MJO, which results in large-scale tropical deep convection patterns propagating eastward and influencing rainfall especially between the western Indian ocean and the western-to-central tropical Pacific. The corresponding traveling atmospheric pattern often fades in the eastern tropical Pacific, while eventually reappearing with lower strength over the tropical Atlantic and then reaching again its full strength over the Indian ocean to complete one of its cycles.

When moving towards slightly larger time-scales (2 to 4 months, Fig. 5.9c), the aforementioned high cross-degree pattern in the northern Indian and western Pacific oceans is gradually diminished in spatial extent and magnitude. I attribute this to the fact that MJO has no stationary period and, hence, may affect also time-scales beyond 2 months, yet only at its region of strongest effect, which would be compatible with the observations regarding the cross-degree field.

At scales between 4 and 8 months (Fig. 5.9d), I find different high cross-degree regions in the central Pacific ocean, near the Antarctic coastlines and in the north-western Pacific, as well as some smaller patches along the North American east

coast and over the Caribbean. The band around Antarctica is possibly related with the Antarctic Oscillation (AAO) or Southern Annular Mode (SAM) [Rogers and Loon, 1982], which describes a belt of westerlies related with the oceanic Antarctic Circumpolar Current (ACC) and can have large-scale effects on rainfall over the southern part of Australia [Risbey et al., 2009], South Africa [Gillett et al., 2006] and even China [Wu et al., 2009]. The pattern over the northern Pacific ocean appears reminiscent to the North Pacific Oscillation (NPO) which primarily acts on sub-seasonal time-scales [Linkin and Nigam, 2008]. The NPO is characterized by sea-level pressure anomalies that can trigger variations of subtropical SST patterns [Shin and An, 2018]. The resulting variations in the subtropical SST due to the NPO can in turn affect rainfall over the southern central United States and Mexico [Linkin and Nigam, 2008] and China [Wang and Chen, 2014]. It has been conjectured that NPO can play a vital role in triggering the onset of ENSO phases [Shin and An, 2018]. This result appears compatible with the observation of an elevated cross-degree pattern in the central Pacific Ocean (Fig. 5.9d), which could be related with such an effect of NPO on ENSO. Note, however, that the analysis presented here is purely correlative and does not aim at providing statements on causal effects among different large-scale patterns, which should be the subject of more detailed follow-up studies.

At scales from 8 to 16 months, I observe high cross-degrees in the eastern-to-central Pacific ocean and a bow-shaped region from the western tropical to central subtropical Pacific. These two patterns closely match the previously discussed regions that are most strongly influenced by the ENSO phenomenon. In addition, I also recover the pattern over the southern Pacific ocean that can be related to the ASL and its influence on rainfall anomalies over Antarctica [Raphael et al., 2016]. Yet another high cross-degree region emerges over the Indian ocean, which can be related with the Indian Ocean Dipole (IOD) pattern, an irregular SST oscillation in the western Indian Ocean [Saji et al., 1999; Webster et al., 1999] that is known to have marked teleconnections with rainfall patterns around the globe. Specifically, the IOD variability shows negative correlations with the precipitation in southern Western Australia and South Australia [Risbey et al., 2009], the southern parts of Brazil [Chan et al., 2008] and southeast Asia [Singhrattna et al., 2005], while positive correlations exist with precipitation over China [Qiu et al., 2014] and south-eastern Africa [Reason, 2001].

At the scale of 16 to 32 months (Fig. 5.9f), the cross-degree patterns show strong similarity with those at scales between 8 and 16 months. The most remarkable differences are that the bow-shaped pattern in the Pacific gets much weaker while the western Indian ocean becomes more prominent. In turn, the patterns in the eastern-to-central equatorial Pacific and the southern Pacific ocean remain almost the same. It should be noticed that the patterns at both, 8 to 16 and 16 to 32 months time-scales, exhibit the closest similarities with those obtained for the original unfiltered data. This provides evidence that ocean-atmosphere interactions within these two scales (i.e., around the annual cycle period and around two years) are most dominant. The lower frequency contributions most likely result from ENSO, which is known to be the tropical climate variability mode with the highest amplitude of

anomalies and most wide-spread effects globally. In addition, I may speculate about a possible additional effect of the atmospheric quasi-biennial oscillation, which has its core frequency right in the identified range of time-scales.

At time-scales of 32 to 64 months (Fig. 5.9g), the main ENSO-related high cross-degree region in the eastern-to-central tropical Pacific starts to get blurred, while new regions with high cross-degree emerge especially in the northern tropical to subtropical Atlantic. This pattern could be related to the Atlantic Equatorial Mode (AEM), which describes a quasi-periodic inter-annual warming and cooling of the equatorial Atlantic SST [Lübbecke et al., 2018; Mohino and Losada, 2015]. It has been shown that AEM can affect rainfall over both, adjacent and remote regions, including West Africa [Losada et al., 2010], Brazil [Giannini et al., 2004] and even central Europe [García-Serrano et al., 2011].

Finally, at 64 to 128 month time-scales (Fig. 5.9h), I still find elevated cross-degrees over the equatorial and southern Pacific Ocean. Interestingly, the Northern Pacific PDO signature that could have been expected to be observable at this time-scale is widely absent in the corresponding results. It may be hypothesized that corresponding patterns could show up only when turning to even lower frequencies. However, given the restricted time coverage of the studied data sets and increasing numerical artifacts of wavelet analyses at the beginning and end of the records, I hesitate to extend the present analysis towards even longer time-scales.

Cross-average link distances: Figure 5.10 shows the results for the cross-average link distance. This measure provides a complementary picture on the strength of the SST–PCP relationship by unfolding the spatial information contained in the associated coupled network's cross-linkage structure between both fields.

For the unfiltered time series (Fig. 5.10a), especially those regions that were already dominant in the n.s.i. cross-degree (Fig. 5.9a) exhibit short cross-link distances (red areas). This indicates that in these regions, SST strongly affects PCP, but mostly at smaller spatial scales, which dominate over possible remote teleconnections.

At time-scales of 1 to 2 months, most of the tropical oceans show mostly short cross-link distances. This could again be explained by a strong spatially localized modulation of SST and rainfall patterns due to the action of the MJO.

At the scale of 2 to 4 months, I recall the largely absent high n.s.i. cross-degree patterns that are present at other scales (Fig. 5.9c). Here, regions with small cross-average link distances only partly coincide with high cross-degrees, while particularly short average cross-link distances are found, e.g., in the eastern Pacific, over Indonesia and in the western part of Indian Ocean (Fig. 5.10c).

For 4 to 8 month time-scales up to 32 to 64 months (Figs. 5.10d,e,f,g), most of the tropical Pacific previously identified as the most densely connected region in the coupled SST-P network is characterized by short mean cross-link distances, which again points to a dominance of local SST effects on precipitation. In general, this indicates that at smaller spatial scales, SST and precipitation at monthly-to-interannual resolution are most intimately connected in the tropics, where particularly

high SSTs imply strong evaporation and, hence, convection feeding predominantly local rainfall. However, I note again that the finding that the tropical oceans are densely connected at short spatial scales does not imply an absence of long-distance connections, but simply a very large amount of short-distance connections.

Beyond these general observations, there are some other regions over which the mean cross-link distances decrease and increase when gradually moving from shorter to longer time-scales. For example, for 4 to 8 months (Fig. 5.10d), there is a region in the tropical Atlantic with short cross-link distances, which indicate strongly localized cross-correlations betwen SST and PCP. Over the western-to-central north Pacific, I find similar short cross-link distances, which could again be related to the effect of the NPO. By moving towards time-scales of 8 to 16 months (Fig. 5.10e), the cross-link distances in the tropical Atlantic increase, while those in the eastern Indian ocean decrease as a sign of strongly localized correlations between SST and PCP in this region. Interestingly, at 16 to 32 month time-scales (Fig. 5.10f), the cross-link distances over both, tropical Atlantic and Indian ocean increase, while only the equatorial Pacific is still characterized by short cross-link distances. This observation could be related to the strong spatial auto-correlation of both SST and precipitation in the ENSO region along with the aforementioned expected SST-precipitation coupling associated with ENSO variability. When proceeding to even longer time-scales of 32 to 64 months (Fig. 5.10g), the pattern of short cross-link distances in the tropical Pacific shifts towards the eastern part of the equatorial Pacific. Finally, at the time-scale of 64 to 128 months (Fig. 5.10h), there is only a small region with short cross-link distances remaining in the central tropical Pacific, which – along with the associated cross-degree patterns – indicates a much stronger variety of spatial link placements in the corresponding coupled climate network.

As an important general remark regarding the spatial structure of cross-links as captured by the cross-average link distance, I recall that the precipitation data set has global coverage including both oceans and continents, while the SST data are necessarily spatially limited. Due to the strong interdependence between SST and surface air temperature, a change in SST will strongly affect the atmosphere above the oceans and the resulting amount of water vapor. In turn, the present analysis does not account for the corresponding effect over the continents, which likely has certain implications for the inferred link structures. Future work should therefore extend the present analysis by considering the effect of both, sea and land surface temperatures (or surface air temperatures) on precipitation using an equivalent analysis strategy.

Zonal and meridional mean coupled network properties: In order to summarize the main spatial correlation patterns between ocean and atmosphere at different time-scales as revealed by the coupled networks properties, I finally compute zonal and meridional averages of n.s.i. cross-degree and n.s.i. cross-average link distance over all grid points with available time series. This perspective highlights again the previously found high cross-degrees in the tropics at time-scales between 8–16 and

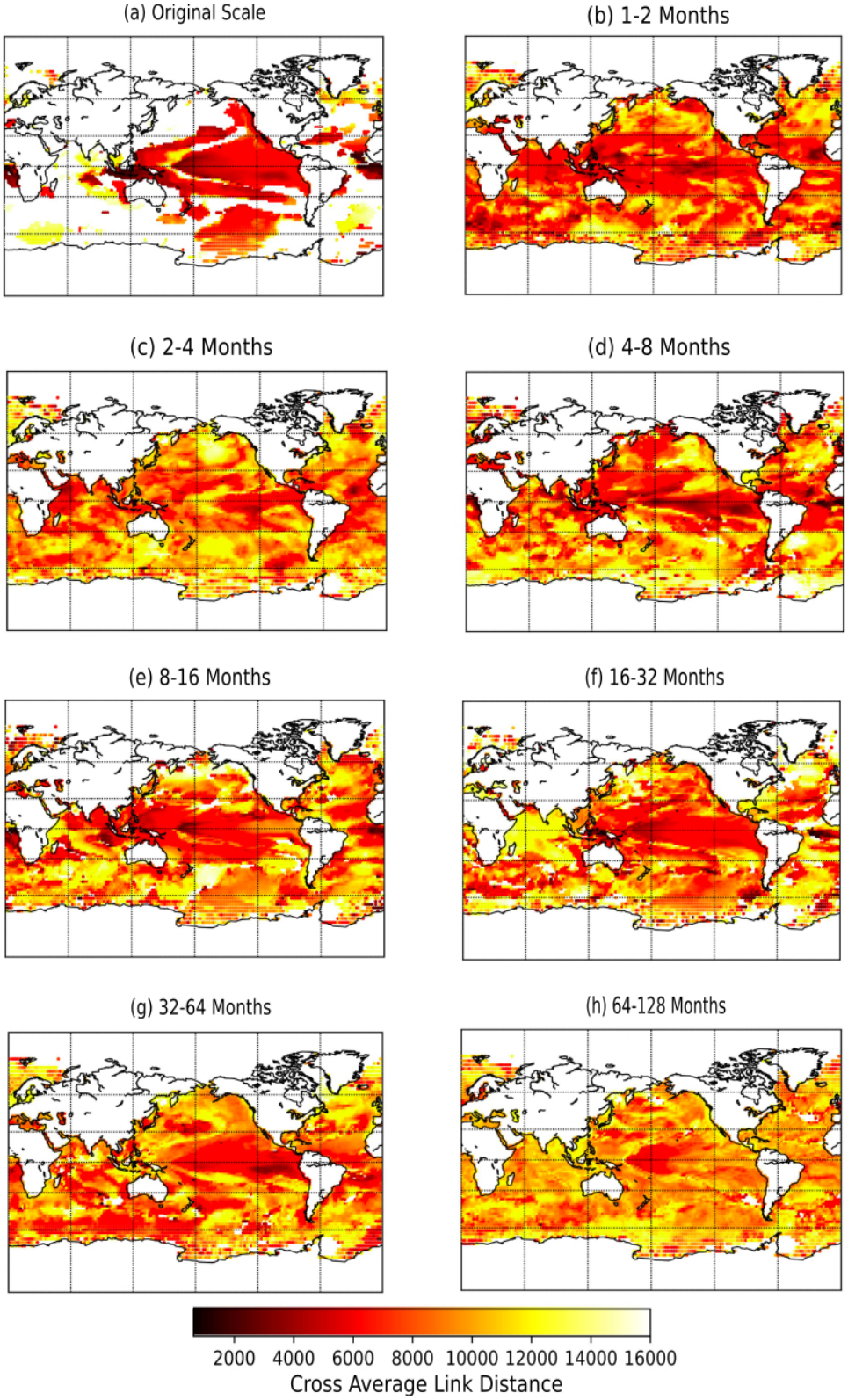

Figure 5.10.: Same as in Fig. 5.9, but for the n.s.i. cross-average link distances.

16–32 months (Fig. 5.11a), primarily in the eastern equatorial Pacific (Fig. 5.11b). The corresponding results thus demonstrate that the effect of SST variations in the eastern equatorial Pacific (i.e., the ENSO region) on global precipitation is generally stronger than in any other ocean basin at annual to shorter inter-annual time-scales.

Considering the zonal and meridional averages of the n.s.i. cross-average link distance, the tropics are generally characterized by the on average shortest cross-links among all time-scales, while the extratropics generally exhibit longer mean links (Fig. 5.11c). Taking this information together with the associated cross-degree patterns, it is likely that I observe here mostly regional effects that may originate from temporary SST and precipitation trends reflecting ENSO variability. In turn, some extratropical ocean regions (like the ASL region) also affect global precipitation patterns markedly, yet primarily at larger distances. This could be related to the fact that tropical precipitation reacts more quickly to SST via a fast evaporation–cloud formation–precipitation cycle (e.g., via local convective activity at daily to multi-day time-scales), while extratropical influences are transported via the atmospheric circulation (specifically, planetary wave patterns) to remote regions while not having an equally strong local effect on precipitation as tropical SSTs. Taking the longitudinal perspective into account (Fig. 5.11d), I find that localization of interdependence patterns primarily arises on seasonal to inter-annual time-scales in all three ocean basins, with a focus on the Indian and Pacific oceans.

In general, this results indicate that the spatial localization properties of ocean-atmosphere interactions as revealed by this analysis are mostly characteristic for the tropics at seasonal to inter-annual time-scales, while (sub-) seasonal and decadal scales exhibit only few highly and/or short-range connected patterns that are hardly visible in the zonal and meridional averages.

5.2.3. Conclusion

I have employed a complex network based framework to investigate the effect of oceanic conditions (expressed via sea-surface temperature (SST) patterns) on global precipitation at time-scales ranging from monthly to decadal scales. For this purpose, I have combined time series decomposition by the maximum-overlap discrete wavelet transform with functional network analysis in a coupled network setting.

The observed scale-specific statistical interdependence patterns between the two variables of interest have been characterized by the two coupled network measures n.s.i. cross-degree and n.s.i. cross-average link length. This analysis reveals main regions of SST that significantly influence precipitation around the globe at different time-scales. Notably, these regions differ among temporal scales, i.e., they show scale-specific behavior. By looking at the raw time series that include variability at all scales, main interdependence patterns between SST and precipitation are found, but information on the associated time-scales cannot be taken into account. This approach unfolds this otherwise hidden information and allows separating the effects of processes and large-scale climate patterns acting at different characteristic time-scales.

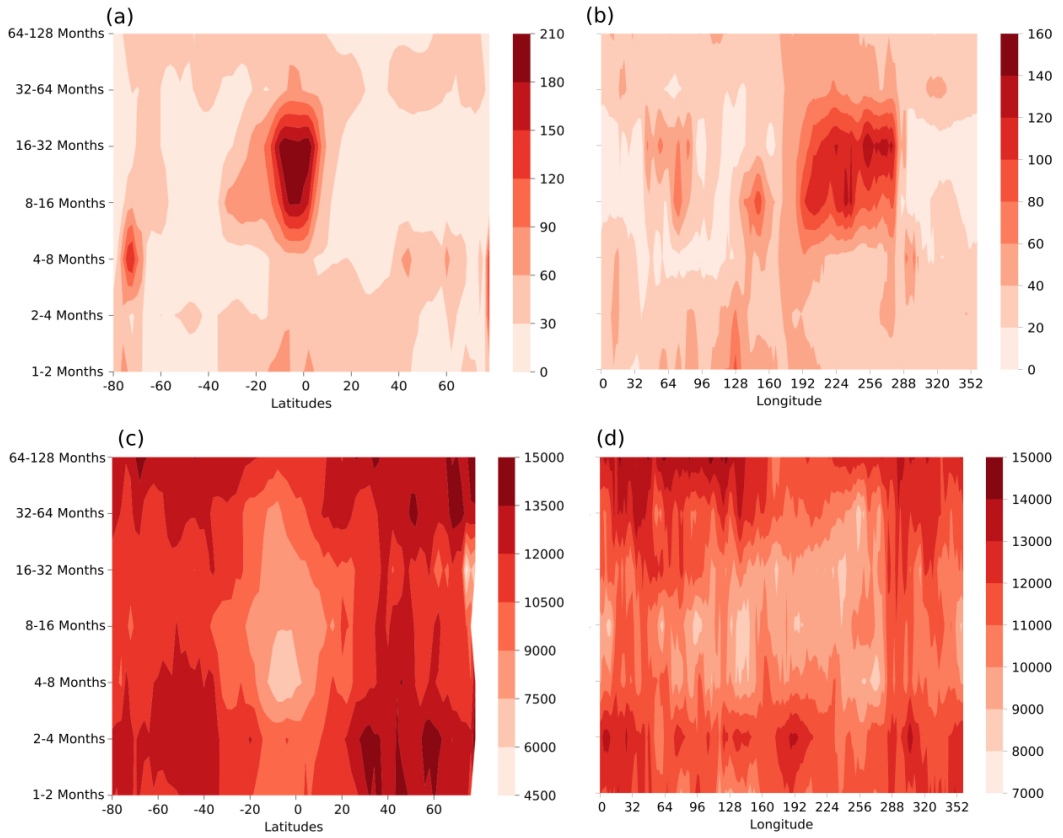

Figure 5.11.: Average zonal (a) and meridional (b) n.s.i. cross-degree from SST to the global precipitation field. (c,d) Same as (a,b) but for the n.s.i. cross-average link distance.

In this case, at their native (monthly) temporal resolution, the two considered climatological fields feature several pronounced spatial patterns that resemble ENSO, PDO and SAM, which are known to exhibit mutual interdependences. Given the prominent role of ENSO in global climate variability, the dominance of the eastern-to-central tropical Pacific is compatible with expectations. However, other (weaker) atmosphere-ocean co-variability features would be easily overlooked in this integral perspective. By decomposing the SST and PCP time series into distinct time-scales, one is able to trace the appearance and disappearance of different patterns that are related to seasonal over interannual up to decadal variability associated with large-scale climate phenomena. Thereby, I obtained a more explicit picture of other climate modes with different characteristic time-scales that might be important for understanding global precipitation patterns, which is a relevant task in the context of improving future long-term precipitation and drought forecasts.

The substantial variation of the SST-precipitation interdependence globally and across time-scales that is unraveled by the proposed framework provides an exciting perspective for understanding ocean-atmosphere coupling and resulting climate variability. Beyond climate, similar approaches are potentially useful in other fields as well, including neurophysiology [Perinelli et al., 2018] or economics, or generally for understanding multi-component complex systems and their spatio-temporal dynamics [Gupta and Ambika, 2018].

Part II.

Regional climate model sensitivity

Chapter 6.

Introduction

The second part of this thesis presents an investigation of the climatic effects of Lake Sobradinho (a large freshwater reservoir in Northeastern Brazil) using the COSMO model in CLimate Mode (COSMO-CLM or CCLM) [Rockel et al., 2008]. Lakes significantly affect the structure of the atmospheric surface layer and therefore the surface fluxes of heat, water vapor, and momentum. Lakes are characterized by an elevated heat capacity and thermal inertia, small roughness length and albedo [Bonan, 1995]. Several studies have demonstrated that the presence of lakes can impact near-surface meteorological conditions as well as meso or synoptic scale processes [Bates et al., 1993, Pielke, 1974, Pielke, 2002]. Typically, in the vicinity of lakes, surface moisture increases and the daily and annual range of the near-surface air temperature reducedes. In the fall and winter of temperate climates, the cold dry air moves over the warmer lakes surfaces causing high evaporation rates and subsequently cloudiness and precipitation. This situation is reversed in the summer when the cooler lakes surfaces stabilizes the overlying atmosphere leading to a reduction in clouds and precipitation. The local high-pressure centers over lakes in the summer can influence the atmospheric circulation and cause lake breezes [Bates et al., 1993]. Previous studies on the effects of tropical lakes on the regional climate, such as the Elqui Valley reservoir in an arid region of the Chile [Bischoff-Gauß et al., 2006] and the great African lakes [Thiery et al., 2014] confirm the aforementioned findings for lakes in the temperate climates regarding their effects on the near-surface air temperature and its diurnal cycle as well as increased precipitation.

Although studying the effect of lakes on the structure of the atmospheric surface, surface fluxes of heat, water vapour, and momentum is important, in the most numerical weather prediction (NWP) systems, the effect of lakes is either entirely ignored or is parameterized very crudely [Mironov et al., 2008]. There are two main problems regarding the modeling of a lake. Firstly, the interaction of the atmosphere with the underlying surface strongly depends on the surface temperature and how it changes during time. In modeling water surfaces, for seas and deep lakes, to some extent, it can be assumed that the water surface temperature can be kept 'frozen' over the forecast period. It is worth nothing that, this assumption is not justified in case of small-to-medium size relatively shallow lakes, where the short-term variations of the surface temperature (with a period of several hours to one day) reach the several degrees. Hence, a very high horizontal resolution is needed. In many NWP systems with coarser resolution, these small-to-medium lakes are considered

as sub-grid scale features. However, the presence of these lakes cannot be ignored due to their aggregate effect on the grid-scale surface fluxes. This also holds for the climate modeling systems concerned with time scales ranging from many days to many years [Mironov et al., 2008].

Secondly, lakes strongly modify the structure and the circulation properties of the atmospheric surface layer. To tackle this problem, a parameterization of the roughness of the water surface with respect to wind and scalar quantities, such as potential temperature and specific humidity is required [Mironov et al., 2008].

In order to solve the problems regarding the modeling of lakes in NWP and climate modeling systems, there have been several developments [e.g. Ljungemyr et al., 1996, Goyette et al., 2000, Tsuang et al., 2001]. Some models, neglect the lake thermocline, and use a complete mixing, down to the lake bottom and characterize the entire water column by a single value of temperature. This approach is computationally very cheap but comes at the expense of large errors in surface temperature. Others use turbulence closure models, e.g. models based on the transport equation for the turbulent kinetic energy [Tsuang et al., 2001], which is useful for describing the lake thermocline, but these models are computationally very expensive.

In this thesis, I use the regional climate model (RCM) CCLM to study the effect of the Lake Sobradinho on the regional climate. In CCLM, the FLake model (Freshwater Lake model) is applied for the computation of the lake's vertical temperature profile and the energy stored [Mironov et al., 2008] to address aforementioned problem. CCLM is the climate version of the COnsortium for Small scale MOdeling (COSMO) model [Baldauf et al., 2011], which is an operational numerical weather prediction model, based on the Local Model (LM) and is developed by the German Weather Service. CCLM has been extensively applied over Europe [Jaeger et al., 2008, Zahn and Storch, 2008, Hohenegger et al., 2009, Davin and Seneviratne, 2012], the Indian subcontinent [Dobler and Ahrens, 2010], the East Asia [Fischer et al., 2013], and Africa [Nikulin et al., 2012]. The latter two applications were spurred by the COordinated Regional climate Downscaling EXperiment (CORDEX) initiative [Giorgi et al., 2008].

The FLake which is used by CCLM is a bulk model capable of predicting the vertical temperature structure and the mixing conditions in lakes of various depth and on time scales from a few hours to many years. This lake model is based on a two-layer parameterization of the temperature profile, where the structure of the stratified layer between the upper mixed layer and the basin bottom, the so-called lake thermocline, is described using the concept of self-similarity of the evolving temperature profile [Kitaigorodsky and Miropolsky, 1970]. The same concept is exploited to describe the interaction of the water column with the bottom sediments and the evolution of ice and snow cover. This approach, which is based on 'verifiable empiricism', still incorporates much of the essential physics of lakes and offers a very good compromise between physical realism and computational economy.

Previously documented CCLM applications over South America have either focused on different aspects of the physical parameterizations within CCLM, like the soil hydrology [Böhm et al., 2003] and cloud parameterizations [Lange et al., 2015], or

on CCLM evaluations and comparison of model output with observations [Rockel et al., 2008, Wagner et al., 2012]. In turn, there has been a series of attempts to simulate the South American climate with other regional climate models. Some of these studies focused solely on the model evaluation [Nicolini et al., 2002, Seth and Rojas, 2003, Solman et al., 2013], while others provided regional climate projections based on greenhouse gas emission or land-surface change scenario runs of general circulation models [Correia et al., 2008, Marengo et al., 2010, Marengo et al., 2012]. With respect to the region of interest in this work (Northeastern Brazil), Melo et al. [Melo et al., 2015] used the numerical model RAMS (Regional Atmospheric Modeling System, version 8) to assess the environmental impact of the agricultural expansion on the natural Caatinga dominated landscape in the basin of the São Francisco River. In another case study on the Lake Sobradinho [Correia et al., 2006a, Correia et al., 2006b], the RAMS model was applied (at 2 km and 6 km resolution, respectively) for one-day simulations with and without the lake and irrigated crops. This part of this thesis systematically expands the original case study by Correia et al. [Correia et al., 2006a, Correia et al., 2006b] conducting the additional high resolution ($\sim$ 2km) simulations with the CCLM.

The results presented by Correia et al. [Correia et al., 2006a, Correia et al., 2006b] have been restricted to a single regional climate model (RCM) and a very short integration time, raising concerns regarding the general validity of the obtained results. To further address this problem, my work expands the original case study by Correia et al. [Correia et al., 2006a, Correia et al., 2006b] for the entire months of April and May of the two years of 1998 and 2002. The year 1998 has been characterized by very high air temperatures and low amounts of rainfall. Therefore, the lake effects are expected to be particularly strong in this arid region. On the other hand, during the year 2002, the observed air temperatures and rainfall represent the long-term average climatic conditions of the lake basin. As I mentioned earlier, to capture the effect of the lake, the one-dimensional lake model FLake was used together with CCLM. In order to provide highly resolved climate simulations, I first conducted long-term simulations (1979-2004) of the area with and without the lake at a spatial resolution of 11 km. The highly resolved 2 km runs have then simply been nested for the two selected periods of interest, implying that these short-term fine-grid simulations have been initialized and driven by long-term coarser-grid simulations with the same RCM. This strategy ensures that the model is in long-term equilibrium for the two study periods which indicate I can capture the possible long-term effects, even though I analyze only shorter episodes. In turn, I emphasize that analyzing climatological effects instead of effects at the weather scale would require simulations over 20-30 years on the finer grid, which would increase the numerical effort tremendously. However, a corresponding investigation has been beyond the scope of the present study.

The second part of this thesis is structured as follows. In chapter 6 I describe theoretical background relevant to this thesis in three separate sections. In the section 6.1 I present the theory behind numerical climate modeling CCLM is also based on, in the Section 6.2, I outline the idea of the physical parameterization in the context

of atmospheric modeling and describe the lake parameterization schemes available in CCLM. In the section 6.3 I explain the concept of regional climate modeling and give a general description of CCLM. Finally, in chapter 7, I present the design of the CCLM sensitivity/evaluation study for Lake Sobradinho and the corresponding results.

Chapter 7.

Theoretical background

7.1. Numerical atmospheric modeling

Numerical Weather Prediction (or NWP) represent the science of forecasting weather using governing physical equations of the atmosphere. Observing the current state of the atmosphere and employing complex equations for describing its processes, weather models can take steps forward in time. With modern computers, a vast amount of information about climate dynamics can be processed, and therefore weather models are becoming increasingly accurate.

Vilhelm Bjerknes, a Norwegian physicist, and meteorologist was the first to state that if the current state of the atmosphere can be accurately measured, then the governing equations of the fluid dynamics can be used to proceed forward in time, and forecast the following state of the atmosphere [Bjerknes, 2009]. He also mentioned the complexity of atmospheric equations (there is no exact solution for these equations) and that the accuracy of our measurements o the current state of the atmosphere impose difficulties for forecasting the subsequent state of the atmosphere.

Due to the complexity of the atmospheric equations, NWP was not quite successful until the invention of computers in the 1940s. Jule Charney successfully ran a numerical weather model over three layers of the atmosphere employing a simplified version of the governing equations of the atmosphere [Donner et al., 2011]. In 1958, a single-level numerical weather model was first used operationally by the weather forecasters at the US Weather Bureau. This weather model performed forecasts for an altitude of roughly 5 km above the sea level. The weather models have been becoming exponentially more complex since, as the present computational power has increased exponentially with time [Donner et al., 2011]. By 1966, forecasters could generate forecasts covering the Northern Hemisphere at a resolution of 380 km through a 6-level model which allowed implementation of the un-simplified (or 'primitive') equations [Donner et al., 2011]. By 1990, weather models were used over the whole globe, considering 18 levels in the atmosphere, and with an effective horizontal resolution of 160 km [Donner et al., 2011]. Methods of statistically adjusting the raw model data based on historical observational data from weather stations were also introduced [Coiffier, 2011].

In addition to the accurate modeling of the dynamical equations of motion, another crucial part of the modeling is data assimilation. Data assimilation represents the process of taking the initial state of the atmosphere, via provided weather stations,

balloons measurements, or satellite, and employing this data as a starting point for models. While being solely based on point measurements originally, in 1970s, different methods for assimilating satellite data into weather models were introduced. This was a significant step forward since by using only weather stations, areas of the globe with very few or no surface-based observations, like the oceans, were not represented sufficiently. on the other hand, satellite data provide much better coverage of the whole globe.

Another significant step for weather forecasting was considering the theory of chaos in numerical modeling. In 1961, Edward Lorenz noticed that a minor change in the initial state of the atmosphere could cause very different results in forecasting [Lorenz, 1963]. To address this problem, at 1992, the idea of model ensemble was introduced [Toth and Kalnay, 1997]. Without considering chaos, the weather models were deterministic in nature, starting with the initial state of the atmosphere, such that there would be only one possible future based on the equations. The chaotic nature of atmosphere was not considered in this method. Also, errors of observing and measuring the current state of the atmosphere were not included. On the other hand, an ensemble forecast is based on probability. This means that starting from an initial state of the atmosphere; the future state of the atmosphere can exhibit many solutions, each with different probabilities. To make an ensemble forecast, the deterministic model is used for multiple times, but each time, the initial state is changed slightly. With this approach, forecasters will obtain distribution of possible future states of the atmosphere and can then look for clusters within these solutions. This method extends forecast skill to the two-weeks range because it averages over many possible initial states, to essentially 'smooth' the chaotic nature of the atmosphere.

In the following, I briefly explain the primitive equations that has been proposed by Bjerknes [Bjerknes, 2009]. These equations are fundamental in numerical atmospheric modeling. The primitive equations are a set of nonlinear differential equations, which consists of three main balance equations: continuity equation, conservation of momentum equation, and thermal energy equation. Momentum equation describe the conservation of mass in the fluid. The conservation of momentum can be described as a simplified form of the 'Navier–Stokes' equations used for describing the flow of a fluid on the surface of a sphere. Last equation, thermal energy equation, describes the general temperature and its change due to heat sources and sinks in the system. These three equations can be written as follows:

(i) Momentum equation

$$\frac{\partial \vec{v}}{\partial t} + \vec{v} \cdot \nabla \vec{v} + 2\vec{\Omega} \times \vec{v} = \frac{-1}{\rho} \nabla p + \vec{g} + \vec{f}, \tag{7.1}$$

Here $\vec{v} = \vec{v}(\vec{x}, t)$ is the velocity vector of an atmospheric fluid in a rotating coordinate system; $\vec{\Omega}$ is the three-dimensional angular velocity vector (the velocity of a rotating frame, relative to an inertial frame); ρ is the density of an atmospheric fluid; p the

pressure; $\vec{g}$ is a gravitational acceleration vector in three dimensions; $\vec{f}$ is a three dimensional friction force and ∇ is a gradient operator in three spatial dimensions.

(ii) Continuity equation

$$\frac{\partial \rho}{\partial t} + \nabla \cdot (\rho \vec{v}) = 0. \tag{7.2}$$

Equation (7.2) shows that the rate of changes in a local density is equal to the negative of the density (mass) divergence. There is an alternative form for this equation that can be written as:

$$\frac{1}{\alpha}\frac{D\alpha}{Dt} + \nabla \cdot \vec{v} = 0, \tag{7.3}$$

where $\alpha = \frac{1}{\rho}$ which is called the specific volume. Total derivatives ($\frac{D}{Dt}$) can be written in a form of partial derivatives as:

$$\frac{D}{Dt} = \frac{\partial}{\partial t} + \vec{v} \cdot \nabla. \tag{7.4}$$

(iii) Thermal/energy equation

$$\frac{De}{Dt} = -p\frac{D\alpha}{Dt} + Q, \tag{7.5}$$

where e is the specific internal energy, which is a function of the temperature (T), and Q is the amount of heat per unit of mass. The last equation shows that the internal energy of a system is related to the amount of heat that is added to a system and the work that is done by that system. Note that the temperature is described as a function of space and time. For dry air, the specific heat at constant volume equals to $c_\nu \equiv e/T$. Therefore equation (7.5) is written as follows:

$$c_\nu \frac{DT}{Dt} = -p\frac{D\alpha}{Dt} + Q. \tag{7.6}$$

By performing a scale analysis for momentum equation [Holton, 1979], it becomes explicit that in synoptic dynamics, the Coriolis force and the pressure gradient term are dominant players. Retaining only these two terms for the horizontal part of equation (7.1), the first approximation, the *geostrophic* approximation, is written as:

$$-fv \approx -\frac{1}{\rho}\frac{\partial p}{\partial x}; \qquad fu \approx -\frac{\partial p}{\partial y}, \tag{7.7}$$

where $f \equiv 2\Omega \sin\phi$ is called the *Coriolis parameter*. It is worth noting that equation (7.7) is a *diagnostic* expression, and is used for explaining the relationship between the pressure field and the horizontal velocity in a synoptic scale disturbances for midlatitude systems. Equation (7.7) does not explicitly depends on time and therefore, the *geostrophic* approximation is not a *prognostic* expression and cannot be used

for predicting the evolution of the velocity field. Utilizing this approximation, the horizontal velocity field, called the *geostrophic wind*, can be defined as follows:

$$\vec{V_g} \equiv \vec{k} \times \frac{1}{\rho f} \nabla p. \tag{7.8}$$

Another approximation based on a scale analysis can be applied to the vertical part of equation (7.8), and is called the *hydrostatic* approximation which is written as follows:

$$\frac{1}{\rho} \frac{\partial p}{\partial z} \equiv -g. \tag{7.9}$$

This approximation shows, with a high degree of accuracy, the pressure at a specific point is approximately equal to the weight of the air column above that point. By introducing the *hydrostatic* approximation, one also can define a standard pressure $\bar{p}$ for the hydrostatic approximation as follows:

$$\frac{d\bar{p}}{dz} = \bar{\rho} g, \tag{7.10}$$

where $\bar{\rho}$ is a standard density. Note that by simplifying the vertical component of equation (7.1), the vertical winds are ignored. In other words, at a synoptic scale, these vertical winds are negligible.

7.2. Downscaling

Up to now what I discussed was the formulation of the numerical atmospheric modeling on the global scale. The Global climate models (GCM) are primary tools for investigating global change and can provide simulations of the present and past climate with reasonable accuracy. However for practical planing of local issues such as floads or droughts, a focus on regional and local scales is needed. For regional and local scale analysis, climate systems in smaller scale should be taken into account. To this regard, GCMs are not useful due to their coarse spatial and temporal resolutions [Wigley et al., 1990, Carter et al., 1994]. To address this problem, a so-called *downscaling* methods are applied to relate regional and local scales to the global scale [Grotch and MacCracken, 1991, Von Storch et al., 1993, Wilby, 1994, Kattenberg, 1996]. *Downscaling* method can be categorized into four groups: regression method, weather pattern-based approaches, stochastic weather generators and limited area modeling (LAM) [Wilby and Wigley, 1997]. Among these four methods, regression method is the easiest to implement. In this method, and also in a more sophisticated version of it like the artificial neural network (ANN), a linear or nonlinear relationship between the regional-scale atmospheric variable and the coarser-scale variable is established. On the other hand, LAMs are embeded into GCMs and use the GCMs outputs as the boundary conditions to capture small-scale atmospheric processes. Although LAM is very appealing for climate change impact studies, it requires considerable computing resources which consequently make it hard to employ it

frequently. Furthermore, in LAM, GCM grid point data is used as a *lateral boundary* [Dickinson et al., 1989, Giorgi, 1990]. Therefore, this approach is limited by the accuracy of GCMs.

7.3. Grid representation

Not only for LAM but also for GCM, a great amount of computer processor time, memory and disk storage are required. Therefore there is a limit to obtain an accurate picture of the Earth from climate models. In climate models, a three dimensional set of spatial points, called *grid* is used to study climate at the global scale or for a specific region of interest. To take the spherical shape of the Earth into account and present equations correctly and efficiently, different grid types were introduced, e.g., the rectangular, triangular, and hexagonal grid whereby and each of them has its own limitations in representing the spherical nature of the Earth (Fig. 7.1) [Washington et al., 2009, Collins et al., 2013].

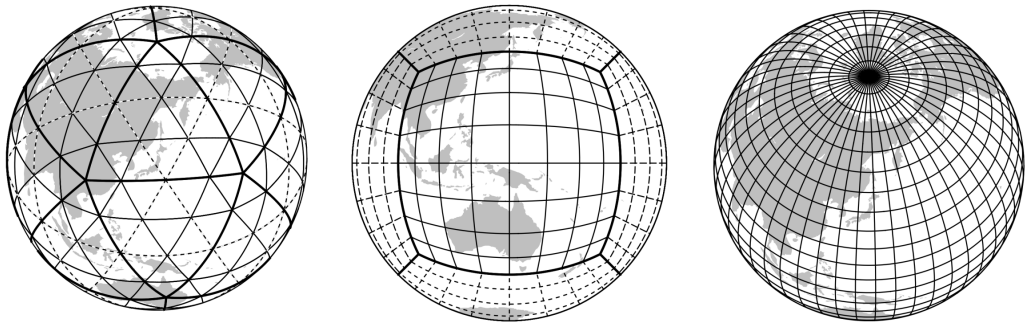

Figure 7.1.: Example of an icosahedral grid (left), cubed sphere grid (middle) and a spherical grid (right). Adopted from Washington et al. (2009).

7.4. Lake parameterization

In this section, I will briefly explain the main idea of parameterization of small scale climatic variable in climate models and specifically its implementation for the inland waters, e.g., freshwater lakes.

In the numerical modeling, there are always some physical processes that cannot be represented, no matter how fine the scale used [Stensrud, 2009]. However, to have an accurate forecasting, these processes must be included. To address this challenge, parameterization methods are used in numerical models. The parameterization is a process of representing unresolved physical processes by relating them to variables known by a model. Examples of such unresolved processes include the movement of the radiation through the atmosphere, which affects the temperature, or the formation of clouds which leads to rainfall. These examples represent molecular processes that cannot be handled by numerical models [Stensrud, 2009]. Parameterization can be

specified in various ways (different parameterization scheme closures). For instance, to capture the effect of solar radiation, its relation to cloud cover or water vapor can be exploited. In the similar manner, the number of cloud droplets can be related to the relative humidity, and then cloud droplets can be related to the formation of raindrops [Stensrud, 2009]. Therefore, parameterization is useful to obtain a more proper understanding of complex physical processes in the atmosphere by looking at their fundamental forms.

Here, I specifically explain the lake parametrization used in CCLM to capture the effect of freshwater lakes on the regional climate. The parameterization of lakes is a part of a larger group of parameterization schemes, called *Land surface-atmosphere* parameterization. Various types of the Earth surface and also deep soils have specific time scale to affect processes within the atmosphere, directly or indirectly. The Earth surface and the atmosphere are coupled to each other through various physical processes like precipitation, radiation and turbulent transfer of heat and momentum and therefore can influence each other. As a result, different components should be implemented within numerical models to capture these mechanisms and track their evolution through space and time. High-density materials like soil and water, typically exhibit much longer memory than the atmosphere. This long memory causes the temperature and the humidity to evolve on larger timescales within the deep soil (and water) [Viterbo, 2002]. Note that in the soil, the horizontal heterogeneity is not fully captured within numerical models and the observational data are also very scarce.

Although both water surfaces and soils possess long memory, water bodies like lakes or sea have very different surface characteristics. Hence they need to be presented in climate models with different parameterizations. Usually in numerical modelings, for oceans, seas, and large-deep lakes, due to their large inertia it is assumed that the air temperature above them is constant. However, the situation is different for the shallower water bodies since their thermal inertia is much smaller than for large water bodies. FLake is a parameterization scheme for considering shallow lakes in numerical models [Mironov et al., 2008].

As I mentioned earlier in chapter 5 the one-dimensional FLake model is applied for the computation of a lake's vertical temperature profile and energy budget [Mironov et al., 2008]. In FLake, a top mixed layer with a uniform water temperature profile as well as a thermocline layer at the bottom of the lake are assumed. The temperature of the thermocline layer is parameterized according to the concept of *self-similarity* [Kitaigorodsky and Miropolsky, 1970]. FLake provides simulations of the average temperature of the water column, the mixed-layers temperature and depth, and the thermocline layer's temperature profile [Mironov et al., 2008]. In following, I present a brief overview on the formulation of FLake.

In order to capture the state of the freshwater, a quadratic equation is used:

$$\rho_w = \left[1 - \frac{1}{2} a_T (\theta - \theta_r)^2\right] \tag{7.11}$$

where ρ_w is the water density, the maximum density of freshwater at $\theta_r = 277.13K$ is $\rho_r \approx 1.0 \cdot 10^3 kg \cdot m^{-3}$. a_T is called the empirical coefficient [Farmer and Carmack, 1981] and is equal to $1.6509 \cdot 10^{-5} K^{-2}$. The thermal expansion coefficient α_T can be related to the buoyancy parameter β such that:

$$\beta(\theta) = g\alpha_T(\theta) = g\alpha_T(\theta - \theta_r) \tag{7.12}$$

where $g = 9.81 m \cdot s^{-2}$ is the acceleration due to gravity.

To obtain the evolving temperature of the water in verrtical direction, the FLake utilize the two-layer parameterization as follows [Mironov et al., 2008]:

$$\theta = \begin{cases} \theta_s & \text{at } 0 \leq z \leq h. \\ \theta_s - (\theta_s - \theta_b)\Phi_\theta(\zeta) & \text{at } h \leq z \leq D, \end{cases} \tag{7.13}$$

where $\Phi_\theta \equiv (\theta_s - \theta)/(\theta_s - \theta_b)$ is a dimensionless function of the dimensionless depth $\zeta \equiv (z - h)/(D - h)$. $z = h$ is the upper layer of the mixed layer and $z = D$ is the basin bottom. Equation (7.13) relate h, D, θ_s, θ_b to the mean vertical temperature of the water body $\bar{\theta} \equiv D^{-1} \int_0^D \theta dz$ through following equation:

$$\bar{\theta} = \theta_s - C_\theta(1 - h/D)(\theta_s - \theta_b), \tag{7.14}$$

where

$$C_\theta = \int_0^1 \Phi_\theta(\zeta) d\zeta, \tag{7.15}$$

is the shape factor. Using equation (7.13), heat transfer equation can be written as follows [Mironov et al., 2008]:

$$\frac{\partial(\rho c \theta)}{\partial t} = -\frac{\partial(Q + I)}{\partial z}, \tag{7.16}$$

where Q is the vertical turbulent heat flux and I is the heat flux caused by the short-wave radiation. The total heat budget can computed by integrating equation (7.16) over z from 0 to D such that:

$$D\frac{d\bar{\theta}}{dt} = \frac{1}{\rho_w c_w}[Q_s + I_s + Q_b - I(D)]. \tag{7.17}$$

c_w is specific heat of water and Q_s and I_s are the value of Q and value of I at the surface of the lake. Q_b is the heat flux through the lake bottom. I_s represents the amount of short-wave radiation that comes from the atmosphere multiplied by $1 - \alpha_w$ where α_w is the albedo of the water surface with respect to the short-wave radiation [Mironov et al., 2008]. On the other hand, the sensible heat flux, the latent heat flux and the net heat flux due to the long-wave radiation are all summed up in Q_s. Note that the long-wave radiation is calculated based on the surface air layer parameters, the cloudiness, and the surface temperature.

In order to have the temperature budget in the mixed layer, by integrating equation (7.16) over z from 0 to h one gets:

$$D\frac{d\theta_s}{dt} = \frac{1}{\rho_w c_w}[Q_s + I_s + Q_h - I(h)], \tag{7.18}$$

where Q_h is the heat flux at the bottom of the mixed layer. Note that in equations (7.14), (7.17) and (7.18), there are seven unknown parameters, h, $\bar{\theta}$, θ_s, θ_b, Q_h, Q_b, and C_θ which are written in the terms of Q_s and I_s. Q_s and I_s are either derived from observation or atmospheric models [Mironov et al. (2008)].

Furthermore, by assuming the mixed layer deepening $\frac{dh}{dt} > 0$ in a self-similar form, the profile of the turbulence heat flux within the thermocline can be obtained as follows [Filyushkin and Miropolsky, 1981, Tamsalu et al., 1998]:

$$Q = Q_h - (Q_h - Q_b)\Phi_Q(\zeta) \qquad \text{at } h \le z \le D. \tag{7.19}$$

Equation (7.19) shows that in the oceans (and atmosphere) in which the mixed layer and the thermocline develop above a deep stable or neutrally stratified passive layer, the temperature profile and the turbulent heat flux are both described by a the similar shape factor, i.e. $\Phi_\theta(\zeta) = \Phi_Q(\zeta)$. However, in shallow lakes, the thermocline usually extends from the bottom to the mixed layer, and although the heat flux exhibits self-similar behavior, its shape factor has a different relation to the shape factor of the temperature profile [Mironov et al., 2008].

One can rewrite heat transfer equation with respect to equations (7.13) and (7.19) by first integrating equation (7.16) over z' from h to $z > h$ and then integrating the result over z from h to D as follows:

$$\frac{1}{2}(D-h)^2\frac{d\theta_s}{dt} - \frac{d}{dt}[C_{\theta\theta}(D-h)^2)(\theta_s - \theta_b)] = \frac{1}{\rho_w c_w}\Big[C_Q(D-H)(Q_h - Q_b) + (D-h)I(h) - \int_h DI(z)dz\Big],$$

where

$$C_Q = \int_0^1 \Phi_Q(\zeta)d\zeta. \tag{7.20}$$

is the shape factor of the heat flux. and

$$C_{\theta\theta} = \int_0^1 d\zeta \int_0^{\zeta'} \Phi_\theta(\zeta')d\zeta'. \tag{7.21}$$

is a dimensionless parameter.

Note that in the case of a stationary mixed layer, equation (7.19) is not valid any more and the bottom temperature is considered to be 'frozen',

$$\frac{d\theta_b}{dt} = 0. \tag{7.22}$$

Then, by assuming $h = D$, one can conclude $\theta_b = \theta_s = \bar{\theta}$ and the mean temperature is obtaind via equation (7.17) [Mironov et al., 2008].

7.5. Short overview of CCLM

CCLM belongs to the category of LAMs or regional climate models (RCMs). As I discussed earlier in section 7.1, LAM is one of the ways of downscaling to capture subgrid processes in numerical modelings. In this method, GCM outputs are used as the *lateral boundary* [Dickinson et al., 1989, Giorgi, 1990]. In one-way nesting approach, the LAM model output is used as an input for GCM [Dickinson et al., 1989]. The one-way nesting is much simpler than two-way nesting where the LAM and the GCM run in parallel to feed each other [Phillips and Shukla, 1973]. However, the one-way nesting suffers from unresolved interactions between the LAM scale and the GCM scale due to the different spatial resolutions, dynamical processes, and parameterization schemes, which can bring inconsistencies in LAM domain boundaries [Zhang et al., 1986, Warner, 1989]. Note that this problem occurs in the two-way nesting as well. To tackle this problem, Davies (1976) introduced the concept of 'sponge zone'. The sponge zone is formed by considering n outer grid points of LAM. By moving along the sponge zone across, LAM output merge into the GCM which leads to a smooth transition between two different grid size. Hence a new form for each prognostic variable ψ is obtained by adding an extra term as follows:

$$\Big(\frac{\partial\langle\psi\rangle}{\partial t}\Big)^{lateral\ boundary} = \mu_i(\langle\psi\rangle^{lateral\ boundary} - \langle\psi\rangle) \qquad , \tag{7.23}$$

where $\langle\psi\rangle^{lateral\ boundary}$ represents the boundary data and μ_i decays exponentially with the grid-cell distance $i = 1, ..., n$ towards the domain edge. CCLM also utilizes this approach.

In this thesis, I used the version 4.25.3 of CCLM which has about 300000 lines of code in FORTRAN and 300 name-list parameters. For running CCLM I used 256 processors of PIK high-performance cluster, which can simulate one year in roughly one day. Due to a high cost of computations, it is clear that any initial guess of model parameters for the optimum setup is impossible. One can only have insight into physical processes and understand how the parameterization of different processes works to find the optimal setup. The horizontal resolution of CCLM is in the order of 1 km and at this high resolution, the hydrostatic approximation is not valid anymore. For this reason, the CCLM is a nonhydrostatic model. The equations within CCLM are discretized on a rotated spherical coordinate system to have a regular grid within the simulation domain (Fig. 7.2). Normally, in CCLM, the Poles are tilted and therefore the Equator runs through the center of the desired domain. Moreover, CCLM uses the terrain-following vertical coordinates, which considers a flat atmospheric layer at some predefined height, and the flatness gradually decreases by going down to the surface of the Earth (Fig. 7.3).

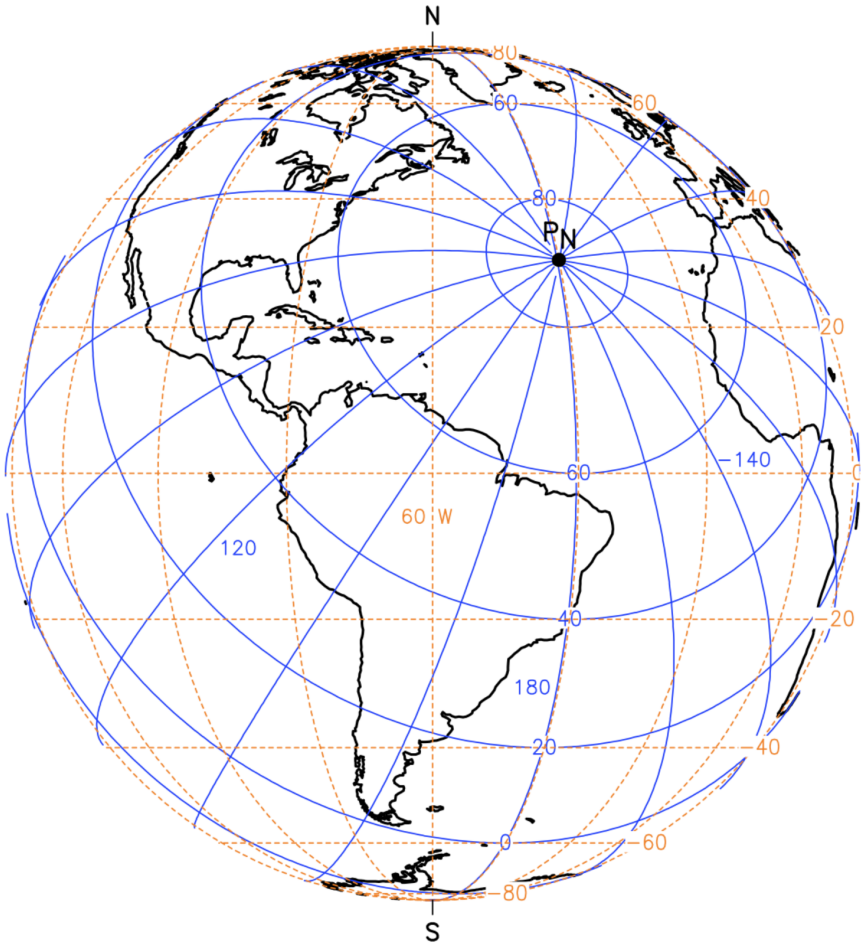

Figure 7.2.: An expample of a Rotated spherical coordinate system (solid blue). The North Pole is tilted to 30°N and 40°W. The geographical coordinate system is shown with broken orange line. Adopted from Doms and Schättler (2002).

The numerical approach for solving differential equations in CCLM is based on a finite difference numerical scheme. Model variables are presented based on the Arakawa-C/Lorenz grid (Cushman-Roisin and Beckers, 2011; Lorenz, 1960), so that scalars such as $\langle\rho\rangle$, $\langle c_\nu\rangle$, $\langle p\rangle$, and $\langle T\rangle$ are defined at grid volume centers while three velocity components in the zonal $\langle u\rangle$, meridional $\langle v\rangle$, and vertical $\langle w\rangle$ directions are defined at grid volume faces, i.e., halfway between centers. There are also several time-integration methods implemented in CCLM. I used a total variation diminishing version of a 3rd order Runge-Kutta split-explicit scheme [Liu et al., 1994, Doms and Schättler, 2002].

CCLM deploys the FLake model for lake parameterization. In FLake, the default downward light attenuation coefficient for incoming solar radiations is $3\mathrm{m}^{-1}$. Global bathymetry dataset [Kourzeneva, 2010] is used to determine the lake's depth for each

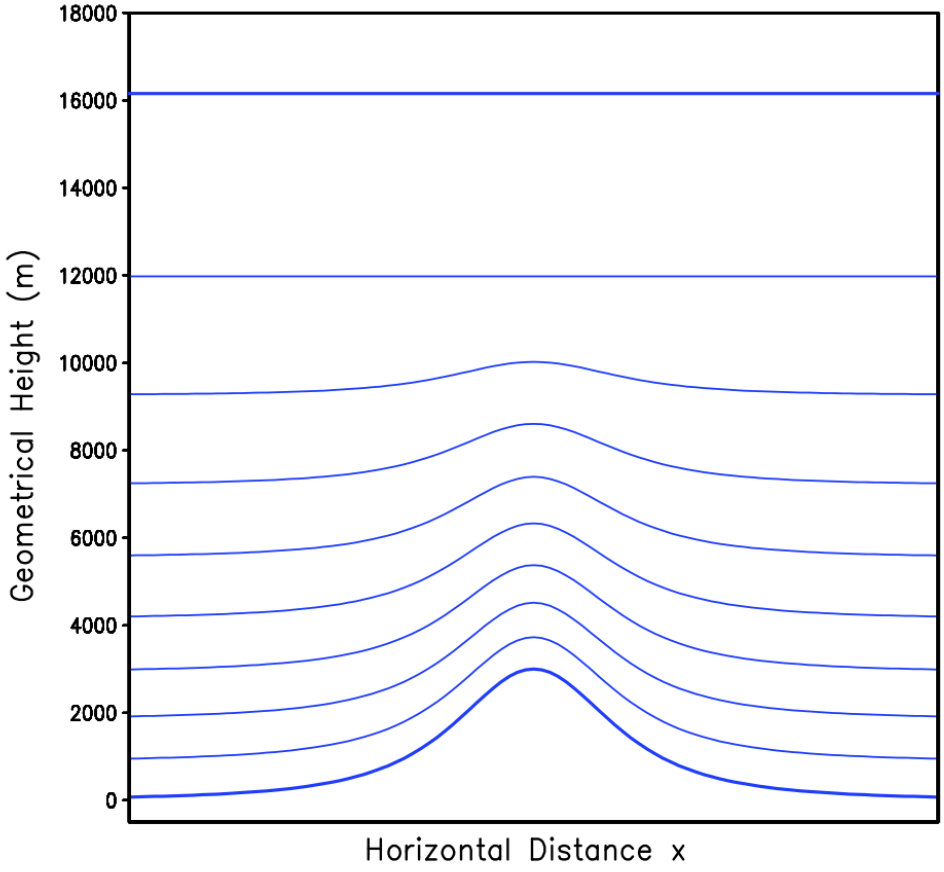

Figure 7.3.: A schematic diagram of a vertical coordinate over a bell-shaped mountain. Adopted from Doms and Schättler (2002).

modeled grid cell (maximum 50m). Besides FLake, other physical parameterizations are included such as sub-grid scale turbulence [Raschendorfer, 2001], grid-scale clouds and precipitation [Doms and Schättler, 2002], delta-two stream radiation transfer [Ritter and Geleyn, 1992], and the shallow and moist convection based on the Integrated Forecasting System (IFS scheme, [Bechtold et al., 2008]). Lower boundary conditions over the land (i.e., land surface and soil processes) are simulated by the multi-layer soil model TERRA-ML [Schrodin, 2001]. The soil-vegetation water balance is modeled according to the biosphere-atmosphere transfer scheme (BATS) [Dickinson et al., 1986]. The richards and heat conduction equations are solved to simulate the vertical soil moisture transport and heat flow. Note that only vertical fluxes are represented in TERRA-ML, as the horizontal displacement can be neglected at presently used grid sizes. This also holds for the runoff formed within a grid cell and not transported to any of adjacent cells. TERRA-ML provides a stability and roughness length dependent formulation of the surface turbulent fluxes which

constitute lower boundary conditions for the atmosphere. Surface runoff is formed by summarizing contributions from the interception store, the surface snow store, and water due to a limited infiltration rate into the soil. Furthermore, contributions from hydrologically active soil layers in the case of over-saturation are added to represent the subsurface runoff. Soil types are based on the UNESCO/FAO (Food and Agriculture Organization of the United Nations) soil map of the world [Unesco, 1974]. Here, the number of soil levels is set to 10, with layer thickness increases with soil depth from 0.005 m to 11.5 m, following an exponential law, and representation of hydrology stops at 8 m depth.

The primary goal of this part of the thesis is evaluating to what extent the output of CCLM as a numerical atmospheric model is comparable to observations. Note that one should not mistake evaluation with validation. Since all scientific models have flaws and defects, the unique term that shall be used for observing various models is evaluating them based on observations. The term evaluation is used based on Oreskes [Oreskes (1998)] who propose using the term, *model evaluation* which sounds more logical and imply a less positive level of confidence that term validation in model quality. Since the beginning of the numerical atmospheric modeling, scientists constantly have tried to compare simulations based on models with real observations [Donner et al., 2011]. There are many methods to investigate to what extent, results from a model resemble the observation. The further step of this study is a simulation. There are several ways for performing a model simulation such as adjusting the external forcing (increased/decreased solar radiation, atmospheric $CO2$ concentrations, a volcanic dust layer, etc.), changing surface boundary conditions (orography, land surface albedo, continental ice sheets), or modifying the model physical parameterization (the convective scheme or treatment of biosphere exchanges). In this thesis I adjust the external forcing by replacing a lake with soil and investigate how the climate will be affected by this scenario.

Chapter 8.

Application

8.1. Effects of the Lake Sobradinho Reservoir (Northeastern Brazil) on the Regional Climate

In this study, I investigate the effects of the Lake Sobradinho reservoir on the regional meteorological conditions. To this end I use CCLM as I described in section 7.5 to carry out simulation studies without and with the lake. When the lake is excluded from the simulations, it is replaced by solid ground with the characteristics of representative grid cells from the surrounding land surface. Each simulation has been done once for an extremely dry year and once for an 'average' (non-extreme) year.

This chapter is primarily based on the study that is presented in P1 [Ekhtiari et al., 2017].

8.1.1. Setup and data

CCLM setup: I use CCLM version 4.25.3 with two domains, one of 0.1° (about 11 km) and one of 0.02° (about 2 km) spatial grid spacing (enclosed areas in Fig.8.1). In a rotated longitude/latitude geographical coordinate system (rotated North Pole at $\varphi = 80°\text{N}, \lambda = 41.8°\text{W}$), the higher resolution modeling domain extends from 2.26°S to 2.24°N and 2.26°W to 2.24°E and is covered by 226×226 grid cells. 50 vertical levels are used so that at level 50, the atmospheric boundary is considered to be flat. The internal time step for solving the physical equations in the model is set to be 25 s. The initial six-hourly boundary conditions are provided by the ERA-Interim reanalysis [Dee et al., 2011]. In order to exclude lateral boundary effects from the analysis, I discard the sponge zone which has a width of 10 grid points. This zone doesn't really represent model dynamics; it is un-physical as it tries to smooth out any pathological effects due to discontinuities at the boundary between two completely different grid sizes.

Since the main goal of this study is investigating the effect of the Lake Sobradinho reservoir, I need to apply lake parameterization to include the physical processes that happen within the lake and the interaction between the lake and the atmosphere above it. For this purpose, I use the Flake model (see, e.g., section 7.5). All other parameterizations schemes that are implemented in the setup of CCLM have been described in section 7.5.

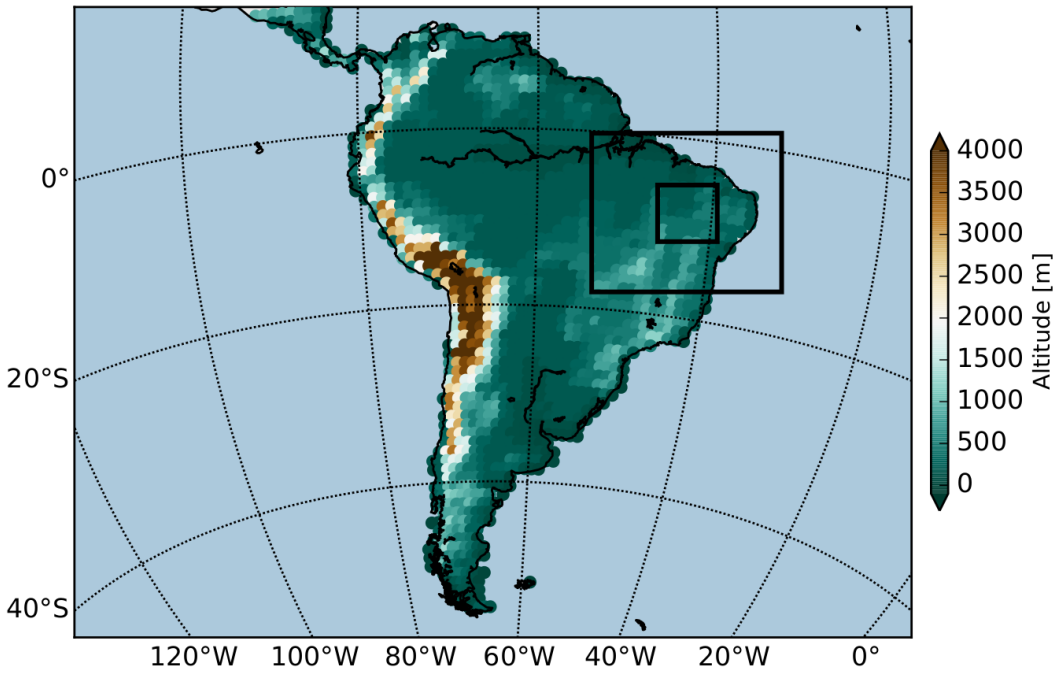

Figure 8.1.: Schematic view of our nesting steps. The larger enclosed area corresponds to a $0.1°$ resolution and the smaller one to a $0.02°$ resolution of CCLM in the respective regions (in rotated coordinates as described in the text).

Climatological Setting: In this section I will first give a short overview of the Lake Sobraddinho. Following the description of Lake Sobradinho, I explain which years I chose to use for model simulation and evaluation.

Lake Sobradinho is located in the semi-arid sub-middle São Francisco river basin (near Petrolina, Pernambuco). The state of Pernambuco is one of the nine federative states forming the Northeast of Brazil. The Northeast of Brazil represents 18% of the national territory of Brazil. With a total area of almost 1.6 million km^2 , it is among the regions most vulnerable to impacts of climate change. This is due to its semi-arid climate in combination with a high population density [Marengo, 2010]. The region Semiárido brasileiro represents approximately 58% of the surface of Nordeste do Brasil [Integração Nacional, 2005] (excluding the State of Maranhão) plus the northernmost part of the State of Minas Gerais, extending from about 3°S to 17°S. Principal characteristics of this region are an annual precipitation fluctuating between 400 and 800 mm, mean air temperatures above 23°C, and evapotranspiration above 2000 mm/year. The living conditions of the population and the region's potential for agricultural production are directly connected to the availability of water [Araújo, 2011]. Specifically, the São Francisco river basin is of key importance in this context.

Lake Sobradinho is a man made reservoir that was installed in 1982 and replaced the natural Caatinga vegetation cover, a mix of shrubs, low trees and cactuses.

Precipitation mainly occurs from November to April. With a length of 280km and a varying width of 5 km to 50 km, Sobradinho's water storage capacity is 34 billion m^3. It's surface area is large enough to potentially influence regional weather and climate, particularly in combination with large areas of irrigated agricultural land to which the natural Caatinga was converted as a result of a governmental irrigation program.

For choosing an extremely dry year and an average (non-extreme) year, I analyzed 2 m air temperature data from the meteorological station at Petrolina (9°22′S, 40°28′W, see Fig8.2 for details) for the years 1981 to 2004. Observational data for precipitation for the years 1998 to 2004 were obtained from the Tropical Rainfall Measuring Mission (TRMM) data set [Huffman et al., 2007]. I calculated the mean air temperature and precipitation values for April and May for each of these years. From that, I determined the median and maximum values of the April/May air temperatures and precipitation taken over all these years. The median values coincide very well with the values obtained for the year 2002, 25.06°C and 0.024 mm/day, respectively, which is therefore considered as a prototypical normal year. In turn, extremely warm and dry conditions have been observed in 1998 for which average air temperature and rainfall amount to 27.07°C and 0.006mm/day, respectively. As mentioned in a previous study on Lake Sobradinho [M. D. F. Correia and Dias, 2003], the long-term mean of the surface lake temperature is 26°C. It is noteworthy that 1998 was rated an extremely dry year in Submédio San Francisco by the rainfall anomaly index (IAC), very likely affected by the strong El Niño event of 1997/98, which caused a decrease in rainfall and rising air temperatures in the Northeast of Brazil [Assis et al., 2015].

Observational Data for Model Evaluation: For the evaluation of modeled air temperature and wind speed, I use observational data from surface weather stations. The data were collected at a total of seven meteorological stations located in the surroundings of the lake (Fig. 8.2), covering the westernmost part of the State of Pernambuco (PE) northeast of the lake as well as the northern part of the State of Bahia (BA): Petrolina-PCD/PE (9°9′S, 40°22′W; here, PCD stands for Plataforma de Coleta de Dados) and Araripina-PCD/PE (7°27′S, 40°24′W) belong to INPE (Instituto Nacional de Pesquisas Espaciais) [32], the National Institute for Space Research, which is a unit of the Brazilian Ministry of Science and Technology. Bebedouro–Petrolina/PE (9°9′S, 40°22′W) and Madacarú-Juazeiro/BA (9°24′S, 40°26′W) are operated by EMBRAPA/CPATSA [33], the Tropical Semi-Arid Research Center of the Brazilian Agricultural Research Corporation. Finally, I use data from three stations operated by INMET (Instituto Nacional de Meteorologia) [34], the National Institute of Meteorology: Petrolina/PE (9°22′S, 40°28′W), Barra/BA (11°05′S, 43°10′W) and Remanso/BA (9°38′S, 42°1′W). The data include daily values of maximum and minimum air temperature, humidity and wind velocity. For 1998, I used data from all stations except Petrolina-PCD/PE, while for 2002, data from the Araripina-PCD/PE station were not available.

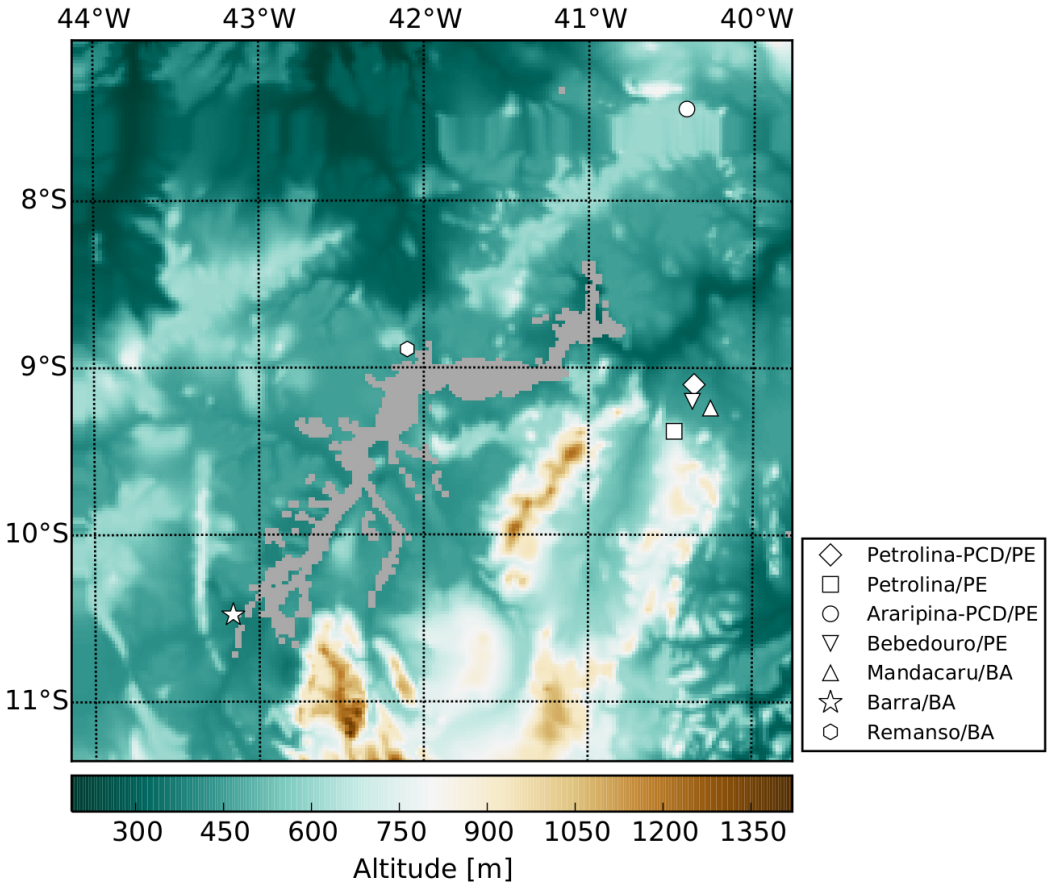

Figure 8.2.: Geographical setting and meteorological stations used for model evaluation. The gray area represents the geographical extent of Lake Sobradinho.

8.1.2. Results

8.1.2.1. Model Evaluation

I applied CCLM to simulate the evolution of various meteorological variables during the two periods of interest. At the coarser spatial scale, I utilized a long simulation starting back in 1979 and covering the whole period of interest of this work. In turn, the two nested simulations at the finer grid started at 1 January 1998 and 1 January 2002, respectively, resulting in a sufficiently long spin-up time of the model (i.e., the simulation period after which transient effects due to imperfect initial conditions can be neglected) of four months each prior to our analysis periods.

I first evaluate our simulation results by comparing the simulated average bi-monthly diurnal cycles of 2 m air temperature (T_{2m}) and 3 m wind speed (V_{3m}) with the corresponding three-hourly observations for each of the two two-month study periods. For this purpose, the model results at the grid points closest to the respective reference station were averaged for each hour of the day for the months

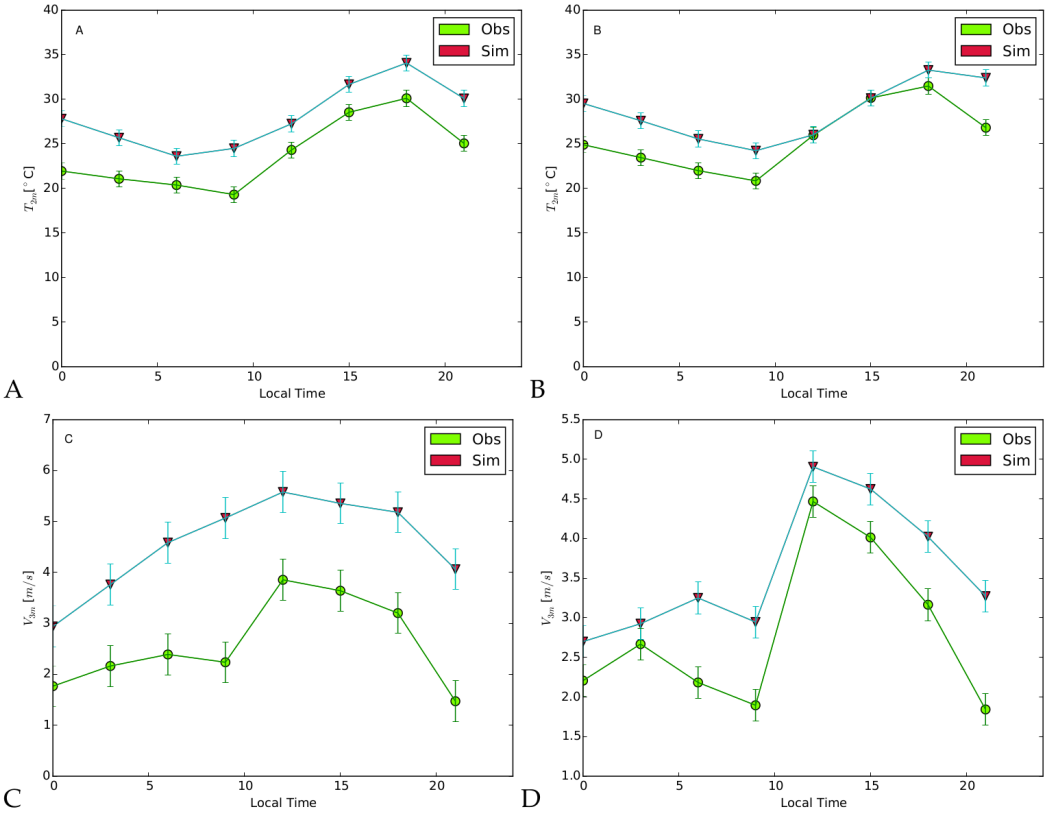

Figure 8.3.: Average diurnal cycles of observed and simulated (A,B) 2m air temperatures (T_{2m}) and (C,D) 3m wind speeds (V_{3m}) for (A,C) 1 April- 31 May 1998 (Araripina/PE station) and (B,D) 1 April- 31 May 2002 (Petrolina/PE station).

of April and May. For the years 1998 and 2002, data from the Araripina/PE and Petrolina/PE stations were used, respectively, which have a temporal resolution of 3 hours (as opposed to the other stations where only daily data have been available). The results are shown in Fig.8.3. For the year 2002, CCLM approximately reproduces the diurnal cycles of T_{2m} and V_{3m} in the station data. In turn, for 1998, the shapes of the cycles are reproduced well, but the magnitudes are overestimated by CCLM. For air temperature, I found around 4°C overestimation and for wind speed, the results are about 1.5 times larger than the observation data.

To handle this overestimation, note that in climate modeling, one generally assumes that model errors are approximately constant across simulations. Therefore, it is customary to regard anomalies from simulations as valid output, even though the simulated baselines might be somewhat off. Considering only variations around the baseline and ignoring the systematic offset can be considered as the simplest possible strategy of bias correction, which is often referred to as the delta change method [Gleick, 1986; Arnell, 1996; Hay et al., 2000].

Also I have only point observations and only simulated regional atmospheric conditions for a period of a few months. I tried to exclude influences of initial conditions by using a long spin-up (see above), but some uncertainties remain. These facts already imply a possible mismatch between the observations and simulation results. Furthermore, I have chosen an extreme period, which is typically harder to reproduce by an RCM than an average period. The missing shading effect could also be a reason for the discrepancy. TERRA-ML does not account for the shading effect of the vegetation. This can easily produce biases of the observed order, depending on the specific station's setup. In summary, I emphasize that the study region is known to be challenging for climate modeling in general [M. D. F. Correia and Dias, 2003]. In this regard, my results can be considered as in line with the state of the art.

Table 8.1 lists the root mean square error (RMSE) and bias (i.e., the root mean squared and mean differences, respectively, between all daily values in the model and observations for the respective periods of time) of the simulated daily mean, maximum and minimum values of 2m air temperature as well as the 3m wind speeds in comparison with observed data for the period of 1 April– 31 May of the years 1998 and 2002.

8.1.2.2. Lake Effects on Near-Surface Meteorological Conditions

In the following, I present the results of our CCLM-based study regarding the effects of Lake Sobradinho on the near-surface meteorological conditions and surface energy fluxes. For all considered variables, mean values over the two entire simulation periods (1 April–31 May 1988 and 1 April–31 May 2002) are presented.

Warm and dry conditions: April/May 1998: I start with considering the more extreme conditions of the year 1998. Figure 8.4 shows the spatial patterns of the simulated daily minimum, maximum and mean 2 m air temperatures ($T_{2m,min}$, $T_{2m,max}$, $T_{2m,mean}$) for the simulations without the lake (Fig.8.4A,E,I) and the difference plots for the simulations with lake minus without lake (Fig.8.4B,F,J). The presence of Lake Sobradinho with its large heat capacity causes $T_{2m,min}$ to increase by up to 2 deg C during night. As will be shown later, this is accompanied by an increase in the nighttime sensible heat fluxes. Additionally, I find that the values of $T_{2m,min}$ over the lake are higher than those in the surrounding natural area by about 1.5 deg C. This can be understood by the fact that the study area is an arid region with dry soils that are characterized by small heat storage capacity and the resulting differential cooling at nighttime. Lake Sobradinho also affects $T_{2m,max}$ in the simulations (Fig.8.4E,F) by reducing the corresponding values by up to 7 deg C. Cooler air is advected towards the region northwest of the lake, cooling this area by up to 3 deg C. Taken together, the presence of the lake leads to a reduction in daily mean air temperatures, $T_{2m,mean}$ (Fig.8.4I,J) by up to 2 deg C and also to lower $T_{2m,mean}$ values in its surrounding.

Year		**1988**									
Station		**Petrolina/PE**		**Mandacarú/BA**		**Bebedouro/PE**		**Barra/BA**		**Remanso/BA**	
Month		**April**	**May**	**April**	**May**	**April**	**May**	**April**	**May**	**April**	**May**
$T_{2m,mean}[^{\circ}\mathrm{C}]$	RMSE	1.61	0.92	1.53	1.06	2.29	1.52	-	-	-	-
	Bias	−1.22	−0.52	−1.16	−0.77	−2.04	−1.28	-	-	-	-
$T_{2m,min}[^{\circ}\mathrm{C}]$	RMSE	1.59	1.0	2.36	3.32	1.82	1.40	4.7	4.33	3.67	2.67
	Bias	−1.13	0.01	−1.99	−2.77	−1.2	−0.45	−4.5	−4.13	−3.21	−2.01
$T_{2m,max}[^{\circ}\mathrm{C}]$	RMSE	2.58	2.03	1.87	3.2	2.48	2.15	2.32	1.28	2.02	3.02
	Bias	−1.98	−1.42	−1.18	−2.3	−1.82	−1.3	−1.84	0.01	−1.88	−2.7
$V_{3m}[\mathrm{ms}^{-1}]$	RMSE	-	-	2.56	2.7	2.02	1.75	0.96	0.87	3.47	3.38
	Bias	-	-	2.37	2.5	−1.91	−1.62	−0.5	−0.22	−2.97	−2.82
Year		**2002**									
Station		**Petrolina/PE**		**Mandacarú/BA**		**Bebedouro/PE**		**Barra/BA**		**Remanso/BA**	
Month		**April**	**May**	**April**	**May**	**April**	**May**	**April**	**May**	**April**	**May**
$T_{2m,mean}[^{\circ}\mathrm{C}]$	RMSE	1.56	1.58	1.65	1.57	2.81	3.09	-	-	-	-
	Bias	−0.27	−1.15	−0.54	1.3	−2.27	−2.08	-	-	-	-
$T_{2m,min}[^{\circ}\mathrm{C}]$	RMSE	1.05	1.45	2.73	2.8	4.29	4.41	4.7	5.17	1.28	1.49
	Bias	−0.5	0.56	−2.42	−2.41	−4.03	−4.05	−4.19	−5.01	−0.93	−1.12
$T_{2m,max}[^{\circ}\mathrm{C}]$	RMSE	2.66	1.89	2.79	1.65	3.08	2.08	2.09	1.73	4.8	3.61
	Bias	−0.02	−1.3	0.36	−0.97	−0.51	−1.56	−0.57	−1.29	−4.4	−1.17
$V_{3m}[\mathrm{ms}^{-1}]$	RMSE	-	-	1.98	1.44	2.11	2.36	0.81	0.77	2.67	3.05
	Bias	-	-	1.57	1.11	−1.72	−2.25	−0.08	−0.02	−2.27	−2.81

Table 8.1.: Root mean squared error (RMSE) and bias of simulated daily mean, minimum and maximum $2\mathrm{m}$ air temperatures and $3\mathrm{m}$ wind speeds in comparison with observed data for the period of 1 April- 31 May of the years 1998 and 2002

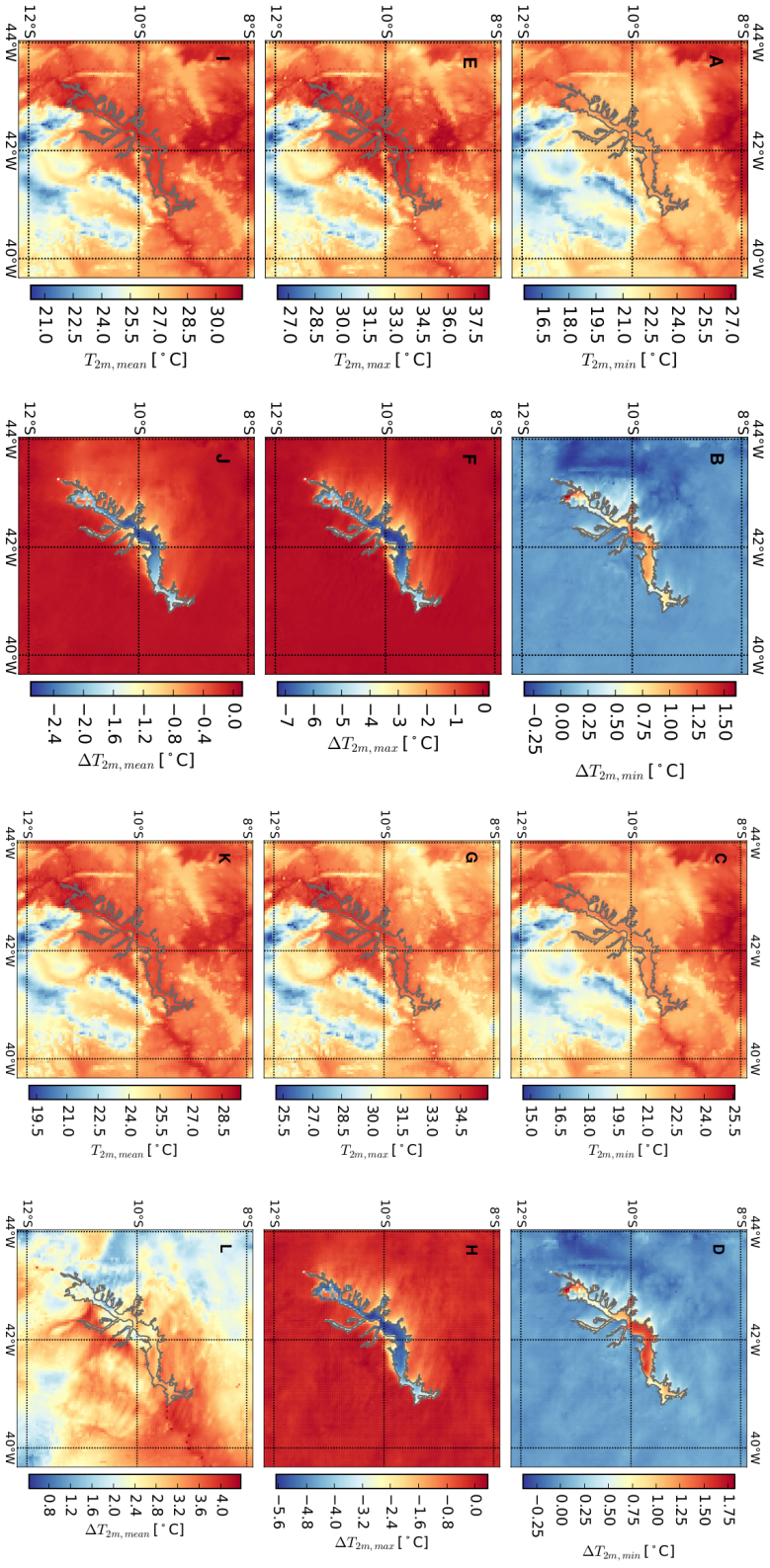

Figure 8.4.: Simulated air temperature at 2m above the ground:(A,B,C,D) daily minimum, (E,F,G,H) daily maximum and (I,J,K,L) daily mean values for the periods (A,B,E,F,I,J) 1 April- 31 May 1998 and (C,D,G,H,K,L) 1 April- 31 May 2002, respectively. (A,C,E,G,I,K) results for simulations without lake; (B,D,F,H,J,L) difference between the results including the lake with respect to the control runs without the lake. The lake's position is indicated by gray line.

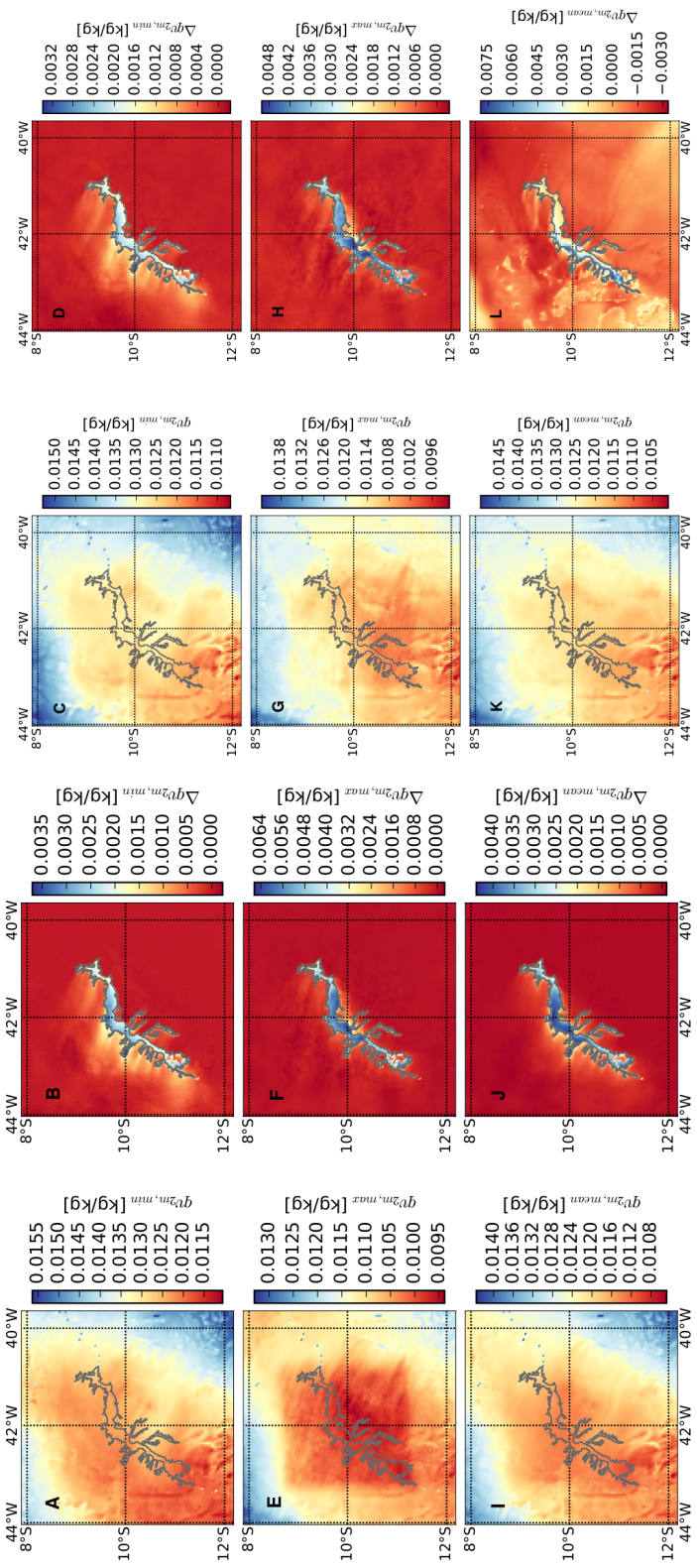

Figure 8.5.: Same as in Fig.8.4, but for the specific humidity at 2 m above the ground.

Analogously to Fig.8.4, Fig.8.5 shows the results for the daily minimum, maximum and mean specific humidity at 2 m above the ground ($qv_{2m,min}$, $qv_{2m,max}$, $qv_{2m,mean}$). As expected, the specific humidity over the lake is increased in comparison with the surrounding arid area during the whole day. This is especially pronounced during nighttime. With cooler air over the lake surface, humidity is advected in northeastern direction during daytime (Fig.8.5A,B), while the moister air is more confined to the lake area during nighttime (Fig.8.5E,F). The reasons for this are lower wind speeds and less mixing during nighttime, when the planetary boundary layer reaches its minimum height.

Figure 8.6 and 8.7 show the simulation results for the latent and sensible heat fluxes (lE and H), respectively. Here, the fluxes are positive when directed away from the lake and land surface and negative when directed towards the surface. During the day (Fig.8.5E,F) and nighttime (Fig.8.5A,B), Lake Sobradinho's simulated lE are about 250 $W.m^{-2}$ and 200 $W.m^{-2}$, respectively, and larger than the lE of the arid surrounding. Since the lake has a large heat capacity and natural moisture availability, most of the absorbed solar radiation is released as latent heat flux during the day. On the other hand, the surrounding natural land surface heats up more quickly and subsequently sensible heat flux leads to higher air temperature over the arid area than over the lake. In Fig.8.5I,J, it can be seen that the average amount of latent heat flux for the whole period of simulation is 250 $W.m^{-2}$ over the lake, which is much larger than over the surrounding area with 50 $W.m^{-2}$.

Regarding the simulated sensible heat fluxes (Fig 8.7), I recall that during the day the lake produces mostly latent heat flux, whereas the arid area without a lake would produce mostly sensible flux (Fig.8.7E,F). As a result, if there were no lake, the amount of sensible heat flux would increase in comparison with the case of the lake being present. It is noteworthy that, in the latter case, the arid area around the lake still produces more sensible heat flux than the lake area. In turn, during the night (Fig.8.7A,B), the lake produces a stronger sensible heat flux than the arid area without the lake. The arid land surface cools down more rapidly than the lake and, hence, the sensible heat flux above the lake increases. In Fig.8.7I,J, the average sensible heat flux for the whole period of simulation is 50 $W.m^{-2}$ over the lake, which is smaller than in the surrounding area (100 $W.m^{-2}$).

Average conditions: April/May 2002: I now turn to the case of average conditions as exemplified by our simulations for the year 2002. Regarding the daily minimum, maximum and mean air temperature, the spatial patterns displayed in Fig.8.4 are qualitatively similar to those in 1998. Especially during daytime (Fig.8.4C,D), the situation closely resembles that observed for the year 1998, whereas during the night (Fig.8.4G,H), the general impact of the lake (expressed in the differences between both simulations with and without the reservoir) are smaller than in 1998. Under the average conditions present in 2002, during the night the areas near the lake also release more latent heat than during the more extreme conditions of 1998. As a result, the differences between the lake and its surrounding area are less obvious

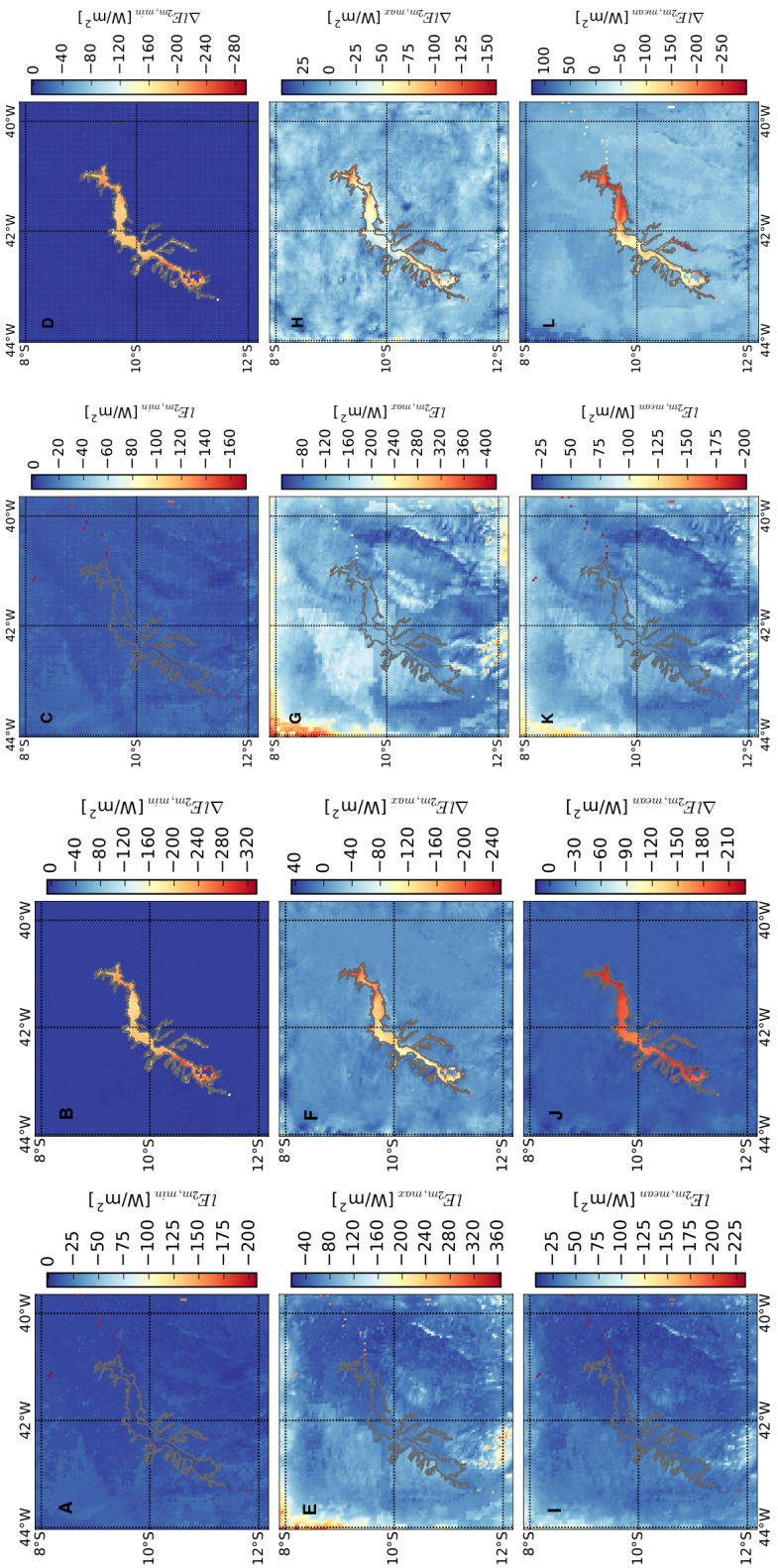

Figure 8.6.: Same as in Fig.8.4, but for the latent heat flux at 2 m above the ground.

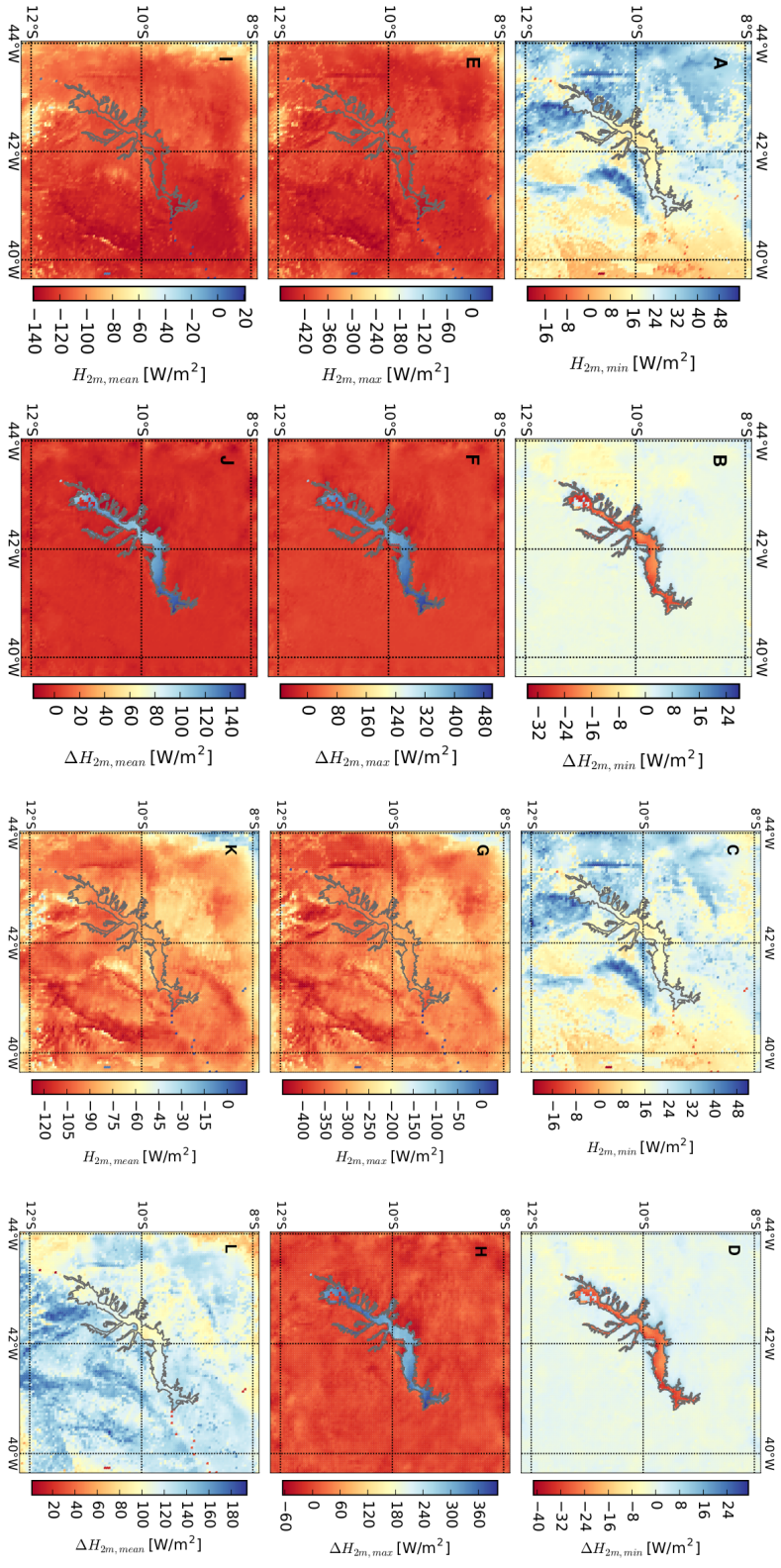

Figure 8.7.: Same as in Fig.8.4, but for the sensible heat flux at 2 m above the ground.

than during 1998. Because of the generally milder climate in 2002, the average effect of the lake on the air temperatures taken over the whole simulation period is not as pronounced as in the year 1998. The lake cools the air by just about 1 deg C in comparison to the case without the lake.

Comparing the daily minimum, maximum and mean values of the specific humidity at 2 m above the land surface with the results for 1998 (Fig.8.5), I observe little differences between both years. Note again that the area around the lake is semi-arid, so that the amount of humidity in this region is small. The only significant difference between both years can be seen in Fig.8.4I–L. In 1998, the region experienced an extremely hot season. Hence, the average difference in humidity between the two cases with and without lake was much larger than in the year 2002. In the latter, the surrounding areas were not as arid as in 1998.

Regarding the latent heat and sensible heat fluxes, respectively (Fig.8.6 and Fig.8.7), I identify strong differences between the situations in 1998 and 2002. As mentioned above, during 2002, there was more humidity in the surroundings of the lake, which could elevate the soil moisture level near the lake in comparison with the values in 1998. Because of the same characteristic behavior of lake and soil water, during the day, I also observe latent heat fluxes over the lake's surroundings, so that the overall amount of latent heat flux in the year 2002 was larger than in 1998. On the other hand, the sensible heat flux also increased for the same reason as for the latent heat flux. Consequently, in the bottom panels of Fig.8.6 and Fig.8.7, the lake's effect on the average amount of latent and sensible heat fluxes is less obvious than during 1998. As expected, orography is the most crucial factor controlling the horizontal and vertical distributions of the flows of energy and water, as can be seen from the predominant SE/NW direction of the flows.

8.1.2.3. Lake Effects on Atmospheric Circulation

Figure 8.8 shows the characteristic wind fields for the simulation without the lake, as well as the associated differences if the lake is present, at 3 : 00 am and 3 : 00 pm local time for both simulation periods.

In 1998, the wind velocities have been mostly unaffected by the presence of Lake Sobradinho. One key aspect related to this observation is the presence of a significant orographic effect that controls wind speed and direction in the study area. Specifically, anabatic winds in the region can affect the local circulation around the lake. There is also a pressure gradient as a result of air temperature differences between the lake and its surroundings, which causes a local thermal circulation (lake breeze). The difference plots in Fig.8.8B,F highlight this effect. In summary, there are a multitude of factors, including the surface temperature of the lake and its surrounding land surface, vegetation cover and orography, all of which do potentially affect the magnitude and direction of the lake breeze.

From a process-based perspective, in an area with low humidity, the surface evaporation would be high initially. Therefore, most of the energy absorbed by the surface would be emitted as latent heat. However, as the surface becomes progressively dryer

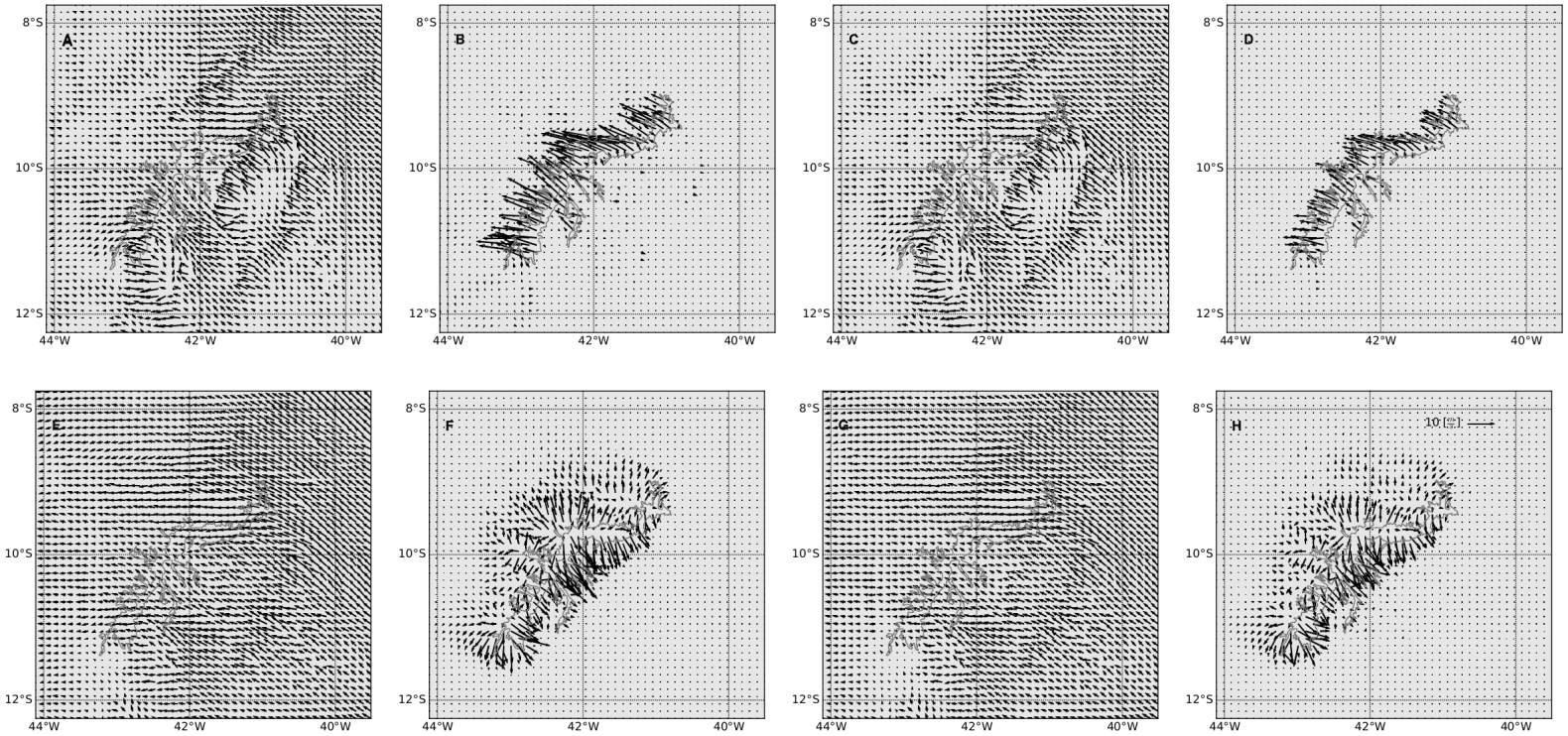

Figure 8.8.: Characteristic wind velocities at $3\mathrm{m}$ above the ground at (A,B,C,D) $3:00$ am and (E,F,G,H) $3:00$ pm for (A,C,E,G) the situation without the lake and (B,D,F,H) differences for the simulations with the lake in comparison with the control run without the lake. The results correspond to the periods (A,B,E,F) 1 April–31 May 1998 and (C,D,G,H) 1 April–31 May 2002, respectively.

during the day, the evaporation rate decreases and the air temperature increases, so most of the energy will be emitted as sensible heat flux. The intensity of thermally induced circulation can be affected by the amount and intensity of surface energy fluxes [38].

During daytime, the lake produces large amounts of latent heat flux. Therefore, the air temperature above the lake is lower than in its surrounding areas. As a consequence, the air pressure above the lake is higher than above the nearby land surface, which causes a pressure gradient and creates a lake breeze towards the area close to the lake.

The situation is vice versa during the night. Here, the air temperature over the lake is higher than in the area surrounding the lake, and most of the available energy is redistributed by sensible heat flux. The pressure above the lake is reduced, which causes again a pressure gradient and a resulting breeze, but this time towards the lake.

As could be expected, the situation for the year 2002 is qualitatively similar. However, as one can see in Fig.8.8C,D,G,H, the lake breeze during the day is weaker than for 1998. To understand this difference, recall that in 1998, the air temperature has been higher than in 2002, associated with the much drier conditions. In such an extreme situation, the presence of the lake has stronger effects than in years with average meteorological conditions.

8.1.3. Conclusions

In this study, I have investigated the effects of the artificial freshwater reservoir Lake Sobradinho on the regional climate of its surrounding areas. For this purpose, I have used the regional climate model COSMO-CLM (CCLM). My analyses have focused on air temperature, humidity, energy fluxes and wind. I have studied two representative periods in different years, one (1998) representing an extreme situation while the other one (2002) corresponds to the average climatic conditions of the region. By comparing the model simulations with station data, I have demonstrated that CCLM is able to reproduce the overall situation qualitatively, but exhibits substantial biases in air temperature and wind velocity.

Based on the simulations for the two considered years, I have demonstrated the emergence of a lake breeze during daytime. As a consequence, the air temperature in the lake's surrounding decreases whereas humidity increases. The latent heat flux increases as well, while the sensible heat flux decreases. The situation is reversed during the night. Here, the presence of the lake decreases the latent heat flux and increases the sensible heat flux, so the humidity over the lake increases. Because of lower wind speeds, reduced mixing and the lower planetary boundary layer height during nighttime, the humidity remains confined near the lake and advection to the surrounding area is reduced in comparison to daytime. The land areas near the lake cool faster than the lake itself, so during the night cooler winds blow towards the lake. The comparison between the more extreme year and the average climate demonstrates that the regional climatic effect of Lake Sobradinho is more pronounced

during extreme years. More specifically, the presence of the lake has stronger effects on near-surface meteorological variables in a drier situation rather than under the normal mean climatology.

The present study underlines the existence of non-negligible effects of artificial reservoirs on local climate. Future studies should address in more detail the longer-term climate situations with and without the lake and additionally investigate the effect of land use change and greenhouse gas emissions on the regional climate of Northeastern Brazil.

Chapter 9.

Conclusion

In this thesis, I have investigated the interaction of the atmosphere with water bodies via two different approaches.

In the first part, I have utilized a new type of application of complex networks in climate. Specifically, I have used coupled climate networks reflecting the strongest statistical interactions between SST and PCP at all available grid points on the Earth. First part, I assessed the effect of different ENSO phases on the interaction between the SST and PCP and whether these interactions are positive or negative. I found out that mainly surface temperature of equatorial oceans interact with the PCP during different phases of ENSO. For instance, during neutral ENSO phases, mostly the western equatorial Ocean, the tropical Indian Ocean, and the Atlantic Ocean influence PCP globally. During La Nina, similar patterns as for neutral ENSO are dominant but stronger. The main reason for this is the Walker circulation that becomes stronger during the La Nina phase, and this causes stronger patterns. However, during El Nino, mostly the eastern equatorial Pacific acts as the main source of variations in PCP. Although by applying coupled climate networks, I did not investigate the nature of these interactions in details, this approach still provides a broader picture of how such interactions might change due to the effect of different ENSO phases. In the following part, I combined a time scale decomposition technique (wavelet analysis) with coupled climate networks to track interactions between SST and PCP across different time scales. By having separate time scales, the appearance and disappearance of different patterns that are related to seasonal or inter-annual variabilities of large-scale climate phenomena has been traced. Although looking at the original scale of the data highlights the main interaction patterns, there is a possibility for overlooking other relevant variability patterns that act at different time scales and might not be as strong as the dominant modes like ENSO. Most notably, the highest mutual correlations between SST and PCP at annual scale (8 to 16 months) concentrate mostly over the Pacific Ocean, while the corresponding spatial patterns progressively disappear when moving towards longer time-scales.

In the second part, I studied the mechanisms of interaction between atmosphere and water surface in a specific domain of interest, Northeastern Brazil. For this purpose, I used the sophisticated regional climate model CCLM. In this approach, relevant physical processes within the atmosphere and the Earth surface are considered via parametrizations. This results in a significant complexity of the model and therefore an initial guess for the model parameters requires foresight into the

physical processes and also how those parametrizations work. Specifically, I investigated the effect of the presence of the Sobradino Lake on its regional climate by applying FLake, a parametrization scheme that is used for shallow to mid-size lakes. By utilizing FLake in the initial setup of CCLM, it captured the main effects of lake Sobradino on its surroundings. My results illustrated that the absence of lake Sobradino leads to higher air temperature and therefore a higher amount the sensible heat while lower amount of latent heat fluxes and humidity.

By applying these two approaches I gained new insight into the different physical processes within the climate system and how they interact with each other. Using coupled climate networks is useful for obtaining a general picture of these interactions without considering the complex physical processes. On the other hand, using regional or global climate models requires a vast knowledge of physical processes which might be costly in the terms of computational power.

Bibliography

Adler, R. F., Huffman, G. J., Chang, A., Ferraro, R., Xie, P.-P., Janowiak, J., Rudolf, B., Schneider, U., Curtis, S., Bolvin, D., Gruber, A., Susskind, J., Arkin, P., and Nelkin, E. (2003). "The Version-2 Global Precipitation Climatology Project (GPCP) Monthly Precipitation Analysis (1979–Present)". In: *Journal of Hydrometeorology* 4.6, pp. 1147–1167. DOI: 10.1175/1525-7541(2003)004<1147:TVGPCP>2.0.CO;2 (cit. on p. 42).

Agustí, P., Traver, V. J., Marin-Jimenez, M. J., and Pla, F. (2011). "Exploring Alternative Spatial and Temporal Dense Representations for Action Recognition". In: *Computer Analysis of Images and Patterns*. Ed. by P. Real, D. Diaz-Pernil, H. Molina-Abril, A. Berciano, and W. Kropatsch. Berlin, Heidelberg: Springer Berlin Heidelberg, pp. 364–371. ISBN: 978-3-642-23678-5 (cit. on p. 9).

Albert, R. and Barabási, A.-L. (2002a). "Statistical mechanics of complex networks". In: *Reviews of Modern Physics* 74.1, pp. 47–97. DOI: 10.1103/RevModPhys.74.47 (cit. on pp. 9, 14, 16, 44).

– (2002b). "Statistical mechanics of complex networks". In: *Rev. Mod. Phys.* 74 (1), pp. 47–97. DOI: 10.1103/RevModPhys.74.47 (cit. on p. 9).

Alexander, M. A., Lau, N.-C., and Scott, J. D. (2013). "Broadening the Atmospheric Bridge Paradigm: ENSO Teleconnections to the Tropical West Pacific-Indian Oceans Over the Seasonal Cycle and to the North Pacific in Summer". In: *Earth's Climate*. American Geophysical Union (AGU), pp. 85–103. ISBN: 9781118665947. DOI: 10.1029/147GM05 (cit. on p. 38).

Alexander, M. A., Bladé, I., Newman, M., Lanzante, J. R., Lau, N.-C., and Scott, J. D. (2002). "The atmospheric bridge: The influence of ENSO teleconnections on air–sea interaction over the global oceans". In: *Journal of Climate* 15.16, pp. 2205–2231 (cit. on pp. 11, 30, 37).

Araújo (2011). "A região Semiárida do Nordeste do Brasil: Questões Ambientais e Possibilidades de uso Sustentável dos Recursos". In: *Rios Eletrôn. Rev. Cient. FASETE*, pp. 89–98 (cit. on p. 90).

Arenas, A., Díaz-Guilera, A., and Pérez-Vicente, C. J. (Mar. 22, 2006). "Synchronization Reveals Topological Scales in Complex Networks". In: *Physical Review Letters* 96.11, p. 114102. DOI: 10.1103/PhysRevLett.96.114102 (cit. on p. 45).

Arizmendi, F., Martí, A. C., and Barreiro, M. (2014). "Evolution of atmospheric connectivity in the 20th century". In: *Nonlin. Processes Geophys.* 21.4, pp. 825–839. ISSN: 1607-7946. DOI: 10.5194/npg-21-825-2014 (cit. on pp. 10, 59).

Arnell, N. (Dec. 1996). *Global Warming, River Flows and Water Resources*. en. Google-Books-ID: XcIPAQAAIAAJ. Wiley. ISBN: 978-0-471-96599-2 (cit. on p. 93).

Ashok, K., Behera, S. K., Rao, S. A., Weng, H., and Yamagata, T. (2007). "El Niño Modoki and its possible teleconnection". In: *Journal of Geophysical Research: Oceans* 112.C11. DOI: 10.1029/2006JC003798 (cit. on p. 19).

Assis, O. de, Souza, W., and Sobral, M. (2015). "Análise climática da precipitação no submédio da bacia do Rio São Francisco com base no índice de anomalia de chuva". In: pp. 115–127 (cit. on p. 91).

Baldauf, M., Seifert, A., Förstner, J., Majewski, D., Raschendorfer, M., and Reinhardt, T. (2011). "Operational Convective-Scale Numerical Weather Prediction with the COSMO Model: Description and Sensitivities". In: *Monthly Weather Review* 139.12, pp. 3887–3905. DOI: 10.1175/MWR-D-10-05013.1 (cit. on p. 74).

Barreiro, M., Marti, A. C., and Masoller, C. (2011). "Inferring long memory processes in the climate network via ordinal pattern analysis". In: *Chaos: An Interdisciplinary Journal of Nonlinear Science* 21.1, p. 013101. ISSN: 1054-1500. DOI: 10.1063/1.3545273 (cit. on p. 10).

Bates, G. T., Giorgi, F., and Hostetler, S. W. (1993). "Toward the Simulation of the Effects of the Great Lakes on Regional Climate". In: *Monthly Weather Review* 121.5, pp. 1373–1387. DOI: 10.1175/1520-0493(1993)121<1373:TTSOTE>2.0.CO;2 (cit. on p. 73).

Bechtold, P., Köhler, M., Jung, T., Doblas-Reyes, F., Leutbecher, M., Rodwell, M. J., Vitart, F., and Balsamo, G. (2008). "Advances in simulating atmospheric variability with the ECMWF model: From synoptic to decadal time-scales". In: *Quarterly Journal of the Royal Meteorological Society* 134.634, pp. 1337–1351. DOI: 10.1002/qj.289 (cit. on p. 87).

Behera, S. K. and Yamagata, T. (2003). "Influence of the Indian Ocean Dipole on the Southern Oscillation". In: *Journal of the Meteorological Society of Japan. Ser. II* 81.1, pp. 169–177. DOI: 10.2151/jmsj.81.169 (cit. on p. 38).

Bischoff-Gauß, I., Kalthoff, N., and Fiebig-Wittmaack, M. (2006). "The influence of a storage lake in the Arid Elqui Valley in Chile on local climate". In: *Theoretical and Applied Climatology* 85.3, pp. 227–241. ISSN: 1434-4483. DOI: 10.1007/s00704-005-0190-8 (cit. on p. 73).

Bjerknes (1964). "Atlantic air-sea interaction". In: *Advances in geophysics*. Vol. 10. Elsevier, pp. 1–82 (cit. on pp. 29, 41).

– (2009). "The problem of weather prediction, considered from the viewpoints of mechanics and physics". In: *Meteorologische Zeitschrift* 18.6, pp. 663–667. DOI: 10.1127/0941-2948/2009/416 (cit. on pp. 77, 78).

Boccaletti, S., Bianconi, G., Criado, R., Genio, C. del, Gómez-Gardeñes, J., Romance, M., Sendiña-Nadal, I., Wang, Z., and Zanin, M. (2014). "The structure and dynamics of multilayer networks". In: *Physics Reports* 544.1. The structure and dynamics of multilayer networks, pp. 1–122. ISSN: 0370-1573. DOI: https://doi.org/10.1016/j.physrep.2014.07.001 (cit. on p. 16).

Boccaletti, S., Latora, V., Moreno, Y., Chavez, M., and Hwang, D.-U. (2006). "Complex networks: Structure and dynamics". In: *Physics Reports* 424.4, pp. 175–308. ISSN: 0370-1573. DOI: https://doi.org/10.1016/j.physrep.2005.10.009 (cit. on pp. 9, 13).

Boers, N., Bookhagen, B., Barbosa, H. M. J., Marwan, N., Kurths, J., and Marengo, J. A. (2014a). "Prediction of extreme floods in the eastern Central Andes based on a complex networks approach". In: *Nature Communications* 5, p. 5199. ISSN: 2041-1723. DOI: 10.1038/ncomms6199 (cit. on pp. 10, 20).

Boers, N., Bookhagen, B., Marwan, N., Kurths, J., and Marengo, J. (2013). "Complex networks identify spatial patterns of extreme rainfall events of the South American Monsoon System". In: *Geophysical Research Letters* 40.16, pp. 4386–4392. DOI: 10.1002/grl.50681 (cit. on pp. 10, 20).

Boers, N., Donner, R. V., Bookhagen, B., and Kurths, J. (2015). "Complex network analysis helps to identify impacts of the El Niño Southern Oscillation on moisture divergence in South America". In: *Climate Dynamics* 45.3, pp. 619–632. ISSN: 1432-0894. DOI: 10.1007/s00382-014-2265-7 (cit. on p. 10).

Boers, N., Rheinwalt, A., Bookhagen, B., Barbosa, H. M. J., Marwan, N., Marengo, J., and Kurths, J. (2014b). "The South American rainfall dipole: A complex network analysis of extreme events". In: *Geophysical Research Letters* 41.20, pp. 7397–7405. DOI: 10.1002/2014GL061829 (cit. on pp. 10, 20).

Böhm, U., Gerstengarbe, F.-W., Hauffe, D., Kücken, M., Österle, H., and Werner, P. C. (2003). "Dynamic Regional Climate Modeling and Sensitivity Experiments for the Northeast of Brazil". In: *Global Change and Regional Impacts: Water Availability and Vulnerability of Ecosystems and Society in the Semiarid Northeast of Brazil*. Ed. by T. Gaiser, M. Krol, H. Frischkorn, and J. C. de Araújo. Berlin, Heidelberg: Springer Berlin Heidelberg, pp. 153–170. ISBN: 978-3-642-55659-3. DOI: 10.1007/978-3-642-55659-3_12 (cit. on p. 74).

Bonan, G. B. (1995). "Sensitivity of a GCM Simulation to Inclusion of Inland Water Surfaces". In: *Journal of Climate* 8.11, pp. 2691–2704. DOI: 10.1175/1520-0442(1995)008<2691:SOAGST>2.0.CO;2 (cit. on p. 73).

Bradshaw and McIntosh (1994). "Detecting climate-induced patterns using wavelet analysis". In: *Environmental Pollution* 83.1, pp. 135–142. ISSN: 0269-7491. DOI: https://doi.org/10.1016/0269-7491(94)90031-0 (cit. on p. 55).

Broomhead, D. and King, G. P. (1986). "Extracting qualitative dynamics from experimental data". In: *Physica D: Nonlinear Phenomena* 20.2, pp. 217–236. ISSN: 0167-2789. DOI: https://doi.org/10.1016/0167-2789(86)90031-X (cit. on p. 9).

Bullmore, E. and Sporns, O. (2009a). "Complex brain networks: graph theoretical analysis of structural and functional systems". en. In: *Nature Reviews Neuroscience* 10.3, pp. 186–198. ISSN: 1471-0048. DOI: 10.1038/nrn2575 (cit. on p. 9).

– (2009b). "Complex brain networks: graph theoretical analysis of structural and functional systems". In: *Nature Reviews Neuroscience* 10. Review Article, 186 EP - (cit. on p. 13).

Carter, T., Parry, M., Harasawa, H., and Nishioka, S. (1994). *IPCC technical guidelines for assessing climate change impacts and adaptions. IPPC special report to Working Group II of IPCC.* London: University College London and Tsukaba, Japan: Centre for Global Environmental Research. (cit. on p. 80).

Carton, J. A., Cao, X., Giese, B. S., and Da Silva, A. M. (1996). "Decadal and Interannual SST Variability in the Tropical Atlantic Ocean". In: *Journal of Physical*

Oceanography 26.7, pp. 1165–1175. DOI: 10.1175/1520-0485(1996)026<1165:DAISVI>2.0.CO;2 (cit. on p. 35).

Chan, S. H. Y., Donner, R. V., and Lämmer, S. (2011). "Urban road networks — spatial networks with universal geometric features?" In: *The European Physical Journal B* 84.4, pp. 563–577. ISSN: 1434-6036. DOI: 10.1140/epjb/e2011-10889-3 (cit. on p. 13).

Chan, Behera, and Yamagata (2008). "Indian Ocean Dipole influence on South American rainfall". In: *Geophysical Research Letters* 35.14, L14S12. DOI: 10.1029/2008GL034204. eprint: https://agupubs.onlinelibrary.wiley.com/doi/pdf/10.1029/2008GL034204 (cit. on p. 63).

Chang, P., Ji, L., and Li, H. (1997). "A decadal climate variation in the tropical Atlantic Ocean from thermodynamic air-sea interactions". In: *Nature* 385.6616, pp. 516–518. ISSN: 1476-4687. DOI: 10.1038/385516a0 (cit. on p. 35).

Chen, Y.-H., Wang, B.-H., Zhao, L.-C., Zhou, C., and Zhou, T. (2010). "Optimal transport on supply-demand networks". In: *Phys. Rev. E* 81 (6), p. 066105. DOI: 10.1103/PhysRevE.81.066105 (cit. on p. 9).

Chiang and Vimont (2004). "Analogous Pacific and Atlantic Meridional Modes of Tropical Atmosphere–Ocean Variability". In: *Journal of Climate* 17.21, pp. 4143–4158. DOI: 10.1175/JCLI4953.1 (cit. on p. 62).

Coiffier, J. (2011). "Half a century of numerical weather prediction". In: *Fundamentals of Numerical Weather Prediction*. Cambridge University Press, pp. 1–14. DOI: 10.1017/CBO9780511734458.005 (cit. on p. 77).

Collins, S. N., James, R. S., Ray, P., Chen, K., Lassman, A., and Brownlee, J. (2013). "Grids in Numerical Weather and Climate Models". In: *Climate Change and Regional/Local Responses*. Ed. by Y. Zhang and P. Ray. Rijeka: IntechOpen. Chap. 4. DOI: 10.5772/55922 (cit. on p. 81).

Correia, M. D. F. and Dias, M. A. F. D. S. (2003). "Variação do Nível do Reservatório de Sobradinho e seu Impacto Sobre o Clima da Região". pt-br. In: *RBRH - Revista Brasileira de Recursos Hídricos* 8.1, pp. 157–168. ISSN: 2318-0331 (cit. on pp. 91, 94).

Correia, Alvalá, R. C. S., and Manzi, A. O. (2008). "Modeling the impacts of land cover change in Amazonia: a regional climate model (RCM) simulation study". In: *Theoretical and Applied Climatology* 93.3, pp. 225–244. ISSN: 1434-4483. DOI: 10.1007/s00704-007-0335-z (cit. on p. 75).

Correia, Silva Dias, M. A. F. da, and Silva Aragão, M. R. da (2006a). "Soil occupation and atmospheric variations over Sobradinho Lake area. Part one: an observational analysis". In: *Meteorology and Atmospheric Physics* 94.1, pp. 103–113. ISSN: 1436-5065. DOI: 10.1007/s00703-005-0173-4 (cit. on p. 75).

– (2006b). "Soil occupation and atmospheric variations over Sobradinho Lake area. Part two: a regional modeling study". In: *Meteorology and Atmospheric Physics* 94.1, pp. 115–128. ISSN: 1436-5065. DOI: 10.1007/s00703-005-0174-3 (cit. on p. 75).

Costa, Rodrigues, F. A., Travieso, G., and Boas, P. R. V. (2007). "Characterization of complex networks: A survey of measurements". In: *Advances in Physics* 56.1, pp. 167–242. DOI: 10.1080/00018730601170527 (cit. on p. 13).

Croft, D. P., James, R., and Krause, J. (2008). *Exploring Animal Social Networks*. Princeton University Press. ISBN: 9780691127521 (cit. on p. 9).

Curtis, S. and Hastenrath, S. (1995). "Forcing of anomalous sea surface temperature evolution in the tropical Atlantic during Pacific warm events". In: *Journal of Geophysical Research: Oceans* 100.C8, pp. 15835–15847. DOI: 10.1029/95JC01502 (cit. on p. 35).

Danila, B., Yu, Y., Marsh, J. A., and Bassler, K. E. (2006). "Optimal transport on complex networks". In: *Phys. Rev. E* 74 (4), p. 046106. DOI: 10.1103/PhysRevE.74.046106 (cit. on p. 9).

Davies, H. C. (1976). "A lateral boundary formulation for multi-level prediction models". In: *Quarterly Journal of the Royal Meteorological Society* 102.432, pp. 405–418. DOI: 10.1002/qj.49710243210 (cit. on p. 85).

Davin, E. L. and Seneviratne, S. I. (2012). "Role of land surface processes and diffuse/direct radiation partitioning in simulating the European climate". In: *Biogeosciences* 9.5, pp. 1695–1707. DOI: 10.5194/bg-9-1695-2012 (cit. on p. 74).

Dee, D. P., Uppala, S. M., Simmons, A. J., Berrisford, P., Poli, P., Kobayashi, S., Andrae, U., Balmaseda, M. A., Balsamo, G., Bauer, P., Bechtold, P., Beljaars, A. C. M., Berg, L. van de, Bidlot, J., Bormann, N., Delsol, C., Dragani, R., Fuentes, M., Geer, A. J., Haimberger, L., Healy, S. B., Hersbach, H., Hólm, E. V., Isaksen, L., Kållberg, P., Köhler, M., Matricardi, M., McNally, A. P., Monge-Sanz, B. M., Morcrette, J.-J., Park, B.-K., Peubey, C., Rosnay, P. de, Tavolato, C., Thépaut, J.-N., and Vitart, F. (2011). "The ERA-Interim reanalysis: configuration and performance of the data assimilation system". In: *Quarterly Journal of the Royal Meteorological Society* 137.656, pp. 553–597. DOI: 10.1002/qj.828 (cit. on p. 89).

Delworth, Broccoli, A. J., Rosati, A., Stouffer, R. J., Balaji, V., Beesley, J. A., Cooke, W. F., Dixon, K. W., Dunne, J., Dunne, K. A., Durachta, J. W., Findell, K. L., Ginoux, P., Gnanadesikan, A., Gordon, C. T., Griffies, S. M., Gudgel, R., Harrison, M. J., Held, I. M., Hemler, R. S., Horowitz, L. W., Klein, S. A., Knutson, T. R., Kushner, P. J., Langenhorst, A. R., Lee, H.-C., Lin, S.-J., Lu, J., Malyshev, S. L., Milly, P. C. D., Ramaswamy, V., Russell, J., Schwarzkopf, M. D., Shevliakova, E., Sirutis, J. J., Spelman, M. J., Stern, W. F., Winton, M., Wittenberg, A. T., Wyman, B., Zeng, F., and Zhang, R. (Mar. 1, 2006). "GFDL's CM2 Global Coupled Climate Models. Part I: Formulation and Simulation Characteristics". In: *Journal of Climate* 19.5, pp. 643–674. ISSN: 0894-8755. DOI: 10.1175/JCLI3629.1 (cit. on p. 45).

Delworth, Manabe, and Stouffer (1993). "Interdecadal Variations of the Thermohaline Circulation in a Coupled Ocean-Atmosphere Model". In: *Journal of Climate* 6.11, pp. 1993–2011. DOI: 10.1175/1520-0442(1993)006<1993:IVOTTC>2.0.CO;2 (cit. on p. 37).

Deza, J. I., Barreiro, M., and Masoller, C. (2015). "Assessing the direction of climate interactions by means of complex networks and information theoretic tools". In:

Chaos: An Interdisciplinary Journal of Nonlinear Science 25.3, p. 033105. ISSN: 1054-1500. DOI: 10.1063/1.4914101 (cit. on p. 10).

Dickinson, Errico, R. M., Giorgi, F., and Bates, G. T. (1989). "A regional climate model for the western United States". In: *Climatic Change* 15.3, pp. 383–422. ISSN: 1573-1480. DOI: 10.1007/BF00240465 (cit. on pp. 81, 85).

Dickinson, Henderson-Sellers, A., Kennedy, J., and Wilson, F. (1986). "Biosphere-atmosphere Transfer Scheme (BATS) for the NCAR Community Climate Model". en. In: DOI: 10.5065/D6668B58 (cit. on p. 87).

Dijkstra, H. A., Hernández-García, E., Masoller, C., and Barreiro, M. (2019). *Networks in Climate*. Cambridge: Cambridge University Press (cit. on p. 42).

Dobler, A. and Ahrens, B. (2010). "Analysis of the Indian summer monsoon system in the regional climate model COSMO-CLM". In: *Journal of Geophysical Research: Atmospheres* 115.D16. DOI: 10.1029/2009JD013497 (cit. on p. 74).

Doms, G. and Schättler, U. (2002). "A description of the nonhydrostatic regional model LM, Part I: Dynamics and numerics". In: 2, pp. 225–235 (cit. on pp. 86, 87).

Donges, J. F., Schultz, H. C. H., Marwan, N., Zou, Y., and Kurths, J. (2011a). "Investigating the topology of interacting networks". In: *The European Physical Journal B* 84.4, pp. 635–651. ISSN: 1434-6028, 1434-6036. DOI: 10.1140/epjb/e2011-10795-8 (cit. on pp. 10, 16, 17, 19, 21, 42, 45, 59).

– (2011b). "Investigating the topology of interacting networks". In: *The European Physical Journal B* 84.4, pp. 635–651. ISSN: 1434-6036. DOI: 10.1140/epjb/e2011-10795-8 (cit. on p. 11).

Donges, J. F., Zou, Y., Marwan, N., and Kurths, J. (2009a). "Complex networks in climate dynamics". In: *The European Physical Journal Special Topics* 174.1, pp. 157–179. ISSN: 1951-6355, 1951-6401. DOI: 10.1140/epjst/e2009-01098-2 (cit. on pp. 9, 10, 17, 19).

– (2009b). "The backbone of the climate network". In: *EPL (Europhysics Letters)* 87.4, p. 48007. ISSN: 0295-5075. DOI: 10.1209/0295-5075/87/48007 (cit. on pp. 10, 20).

Donner, R. V., Wiedermann, M., and Donges, J. F. (2017). "Complex Network Techniques for Climatological Data Analysis". In: *Nonlinear Stoch. Clim. Dyn.* Ed. by C. Franzke and T. O'Kane. 1st ed. Cambridge: Cambridge University Press, pp. 159–183 (cit. on p. 42).

Donner, Schubert, W. H., and Somerville, R. (2011). *The development of atmospheric general circulation models : complexity, synthesis, and computation*. Cambridge ; New York (cit. on pp. 77, 88).

Donner, Wiedermann, M., and Donges, J. F. (2017). "Complex Network Techniques for Climatological Data Analysis". In: *Nonlinear and Stochastic Climate Dynamics*. Ed. by C. L. E. Franzke and T. J. O'Kane. Cambridge University Press, pp. 159–183. DOI: 10.1017/9781316339251.007 (cit. on p. 18).

Ebert-Uphoff, I. and Deng, Y. (2012). "Causal Discovery for Climate Research Using Graphical Models". In: *Journal of Climate* 25.17, pp. 5648–5665. DOI: 10.1175/JCLI-D-11-00387.1 (cit. on pp. 10, 20).

Eckmann, J.-P., Kamphorst, S. O., and Ruelle, D. (Nov. 1987). "Recurrence Plots of Dynamical Systems". In: *Europhysics Letters (EPL)* 4.9, pp. 973–977. DOI: 10.1209/0295-5075/4/9/004 (cit. on p. 9).

Ekhtiari, N., Grossman-Clarke, S., Koch, H., Meira de Souza, W., Donner, R. V., and Volkholz, J. (2017). "Effects of the Lake Sobradinho Reservoir (Northeastern Brazil) on the Regional Climate". In: *Climate* 5.3. ISSN: 2225-1154. DOI: 10.3390/cli5030050 (cit. on p. 89).

Enfield, D. B. and Mayer, D. A. (1997). "Tropical Atlantic sea surface temperature variability and its relation to El Niño-Southern Oscillation". In: *Journal of Geophysical Research: Oceans* 102.C1, pp. 929–945. DOI: 10.1029/96JC03296 (cit. on pp. 35, 38).

Farge, M. (1992). "WAVELET TRANSFORMS AND THEIR APPLICATIONS TO TURBULENCE". In: *Annual Review of Fluid Mechanics* 24.1, pp. 395–458. DOI: 10.1146/annurev.fl.24.010192.002143. eprint: https://doi.org/10.1146/annurev.fl.24.010192.002143 (cit. on p. 9).

Farmer, D. M. and Carmack, E. (1981). "Wind Mixing and Restratification in a Lake near the Temperature of Maximum Density". In: *Journal of Physical Oceanography* 11.11, pp. 1516–1533. DOI: 10.1175/1520-0485(1981)011<1516:WMARIA>2.0.CO;2 (cit. on p. 83).

Fedorov, A. V. (2008). *Ocean–atmosphere coupling* (cit. on pp. 11, 29, 41).

Feng and Dijkstra, H. (2013). "Are North Atlantic multidecadal SST anomalies westward propagating?" In: *Geophysical Research Letters* 41.2, pp. 541–546. DOI: 10.1002/2013GL058687 (cit. on p. 18).

Feng, Gong, Z., Wang, Q., and Feng, G. (2012). "Three-dimensional air–sea interactions investigated with bilayer networks". In: *Theoretical and Applied Climatology* 109.3, pp. 635–643. ISSN: 0177-798X, 1434-4483. DOI: 10.1007/s00704-012-0600-7 (cit. on pp. 10, 11, 17, 19, 21, 42, 45, 59).

Filyushkin, B. N. and Miropolsky, Y. Z. (1981). "Seasonal variability of the upper thermocline and self-similarity of temperature profiles." In: *Okeanologia* 21, pp. 416–424 (cit. on p. 84).

Fischer, T., Menz, C., Su, B., and Scholten, T. (2013). "Simulated and projected climate extremes in the Zhujiang River Basin, South China, using the regional climate model COSMO-CLM". In: *International Journal of Climatology* 33.14, pp. 2988–3001. DOI: 10.1002/joc.3643 (cit. on p. 74).

Fortunato, S. (2010). "Community detection in graphs". In: *Physics Reports* 486.3, pp. 75–174. ISSN: 0370-1573. DOI: https://doi.org/10.1016/j.physrep.2009.11.002 (cit. on p. 45).

Fortunato, S. and Hric, D. (2016). "Community detection in networks: A user guide". In: *Physics Reports* 659. Community detection in networks: A user guide, pp. 1–44. ISSN: 0370-1573. DOI: https://doi.org/10.1016/j.physrep.2016.09.002 (cit. on p. 45).

Fraedrich, K. (1986). "Estimating the Dimensions of Weather and Climate Attractors". In: *Journal of the Atmospheric Sciences* 43.5, pp. 419–432. DOI: 10.1175/1520-

0469(1986)043<0419:ETDOWA>2.0.CO;2. eprint: https://doi.org/10.1175/1520-0469(1986)043<0419:ETDOWA>2.0.CO;2 (cit. on p. 9).

García-Serrano, Losada, and Rodríguez-Fonseca (2011). "Extratropical Atmospheric Response to the Atlantic Niño Decaying Phase". In: *Journal of Climate* 24.6, pp. 1613–1625. DOI: 10.1175/2010JCLI3640.1. eprint: https://doi.org/10.1175/2010JCLI3640.1 (cit. on p. 64).

Ghil, M., Allen, M. R., Dettinger, M. D., Ide, K., Kondrashov, D., Mann, M. E., Robertson, A. W., Saunders, A., Tian, Y., Varadi, F., and Yiou, P. (2002). "Advanced spectral methods for climatic time series". In: *Reviews of Geophysics* 40.1. DOI: 10.1029/2000RG000092 (cit. on p. 9).

Giannini, Saravanan, and Chang (2004). "The preconditioning role of Tropical Atlantic Variability in the development of the ENSO teleconnection: implications for the prediction of Nordeste rainfall". In: *Climate Dynamics* 22.8, pp. 839–855. ISSN: 1432-0894. DOI: 10.1007/s00382-004-0420-2 (cit. on p. 64).

Giese, B. S. and Carton, J. A. (1999). "Interannual and Decadal Variability in the Tropical and Midlatitude Pacific Ocean". In: *Journal of Climate* 12.12, pp. 3402–3418. DOI: 10.1175/1520-0442(1999)012<3402:IADVIT>2.0.CO;2 (cit. on p. 38).

Gillett, Kell, and Jones (2006). "Regional climate impacts of the Southern Annular Mode". In: *Geophysical Research Letters* 33.23, p. L23704. DOI: 10.1029/2006GL027721. eprint: https://agupubs.onlinelibrary.wiley.com/doi/pdf/10.1029/2006GL027721 (cit. on p. 63).

Giorgi, F. (1990). "Simulation of Regional Climate Using a Limited Area Model Nested in a General Circulation Model". In: *Journal of Climate* 3.9, pp. 941–963. DOI: 10.1175/1520-0442(1990)003<0941:SORCUA>2.0.CO;2 (cit. on pp. 81, 85).

Giorgi, F., Jones, C., and Asrar, G. (2008). "Addressing climate information needs at the regional level: The CORDEX framework". In: 53 (cit. on p. 74).

Gleick, P. H. (1986). "Methods for evaluating the regional hydrologic impacts of global climatic changes". In: *Journal of Hydrology* 88.1, pp. 97–116. ISSN: 0022-1694. DOI: https://doi.org/10.1016/0022-1694(86)90199-X (cit. on p. 93).

Goh, K.-I., Oh, E., Jeong, H., Kahng, B., and Kim, D. (2002). "Classification of scale-free networks". In: *Proceedings of the National Academy of Sciences* 99.20, pp. 12583–12588. ISSN: 0027-8424. DOI: 10.1073/pnas.202301299 (cit. on p. 9).

Goyette, S., McFarlane, N., and Flato, G. M. (2000). "Application of the Canadian regional climate model to the Laurentian great lakes region: Implementation of a lake model". In: *Atmosphere-Ocean* 38.3, pp. 481–503. DOI: 10.1080/07055900.2000.9649657 (cit. on p. 74).

Grotch, S. L. and MacCracken, M. C. (1991). "The Use of General Circulation Models to Predict Regional Climatic Change". In: *Journal of Climate* 4.3, pp. 286–303. DOI: 10.1175/1520-0442(1991)004<0286:TUOGCM>2.0.CO;2 (cit. on p. 80).

Gu, D. and Philander, S. G. H. (1997). "Interdecadal Climate Fluctuations That Depend on Exchanges Between the Tropics and Extratropics". In: *Science* 275.5301, pp. 805–807. ISSN: 0036-8075. DOI: 10.1126/science.275.5301.805 (cit. on p. 36).

Gupta and Ambika (2018). "Role of time scales and topology on the dynamics of complex networks". In: *arXiv e-prints*, arXiv:1810.00687 (cit. on p. 69).

Handorf, D. and Dethloff, K. (2012). "How well do state-of-the-art atmosphere-ocean general circulation models reproduce atmospheric teleconnection patterns?" In: *Tellus A: Dynamic Meteorology and Oceanography* 64.1, p. 19777. DOI: 10.3402/tellusa.v64i0.19777 (cit. on pp. 18, 19).

Hannachi, A., Jolliffe, I. T., and Stephenson, D. B. (2007). "Empirical orthogonal functions and related techniques in atmospheric science: A review". In: *International Journal of Climatology* 27.9, pp. 1119–1152. DOI: 10.1002/joc.1499 (cit. on p. 9).

Hartmann, D. L. (2015). *Global physical climatology*. Vol. 103. Newnes (cit. on pp. 29, 41).

Hay, L. E., Wilby, R. L., and Leavesley, G. H. (2000). "A COMPARISON OF DELTA CHANGE AND DOWNSCALED GCM SCENARIOS FOR THREE MOUNTAINOUS BASINS IN THE UNITED STATES1". In: *JAWRA Journal of the American Water Resources Association* 36.2, pp. 387–397. DOI: 10.1111/j.1752-1688.2000.tb04276.x. eprint: https://onlinelibrary.wiley.com/doi/pdf/10.1111/j.1752-1688.2000.tb04276.x (cit. on p. 93).

Heitzig, J., Donges, J. F., Zou, Y., Marwan, N., and Kurths, J. (2012). "Node-weighted measures for complex networks with spatially embedded, sampled, or differently sized nodes". In: *The European Physical Journal B* 85.1, p. 38. ISSN: 1434-6028, 1434-6036. DOI: 10.1140/epjb/e2011-20678-7 (cit. on pp. 14, 16, 44, 45, 59).

Hohenegger, C., Brockhaus, P., Bretherton, C. S., and Schär, C. (2009). "The Soil Moisture–Precipitation Feedback in Simulations with Explicit and Parameterized Convection". In: *Journal of Climate* 22.19, pp. 5003–5020. DOI: 10.1175/2009JCLI2604.1 (cit. on p. 74).

Holton, J. R. (1979). *An introduction to dynamic meteorology / James R. Holton*. English. 2d ed. Academic Press New York, xii, 391 p. : ISBN: 0122543606 (cit. on p. 79).

Huang, N. E., Shen, Z., Long, S. R., Wu, M. C., Shih, H. H., Zheng, Q., Yen, N.-C., Tung, C. C., and Liu, H. H. (1998). "The empirical mode decomposition and the Hilbert spectrum for nonlinear and non-stationary time series analysis". In: *Proceedings of the Royal Society of London A: Mathematical, Physical and Engineering Sciences* 454.1971, pp. 903–995. ISSN: 1364-5021. DOI: 10.1098/rspa.1998.0193 (cit. on p. 9).

Huffman, G. J., Bolvin, D. T., Nelkin, E. J., Wolff, D. B., Adler, R. F., Gu, G., Hong, Y., Bowman, K. P., and Stocker, E. F. (2007). "The TRMM Multisatellite Precipitation Analysis (TMPA): Quasi-Global, Multiyear, Combined-Sensor Precipitation Estimates at Fine Scales". In: *Journal of Hydrometeorology* 8.1, pp. 38–55. DOI: 10.1175/JHM560.1 (cit. on p. 91).

Hurrell, Kushnir, Y., and Ottersen, G. (2003). "An overview of the North Atlantic oscillation". In: *The North Atlantic Oscillation: Climatic Significance and Environmental Impact* 134, pp. 1–35. DOI: 10.1029/134GM01 (cit. on p. 41).

Integração Nacional, M. da (2005). "Nova Delimitação do Semiárido Brasileiro". In: (cit. on p. 90).

Jaeger, E. B., Anders, I., Lüthi, D., Rockel, B., Schär, C., and Seneviratne, S. I. (2008). "Analysis of ERA40-driven CLM simulations for Europe". In: *Meteorologische Zeitschrift* 17.4, pp. 349–367. DOI: 10.1127/0941-2948/2008/0301 (cit. on p. 74).

Jajcay, Hlinka, J., Kravtsov, S., Tsonis, A. A., and Paluš, M. (2016). "Time scales of the European surface air temperature variability: The role of the 7–8 year cycle". In: *Geophysical Research Letters* 43.2, pp. 902–909. ISSN: 1944-8007. DOI: 10.1002/2015GL067325 (cit. on p. 55).

Kaiser, M. and Hilgetag, C. C. (2004). "Spatial growth of real-world networks". In: *Phys. Rev. E* 69 (3), p. 036103. DOI: 10.1103/PhysRevE.69.036103 (cit. on p. 9).

Kattenberg, A. (1996). "Climate models: Projections of future climate". In: (cit. on p. 80).

Kenyon, J. and Hegerl, G. C. (2010). "Influence of Modes of Climate Variability on Global Precipitation Extremes". In: *Journal of Climate* 23.23, pp. 6248–6262. ISSN: 0894-8755. DOI: 10.1175/2010JCLI3617.1 (cit. on p. 41).

Kistler, R., Kalnay, E., Collins, W., Saha, S., White, G., Woollen, J., Chelliah, M., Ebisuzaki, W., Kanamitsu, M., Kousky, V., Dool, H. van den, Jenne, R., and Fiorino, M. (Feb. 1, 2001). "The NCEP–NCAR 50-Year Reanalysis: Monthly Means CD-ROM and Documentation". In: *Bulletin of the American Meteorological Society* 82.2, pp. 247–268. ISSN: 0003-0007. DOI: 10.1175/1520-0477(2001)082<0247:TNNYRM>2.3.CO;2 (cit. on p. 45).

Kitaigorodsky, S. A. and Miropolsky, Y. Z. (1970). "On the theory of the open ocean active layer." In: *Fizika atmosfery i okeana* (cit. on pp. 74, 82).

Klein, S. A., Soden, B. J., and Lau, N.-C. (1999). "Remote Sea Surface Temperature Variations during ENSO: Evidence for a Tropical Atmospheric Bridge". In: *Journal of Climate* 12.4, pp. 917–932. DOI: 10.1175/1520-0442(1999)012<0917:RSSTVD>2.0.CO;2 (cit. on p. 37).

Kourzeneva, E. (2010). "External data for lake parameterization in Numerical Weather Prediction and climate modeling". In: 15, pp. 165–177 (cit. on p. 86).

Kretschmer, M., Coumou, D., Donges, J. F., and Runge, J. (2016). "Using Causal Effect Networks to Analyze Different Arctic Drivers of Midlatitude Winter Circulation". In: *Journal of Climate* 29.11, pp. 4069–4081. DOI: 10.1175/JCLI-D-15-0654.1. eprint: https://doi.org/10.1175/JCLI-D-15-0654.1 (cit. on p. 20).

Lange, S., Rockel, B., Volkholz, J., and Bookhagen, B. (2015). "Regional climate model sensitivities to parametrizations of convection and non-precipitating subgrid-scale clouds over South America". In: *Climate Dynamics* 44.9, pp. 2839–2857. ISSN: 1432-0894. DOI: 10.1007/s00382-014-2199-0 (cit. on p. 74).

Lanzante, J. R. (1996). "Lag Relationships Involving Tropical Sea Surface Temperatures". In: *Journal of Climate* 9.10, pp. 2568–2578. DOI: 10.1175/1520-0442(1996)009<2568:LRITSS>2.0.CO;2 (cit. on p. 37).

Latif, M., Anderson, D., Barnett, T., Cane, M., Kleeman, R., Leetmaa, A., O'Brien, J., Rosati, A., and Schneider, E. (1998). "A review of the predictability and prediction of ENSO". In: *Journal of Geophysical Research: Oceans* 103.C7, pp. 14375–14393. DOI: 10.1029/97JC03413 (cit. on p. 36).

Latif, M. and Barnett, T. P. (1996). "Decadal Climate Variability over the North Pacific and North America: Dynamics and Predictability". In: *Journal of Climate* 9.10, pp. 2407–2423. DOI: 10.1175/1520-0442(1996)009<2407:DCVOTN>2.0.CO;2 (cit. on p. 36).

Lau and Weng, H. (1995). "Climate Signal Detection Using Wavelet Transform: How to Make a Time Series Sing". In: *Bulletin of the American Meteorological Society* 76.12, pp. 2391–2402. DOI: 10.1175/1520-0477(1995)076<2391:CSDUWT>2.0.CO;2. eprint: https://doi.org/10.1175/1520-0477(1995)076<2391:CSDUWT>2.0.CO;2 (cit. on p. 55).

Lazier, J. R. (1988). "Temperature and salinity changes in the deep Labrador Sea, 1962–1986". In: *Deep Sea Research Part A. Oceanographic Research Papers* 35.8, pp. 1247–1253. ISSN: 0198-0149. DOI: https://doi.org/10.1016/0198-0149(88)90080-5 (cit. on p. 37).

Linkin and Nigam (2008). "The North Pacific Oscillation–West Pacific Teleconnection Pattern: Mature-Phase Structure and Winter Impacts". In: *Journal of Climate* 21.9, pp. 1979–1997. DOI: 10.1175/2007JCLI2048.1. eprint: https://doi.org/10.1175/2007JCLI2048.1 (cit. on p. 63).

Liu, X.-D., Osher, S., and Chan, T. (1994). "Weighted Essentially Non-oscillatory Schemes". In: *Journal of Computational Physics* 115.1, pp. 200–212. ISSN: 0021-9991. DOI: https://doi.org/10.1006/jcph.1994.1187 (cit. on p. 86).

Ljungemyr, P., Gustafsson, N., and Omstedt, A. (1996). "Parameterization of lake thermodynamics in a high-resolution weather forecasting model". In: *Tellus A* 48.5, pp. 608–621. DOI: 10.1034/j.1600-0870.1996.t01-4-00002.x (cit. on p. 74).

Lorenz, E. N. (1963). "Deterministic Nonperiodic Flow". In: *Journal of the Atmospheric Sciences* 20.2, pp. 130–141. DOI: 10.1175/1520-0469(1963)020<0130:DNF>2.0.CO;2. eprint: https://doi.org/10.1175/1520-0469(1963)020<0130:DNF>2.0.CO;2 (cit. on p. 78).

Lorenzo, D., Liguori, Schneider, N., Furtado, J. C., Anderson, B. T., and Alexander, M. A. (2015). "ENSO and meridional modes: A null hypothesis for Pacific climate variability". In: *Geophysical Research Letters* 42.21, pp. 9440–9448. DOI: 10.1002/2015GL066281. eprint: https://agupubs.onlinelibrary.wiley.com/doi/pdf/10.1002/2015GL066281 (cit. on p. 62).

Losada, Rodríguez-Fonseca, Janicot, Gervois, Chauvin, and Ruti (2010). "A multi-model approach to the Atlantic Equatorial mode: impact on the West African monsoon". In: *Climate Dynamics* 35.1, pp. 29–43. ISSN: 1432-0894. DOI: 10.1007/s00382-009-0625-5 (cit. on p. 64).

Lübbecke, Rodríguez-Fonseca, Richter, I., Martín-Rey, M., Losada, T., Polo, I., and Keenlyside, N. S. (2018). "Equatorial Atlantic variability—Modes, mechanisms, and global teleconnections". In: *Wiley Interdisciplinary Reviews: Climate Change*

9.4, e527. DOI: 10.1002/wcc.527. eprint: https://onlinelibrary.wiley.com/doi/pdf/10.1002/wcc.527 (cit. on p. 64).

Ludescher, J., Gozolchiani, A., Bogachev, M. I., Bunde, A., Havlin, S., and Schellnhuber, H. J. (2014). "Very early warning of next El Niño". In: *Proceedings of the National Academy of Sciences* 111.6, pp. 2064–2066. ISSN: 0027-8424, 1091-6490. DOI: 10.1073/pnas.1323058111 (cit. on p. 10).

Maheswaran, R. and Khosa, R. (2012). "Comparative study of different wavelets for hydrologic forecasting". In: *Computers Geosciences* 46, pp. 284–295. ISSN: 0098-3004. DOI: https://doi.org/10.1016/j.cageo.2011.12.015 (cit. on p. 28).

Maheswaran, R., Rakesh, K., Jan, A., Ch., S., G., P., Jatin, A., and Boini, N. (2014). "Wavelet-based multiscale performance analysis: An approach to assess and improve hydrological models". English (US). In: *Water Resources Research* 50.12, pp. 9721–9737. ISSN: 0043-1397. DOI: 10.1002/2013WR014650 (cit. on p. 57).

Malik, N., Bookhagen, B., Marwan, N., and Kurths, J. (2012). "Analysis of spatial and temporal extreme monsoonal rainfall over South Asia using complex networks". In: *Climate Dynamics* 39.3, pp. 971–987. ISSN: 0930-7575, 1432-0894. DOI: 10.1007/s00382-011-1156-4 (cit. on p. 10).

Manabe, S. and Bryan, K. (1969). "Climate Calculations with a Combined Ocean-Atmosphere Model". In: *Journal of the Atmospheric Sciences* 26.4, pp. 786–789. DOI: 10.1175/1520-0469(1969)026<0786:CCWACO>2.0.CO;2 (cit. on p. 30).

Mann, M. E. and Park, J. (1996). "joint Spatiotemporal Modes of Surface Temperature and Sea Level Pressure Variability in the Northern Hemisphere during the Last Century". In: *Journal of Climate* 9.9, pp. 2137–2162. DOI: 10.1175/1520-0442(1996)009<2137:JSMOST>2.0.CO;2 (cit. on p. 37).

Mantua and Hare (2002). "The Pacific Decadal Oscillation". In: *Journal of Oceanography* 58.1, pp. 35–44. ISSN: 1573-868X. DOI: 10.1023/A:1015820616384 (cit. on p. 60).

March, T., Chapman, S., and Dendy, R. (2005). "Recurrence plot statistics and the effect of embedding". In: *Physica D: Nonlinear Phenomena* 200.1, pp. 171–184. ISSN: 0167-2789. DOI: https://doi.org/10.1016/j.physd.2004.11.002 (cit. on p. 9).

Marengo, J. A. (2010). "Vulnerabilidade, impactos e adaptação à mudança do clima no semi-árido do Brasil". pt. In: *Parcerias Estratégicas* 13.27, pp. 149–176. ISSN: 2176-9729 (cit. on p. 90).

Marengo, J. A., Ambrizzi, T., Rocha, R. P. da, Alves, L. M., Cuadra, S. V., Valverde, M. C., Torres, R. R., Santos, D. C., and Ferraz, S. E. T. (2010). "Future change of climate in South America in the late twenty-first century: intercomparison of scenarios from three regional climate models". In: *Climate Dynamics* 35.6, pp. 1073–1097. ISSN: 1432-0894. DOI: 10.1007/s00382-009-0721-6 (cit. on p. 75).

Marengo, J. A., Chou, S. C., Kay, G., Alves, L. M., Pesquero, J. F., Soares, W. R., Santos, D. C., Lyra, A. A., Sueiro, G., Betts, R., Chagas, D. J., Gomes, J. L., Bustamante, J. F., and Tavares, P. (2012). "Development of regional future climate

change scenarios in South America using the Eta CPTEC/HadCM3 climate change projections: climatology and regional analyses for the Amazon, São Francisco and the Paraná River basins". In: *Climate Dynamics* 38.9, pp. 1829–1848. ISSN: 1432-0894. DOI: 10.1007/s00382-011-1155-5 (cit. on p. 75).

Martin, E. A., Paczuski, M., and Davidsen, J. (2013). "Interpretation of link fluctuations in climate networks during El Niño periods". In: *EPL (Europhysics Letters)* 102.4, p. 48003. ISSN: 0295-5075. DOI: 10.1209/0295-5075/102/48003 (cit. on p. 10).

Marwan, N., Kurths, J., and Saparin, P. (2007a). "Generalised recurrence plot analysis for spatial data". In: *Physics Letters A* 360.4, pp. 545–551. ISSN: 0375-9601. DOI: https://doi.org/10.1016/j.physleta.2006.08.058 (cit. on p. 9).

Marwan, N., Romano, M. C., Thiel, M., and Kurths, J. (2007b). "Recurrence plots for the analysis of complex systems". In: *Physics Reports* 438.5, pp. 237–329. ISSN: 0370-1573. DOI: https://doi.org/10.1016/j.physrep.2006.11.001 (cit. on p. 9).

McCreary, J. P. and Lu, P. (1994). "Interaction between the Subtropical and Equatorial Ocean Circulations: The Subtropical Cell". In: *Journal of Physical Oceanography* 24.2, pp. 466–497. ISSN: 0022-3670. DOI: 10.1175/1520-0485(1994)024<0466:IBTSAE>2.0.CO;2 (cit. on p. 36).

McGregor, P. K. (2005). *Animal Communication Networks*. Cambridge University Press. DOI: 10.1017/CBO9780511610363 (cit. on p. 9).

Melo, E., Correia, M., and Aragão, M. (2015). "Expansão da Agricultura Irrigada e Mudanças nos Processos de Interação Superfície-Atmosfera: Um Estudo Numérico de Impacto Ambiental em Áreas de Caatinga." In: *Revista Brasileira de Geografia Física* (cit. on p. 75).

Mironov, D., Rdmann Heise, E., Katerina Kourzeneva, E., Ritter, B., and Atalia, N. (2008). "Parameterisation of Lakes in Numerical Weather Prediction and Climate Models". In: (cit. on pp. 73, 74, 82–85).

Mohino and Losada (2015). "Impacts of the Atlantic Equatorial Mode in a warmer climate". In: *Climate Dynamics* 45.7, pp. 2255–2271. ISSN: 1432-0894. DOI: 10.1007/s00382-015-2471-y (cit. on p. 64).

Namias, J. (1969). "Seasonal interaction between the north Pacific Ocean and the atmosphere during the 1960's". In: *Monthly Weather Review* 97.3, pp. 173–192. DOI: 10.1175/1520-0493(1969)097<0173:SIBTNP>2.3.CO;2 (cit. on p. 31).

Neelin, J. D., Latif, M., and Jin, F. (1994). "Dynamics of Coupled Ocean-Atmosphere Models: The Tropical Problem". In: *Annual Review of Fluid Mechanics* 26.1, pp. 617–659. DOI: 10.1146/annurev.fl.26.010194.003153 (cit. on p. 36).

Newman (2003). "The Structure and Function of Complex Networks". In: *SIAM Review* 45.2, pp. 167–256. ISSN: 0036-1445. DOI: 10.1137/S003614450342480 (cit. on pp. 9, 13, 14, 16, 44).

– (2010). *Networks: An Introduction*. Oxford University Press. 789 pp. ISBN: 978-0-19-920665-0 (cit. on p. 9).

Newman and Girvan, M. (2004). "Finding and evaluating community structure in networks". In: *Physical Review E* 69.2. ISSN: 1539-3755, 1550-2376. DOI: 10.1103/PhysRevE.69.026113 (cit. on pp. 45, 46).

Newman and Park, J. (2003). "Why social networks are different from other types of networks". In: *Phys. Rev. E* 68 (3), p. 036122. DOI: 10.1103/PhysRevE.68.036122 (cit. on p. 9).

Nicolini, M., Salio, P., Katzfey, J. J., McGregor, J. L., and Saulo, A. C. (2002). "January and July regional climate simulation over South America". In: *Journal of Geophysical Research: Atmospheres* 107.D22. DOI: 10.1029/2001JD000736 (cit. on p. 75).

Nikulin, G., Jones, C., Giorgi, F., Asrar, G., Büchner, M., Cerezo-Mota, R., Christensen, O. B., Déqué, M., Fernandez, J., Hänsler, A., Meijgaard, E. van, Samuelsson, P., Sylla, M. B., and Sushama, L. (2012). "Precipitation Climatology in an Ensemble of CORDEX-Africa Regional Climate Simulations". In: *Journal of Climate* 25.18, pp. 6057–6078. DOI: 10.1175/JCLI-D-11-00375.1 (cit. on p. 74).

Oreskes, N. (1998). "Evaluation (not validation) of quantitative models." In: *Environmental Health Perspectives* 106.Suppl 6, pp. 1453–1460. ISSN: 0091-6765 (cit. on p. 88).

Paluš (2014). "Multiscale Atmospheric Dynamics: Cross-Frequency Phase-Amplitude Coupling in the Air Temperature". In: *Phys. Rev. Lett.* 112 (7), p. 078702. DOI: 10.1103/PhysRevLett.112.078702 (cit. on p. 55).

– (2018). "Linked by Dynamics: Wavelet-Based Mutual Information Rate as a Connectivity Measure and Scale-Specific Networks". In: *Advances in Nonlinear Geosciences*. Ed. by Tsonis. Springer International Publishing, pp. 427–463. ISBN: 978-3-319-58894-0 (cit. on p. 55).

Paluš, M., Hartman, D., Hlinka, J., and Vejmelka, M. (2011). "Discerning connectivity from dynamics in climate networks". In: *Nonlinear Processes in Geophysics* 18.5, pp. 751–763. DOI: 10.5194/npg-18-751-2011 (cit. on p. 10).

Paluš, Hartman, Hlinka, and Vejmelka (2011). "Discerning connectivity from dynamics in climate networks". In: *Nonlin. Processes Geophys.* 18.5, pp. 751–763. ISSN: 1607-7946. DOI: 10.5194/npg-18-751-2011 (cit. on pp. 10, 20).

Penven, P., Echevin, V., Pasapera, J., Colas, F., and Tam, J. (2005). "Average circulation, seasonal cycle, and mesoscale dynamics of the Peru Current System: A modeling approach". In: *Journal of Geophysical Research: Oceans* 110.C10. DOI: 10.1029/2005JC002945 (cit. on p. 32).

Percival, D. B. (2008). "Analysis of Geophysical Time Series Using Discrete Wavelet Transforms: An Overview". In: *Nonlinear Time Series Analysis in the Geosciences: Applications in Climatology, Geodynamics and Solar-Terrestrial Physics*. Ed. by R. V. Donner and S. M. Barbosa. Berlin, Heidelberg: Springer Berlin Heidelberg, pp. 61–79. ISBN: 978-3-540-78938-3. DOI: 10.1007/978-3-540-78938-3_4 (cit. on pp. 27, 57).

Percival, D. B. and Walden, A. T. (2000). *Wavelet Methods for Time Series Analysis*. Cambridge Series in Statistical and Probabilistic Mathematics. Cambridge University Press. DOI: 10.1017/CBO9780511841040 (cit. on pp. 22–28).

Perinelli, Chiari, and Ricci (2018). "Correlation in brain networks at different time scale resolution". In: *Chaos* 28.6, p. 063127. DOI: 10.1063/1.5025242 (cit. on p. 69).

Phillips, N. A. and Shukla, J. (1973). "On the Strategy of Combining Coarse and Fine Grid Meshes in Numerical Weather Prediction". In: *Journal of Applied Meteorology* 12.5, pp. 763–770. DOI: 10.1175/1520-0450(1973)012<0763:OTSOCC>2.0.CO;2 (cit. on p. 85).

Pielke, R. A. (1974). "A Three-Dimensional Numerical Model of the Sea Breezes Over South Florida". In: *Monthly Weather Review* 102.2, pp. 115–139. DOI: 10.1175/1520-0493(1974)102<0115:ATDNMO>2.0.CO;2 (cit. on p. 73).

– (2002). *Mesoscale Meteorological Modeling*. en. Google-Books-ID: p815Jhdzfp4C. Academic Press. ISBN: 978-0-12-554766-6 (cit. on p. 73).

Pierce, D. W., Barnett, T. P., and Latif, M. (2000). "Connections between the Pacific Ocean Tropics and Midlatitudes on Decadal Timescales". In: *Journal of Climate* 13.6, pp. 1173–1194. DOI: 10.1175/1520-0442(2000)013<1173:CBTPOT>2.0.CO;2 (cit. on p. 38).

Power, S., Casey, T., Folland, C., Colman, A., and Mehta, V. (1999). "Inter-decadal modulation of the impact of ENSO on Australia". In: *Climate Dynamics* 15.5, pp. 319–324. ISSN: 0930-7575, 1432-0894. DOI: 10.1007/s003820050284 (cit. on p. 41).

Qiu, Cai, Guo, X., and Ng, B. (2014). "The asymmetric influence of the positive and negative IOD events on China's rainfall". en. In: *Scientific Reports* 4, p. 4943. ISSN: 2045-2322. DOI: 10.1038/srep04943 (cit. on p. 63).

Radebach, A., Donner, R. V., Runge, J., Donges, J. F., and Kurths, J. (2013). "Disentangling different types of El Niño episodes by evolving climate network analysis". In: *Physical Review E* 88.5, p. 052807. DOI: 10.1103/PhysRevE.88.052807 (cit. on pp. 10, 18–20, 52, 59).

Raphael, Marshall, Turner, J., Fogt, R. L., Schneider, D., Dixon, D. A., Hosking, J. S., Jones, J. M., and Hobbs, W. R. (2016). "The Amundsen Sea Low: Variability, Change, and Impact on Antarctic Climate". In: *Bulletin of the American Meteorological Society* 97.1, pp. 111–121. DOI: 10.1175/BAMS-D-14-00018.1. eprint: https://doi.org/10.1175/BAMS-D-14-00018.1 (cit. on p. 63).

Raschendorfer, M. (2001). "The new turbulence parameterization of LM". In: 1, pp. 89–97 (cit. on p. 87).

Rasmusson, E. M. and Carpenter, T. H. (1982). "Variations in Tropical Sea Surface Temperature and Surface Wind Fields Associated with the Southern Oscillation/El Niño". In: *Monthly Weather Review* 110.5, pp. 354–384. ISSN: 0027-0644. DOI: 10.1175/1520-0493(1982)110<0354:VITSST>2.0.CO;2 (cit. on p. 41).

Rasmusson, E. M. and Wallace, J. M. (1983). "Meteorological Aspects of the El Niño/Southern Oscillation". In: *Science* 222.4629, pp. 1195–1202. ISSN: 0036-8075, 1095-9203. DOI: 10.1126/science.222.4629.1195 (cit. on p. 41).

Reason (2001). "Subtropical Indian Ocean SST dipole events and southern African rainfall". In: *Geophysical Research Letters* 28.11, pp. 2225–2227. DOI: 10.1029/2000GL012735. eprint: https://agupubs.onlinelibrary.wiley.com/doi/pdf/10.1029/2000GL012735 (cit. on p. 63).

Risbey, Pook, McIntosh, P. C., Wheeler, M. C., and Hendon, H. H. (2009). "On the Remote Drivers of Rainfall Variability in Australia". In: *Monthly Weather*

Review 137.10, pp. 3233–3253. DOI: 10.1175/2009MWR2861.1. eprint: https://doi.org/10.1175/2009MWR2861.1 (cit. on p. 63).

Ritter, B. and Geleyn, J.-F. (1992). "A Comprehensive Radiation Scheme for Numerical Weather Prediction Models with Potential Applications in Climate Simulations". In: *Monthly Weather Review* 120.2, pp. 303–325. DOI: 10.1175/1520-0493(1992)120<0303:ACRSFN>2.0.CO;2 (cit. on p. 87).

Rockel, B., Will, A., and Hense, A. (2008). "The Regional Climate Model COSMO-CLM (CCLM)". In: *Meteorologische Zeitschrift* 17.4, pp. 347–348. DOI: 10.1127/0941-2948/2008/0309 (cit. on pp. 73, 75).

Rodwell, M. (2002). "Atlantic air-sea interaction revisited". In: *Meteorology at the Millennium*. Ed. by R. Pearce. Vol. 83. International Geophysics. Academic Press, pp. 185–197. DOI: https://doi.org/10.1016/S0074-6142(02)80167-X (cit. on p. 31).

Rogers and Loon, van (1982). "Spatial Variability of Sea Level Pressure and 500 mb Height Anomalies over the Southern Hemisphere". In: *Monthly Weather Review* 110.10, pp. 1375–1392. DOI: 10.1175/1520-0493(1982)110<1375:SVOSLP>2.0.CO;2. eprint: https://doi.org/10.1175/1520-0493(1982)110<1375:SVOSLP>2.0.CO;2 (cit. on p. 63).

Ropelewski, C. F. and Halpert, M. S. (1986). "North American Precipitation and Temperature Patterns Associated with the El Niño/Southern Oscillation (ENSO)". In: *Monthly Weather Review* 114.12, pp. 2352–2362. ISSN: 0027-0644. DOI: 10.1175/1520-0493(1986)114<2352:NAPATP>2.0.CO;2 (cit. on p. 41).

Runge, J., Heitzig, J., Marwan, N., and Kurths, J. (2012a). "Quantifying causal coupling strength: A lag-specific measure for multivariate time series related to transfer entropy". In: *Phys. Rev. E* 86 (6), p. 061121. DOI: 10.1103/PhysRevE.86.061121 (cit. on pp. 10, 20).

Runge, J., Heitzig, J., Petoukhov, V., and Kurths, J. (2012b). "Escaping the Curse of Dimensionality in Estimating Multivariate Transfer Entropy". In: *Phys. Rev. Lett.* 108 (25), p. 258701. DOI: 10.1103/PhysRevLett.108.258701 (cit. on p. 10).

Runge, J., Petoukhov, V., Donges, J. F., Hlinka, J., Jajcay, N., Vejmelka, M., Hartman, D., Marwan, N., Paluš, M., and Kurths, J. (2015). "Identifying causal gateways and mediators in complex spatio-temporal systems". en. In: *Nature Communications* 6, p. 8502. ISSN: 2041-1723. DOI: 10.1038/ncomms9502 (cit. on pp. 10, 20).

Runge, J., Petoukhov, V., and Kurths, J. (2014). "Quantifying the Strength and Delay of Climatic Interactions: The Ambiguities of Cross Correlation and a Novel Measure Based on Graphical Models". In: *Journal of Climate* 27.2, pp. 720–739. DOI: 10.1175/JCLI-D-13-00159.1 (cit. on p. 10).

Saji, N. H., Goswami, B. N., Vinayachandran, P. N., and Yamagata, T. (1999). "A dipole mode in the tropical Indian Ocean". In: *Nature* 401.6751, pp. 360–363. ISSN: 1476-4687. DOI: 10.1038/43854 (cit. on pp. 35, 63).

Scaife, A. A., Folland, C. K., Alexander, L. V., Moberg, A., and Knight, J. R. (2008). "European Climate Extremes and the North Atlantic Oscillation". In: *Journal of*

Climate 21.1, pp. 72–83. ISSN: 0894-8755. DOI: 10.1175/2007JCLI1631.1 (cit. on p. 41).

Schreiber, T. and Schmitz, A. (2000). "Surrogate Time Series". In: *Phys. D* 142.3-4, pp. 346–382. ISSN: 0167-2789. DOI: 10.1016/S0167-2789(00)00043-9 (cit. on p. 20).

Schrodin R.; Heise, E. (2001). *The Multi-Layer Version of the DWD Soil Model TERRA-LM*. Tech. rep. Consortium for Small-Scale Modelling (COSMO): Offenbach, Germany, (cit. on p. 87).

Sengupta, D., Goswami, B. N., and Senan, R. (2012). "Coherent intraseasonal oscillations of ocean and atmosphere during the Asian Summer Monsoon". In: *Geophysical Research Letters* 28.21, pp. 4127–4130. DOI: 10.1029/2001GL013587 (cit. on p. 36).

Seth, A. and Rojas, M. (2003). "Simulation and Sensitivity in a Nested Modeling System for South America. Part I: Reanalyses Boundary Forcing". In: *Journal of Climate* 16.15, pp. 2437–2453. DOI: 10.1175/1520-0442(2003)016<2437:SASIAN>2.0.CO;2 (cit. on p. 75).

Shin and An (2018). "Interdecadal Change in the Relationship Between the North Pacific Oscillation and the Pacific Meridional Mode and Its Impact on ENSO". In: *Asia-Pacific Journal of Atmospheric Sciences* 54.1, pp. 63–76. ISSN: 1976-7951. DOI: 10.1007/s13143-017-0060-1 (cit. on p. 63).

Singhrattna, Rajagopalan, Clark, M., and Krishna Kumar, K. (2005). "Seasonal forecasting of Thailand summer monsoon rainfall". In: *International Journal of Climatology* 25.5, pp. 649–664. DOI: 10.1002/joc.1144. eprint: https://rmets.onlinelibrary.wiley.com/doi/pdf/10.1002/joc.1144 (cit. on p. 63).

Smith, T. M., Reynolds, R. W., Peterson, T. C., and Lawrimore, J. (2008). "Improvements to NOAA's Historical Merged Land–Ocean Surface Temperature Analysis (1880–2006)". In: *Journal of Climate* 21.10, pp. 2283–2296. DOI: 10.1175/2007JCLI2100.1 (cit. on p. 42).

Solman, S. A., Sanchez, E., Samuelsson, P., Rocha, R. P. da, Li, L., Marengo, J., Pessacg, N. L., Remedio, A. R. C., Chou, S. C., Berbery, H., Le Treut, H., Castro, M. de, and Jacob, D. (2013). "Evaluation of an ensemble of regional climate model simulations over South America driven by the ERA-Interim reanalysis: model performance and uncertainties". In: *Climate Dynamics* 41.5, pp. 1139–1157. ISSN: 1432-0894. DOI: 10.1007/s00382-013-1667-2 (cit. on p. 75).

Sporns, O., Tononi, G., and Kötter, R. (2005). "The Human Connectome: A Structural Description of the Human Brain". In: *PLOS Computational Biology* 1.4. DOI: 10.1371/journal.pcbi.0010042 (cit. on p. 9).

Steinhaeuser, K., Chawla, N. V., and Ganguly, A. R. (2010). "An Exploration of Climate Data Using Complex Networks". In: *SIGKDD Explor. Newsl.* 12.1, pp. 25–32. ISSN: 1931-0145. DOI: 10.1145/1882471.1882476 (cit. on p. 10).

Stensrud, D. (2009). *Parameterization Schemes: Keys to Understanding Numerical Weather Prediction Models*. Cambridge University Press. ISBN: 9781107469655 (cit. on pp. 81, 82).

Stolbova, V., Martin, P., Bookhagen, B., Marwan, N., and Kurths, J. (2014). "Topology and seasonal evolution of the network of extreme precipitation over the Indian subcontinent and Sri Lanka". In: *Nonlin. Processes Geophys.* 21.4, pp. 901–917. ISSN: 1607-7946. DOI: 10.5194/npg-21-901-2014 (cit. on p. 10).

Strogatz, S. H. (Mar. 2001). "Exploring complex networks". In: *Nature* 410, 268 EP - (cit. on p. 9).

Su, H., Neelin, J. D., and Meyerson, J. E. (2013). "Tropical Tropospheric Temperature and Precipitation Response to Sea Surface Temperature Forcing". In: *Earth's Climate*. American Geophysical Union (AGU), pp. 379–392. ISBN: 9781118665947. DOI: 10.1029/147GM21 (cit. on p. 38).

Sun, W., Lin, B., Baize, R. R., Videen, G., and Hu, Y. (2014). "Sensing Hadley cell with space-borne lidar". In: *Journal of Quantitative Spectroscopy and Radiative Transfer* 148, pp. 38–41. ISSN: 0022-4073. DOI: https://doi.org/10.1016/j.jqsrt.2014.06.017 (cit. on p. 33).

Takayabu, Y. N., Iguchi, T., Kachi, M., Shibata, A., and Kanzawa, H. (1999). "Abrupt termination of the 1997-98 El Niño in response to a Madden-Julian oscillation". In: *Nature* 402, p. 279 (cit. on p. 38).

Tamsalu, R., Malkki, P., and Myrberg, K. (1998). "Self-similarity concept in marine system modelling". English. In: *Oceanographic Literature Review* 45.3, p. 430 (cit. on p. 84).

Tantet and Dijkstra (2014). "An interaction network perspective on the relation between patterns of sea surface temperature variability and global mean surface temperature". In: *Earth System Dynamics* 5.1, pp. 1–14. DOI: 10.5194/esd-5-1-2014 (cit. on p. 46).

The Walker Circulation: ENSO's atmospheric buddy | NOAA Climate.gov (2018) (cit. on p. 34).

Thiery, W., Martynov, A., Darchambeau, F., Descy, J.-P., Plisnier, P.-D., Sushama, L., and Lipzig, N. P. M. van (2014). "Understanding the performance of the FLake model over two African Great Lakes". In: *Geoscientific Model Development* 7.1, pp. 317–337. DOI: 10.5194/gmd-7-317-2014 (cit. on p. 73).

Tirabassi, G., Masoller, C., and Barreiro, M. (2014). "A study of the air–sea interaction in the South Atlantic Convergence Zone through Granger causality". In: *International Journal of Climatology* 35.12, pp. 3440–3453. DOI: 10.1002/joc.4218 (cit. on p. 11).

Torrence, C. and Compo, G. P. (1998a). "A Practical Guide to Wavelet Analysis". In: *Bulletin of the American Meteorological Society* 79.1, pp. 61–78. DOI: 10.1175/1520-0477(1998)079<0061:APGTWA>2.0.CO;2 (cit. on p. 9).

– (1998b). "A Practical Guide to Wavelet Analysis". In: *Bulletin of the American Meteorological Society* 79.1, pp. 61–78. DOI: 10.1175/1520-0477(1998)079<0061:APGTWA>2.0.CO;2 (cit. on p. 26).

Toth, Z. and Kalnay, E. (1997). "Ensemble Forecasting at NCEP and the Breeding Method". In: *Monthly Weather Review* 125.12, pp. 3297–3319. DOI: 10.1175/1520-0493(1997)125<3297:EFANAT>2.0.CO;2. eprint: https://doi.org/10.1175/1520-0493(1997)125<3297:EFANAT>2.0.CO;2 (cit. on p. 78).

Tourre, Y. M. and White, W. B. (1995). "ENSO Signals in Global Upper-Ocean Temperature". In: *Journal of Physical Oceanography* 25.6, pp. 1317–1332. DOI: 10.1175/1520-0485(1995)025<1317:ESIGUO>2.0.CO;2 (cit. on p. 37).

Trenberth and Hurrell (1994). "Decadal atmosphere-ocean variations in the Pacific". In: *Climate Dynamics* 9.6, pp. 303–319 (cit. on pp. 11, 30).

Tsonis, A. A. and Roebber, P. J. (2004). "The architecture of the climate network". In: *Physica A: Statistical Mechanics and its Applications* 333, pp. 497–504. ISSN: 0378-4371. DOI: 10.1016/j.physa.2003.10.045 (cit. on pp. 9, 19, 20).

Tsonis, A. A. and Swanson, K. L. (2012). "Review article "On the origins of decadal climate variability: a network perspective"". In: *Nonlinear Processes in Geophysics* 19.5, pp. 559–568. DOI: 10.5194/npg-19-559-2012 (cit. on p. 42).

Tsonis, A. A. and Swanson, K. L. (2008). "Topology and Predictability of El Niño and La Niña Networks". In: *Physical Review Letters* 100.22, p. 228502. DOI: 10.1103/PhysRevLett.100.228502 (cit. on p. 10).

Tsonis, A. A., Swanson, K. L., and Roebber, P. J. (2006). "What Do Networks Have to Do with Climate?" In: *Bulletin of the American Meteorological Society* 87.5, pp. 585–596. ISSN: 0003-0007. DOI: 10.1175/BAMS-87-5-585 (cit. on pp. 17, 19, 20, 45, 59).

Tsonis, A. A., Wang, G., Swanson, K. L., Rodrigues, F. A., and Costa, L. D. F. (2011). "Community structure and dynamics in climate networks". In: *Climate Dynamics* 37, pp. 933–940. ISSN: 0930-7575. DOI: 10.1007/s00382-010-0874-3 (cit. on pp. 19, 45).

Tsuang, B.-J., Tu, C., and Arpe, K. (2001). *Lake parameterization for climate models*. eng. Vol. 316. Hamburg: Max-Planck-Institut für Meteorologie. DOI: 10.17617/2.2603625 (cit. on p. 74).

Unesco (1974). *FAO-Unesco Soil Map of the World: 1:5 000 000* (cit. on p. 88).

Vecchi, G. A., Xie, S.-P., and Fischer, A. S. (2004). "Ocean–Atmosphere Covariability in the Western Arabian Sea". In: *Journal of Climate* 17.6, pp. 1213–1224. DOI: 10.1175/1520-0442(2004)017<1213:OCITWA>2.0.CO;2 (cit. on p. 36).

Viterbo, P. (2002 2002). *A review of parametrization schemes for land surface processes* (cit. on p. 82).

Von Storch, H., Zorita, E., and Cubasch, U. (1993). "Downscaling of Global Climate Change Estimates to Regional Scales: An Application to Iberian Rainfall in Wintertime". In: *Journal of Climate* 6.6, pp. 1161–1171. DOI: 10.1175/1520-0442(1993)006<1161:DOGCCE>2.0.CO;2 (cit. on p. 80).

Wagner, S., Fast, I., and Kaspar, F. (2012). "Comparison of 20th century and pre-industrial climate over South America in regional model simulations". In: *Climate of the Past* 8.5, pp. 1599–1620. DOI: 10.5194/cp-8-1599-2012 (cit. on p. 75).

Wallace, J. M. and Gutzler, D. S. (1981). "Teleconnections in the Geopotential Height Field during the Northern Hemisphere Winter". In: *Monthly Weather Review* 109.4, pp. 784–812. DOI: 10.1175/1520-0493(1981)109<0784:TITGHF>2.0.CO;2 (cit. on p. 38).

Wang, C. and Picaut, J. (2013). "Understanding Enso Physics—A Review". In: *Earth's Climate*. American Geophysical Union (AGU), pp. 21–48. ISBN: 9781118665947. DOI: 10.1029/147GM02 (cit. on p. 32).

Wang and Chen (2014). "An Intensity Index for the East Asian Winter Monsoon". In: *Journal of Climate* 27.6, pp. 2361–2374. DOI: 10.1175/JCLI-D-13-00086.1. eprint: https://doi.org/10.1175/JCLI-D-13-00086.1 (cit. on p. 63).

Wang, Xie, and Carton (2013). "A Global Survey of Ocean–Atmosphere Interaction and Climate Variability". In: *Earth's Climate*. American Geophysical Union (AGU), pp. 1–19. ISBN: 9781118665947. DOI: 10.1029/147GM01 (cit. on pp. 31, 32, 35–37).

Warner, T. T. (1989). "Mesoscale atmospheric modeling". In: *Earth-Science Reviews* 26.1, pp. 221–251. ISSN: 0012-8252. DOI: https://doi.org/10.1016/0012-8252(89)90023-8 (cit. on p. 85).

Washington, W. M., Buja, L., and Craig, A. (2009). "The computational future for climate and Earth system models: on the path to petaflop and beyond". In: *Philosophical Transactions of the Royal Society of London A: Mathematical, Physical and Engineering Sciences* 367.1890, pp. 833–846. ISSN: 1364-503X. DOI: 10.1098/rsta.2008.0219 (cit. on p. 81).

Webster, P. J., Moore, A. M., Loschnigg, J. P., and Leben, R. R. (1999). "Coupled ocean–atmosphere dynamics in the Indian Ocean during 1997–98". In: *Nature* 401.6751, pp. 356–360. ISSN: 1476-4687. DOI: 10.1038/43848 (cit. on p. 63).

Wells, N. (2011). *The Atmosphere and Ocean: A Physical Introduction*. Advancing Weather and Climate Science. Wiley. ISBN: 9781119979845 (cit. on pp. 30–34).

Weng, H. and Lau (1994). "Wavelets, Period Doubling, and Time–Frequency Localization with Application to Organization of Convection over the Tropical Western Pacific". In: *Journal of the Atmospheric Sciences* 51.17, pp. 2523–2541. DOI: 10.1175/1520-0469(1994)051<2523:WPDATL>2.0.CO;2. eprint: https://doi.org/10.1175/1520-0469(1994)051<2523:WPDATL>2.0.CO;2 (cit. on p. 9).

Wiedermann, Donges Jonathan F., Handorf Dörthe, Kurths Jürgen, and Donner Reik V. (2016a). "Hierarchical structures in Northern Hemispheric extratropical winter ocean–atmosphere interactions". In: *International Journal of Climatology* 37.10, pp. 3821–3836. ISSN: 0899-8418. DOI: 10.1002/joc.4956 (cit. on pp. 10, 11, 19, 21, 42, 45, 59).

Wiedermann, Donges, J. F., Heitzig, J., and Kurths, J. (2013). "Node-weighted interacting network measures improve the representation of real-world complex systems". In: *EPL (Europhysics Letters)* 102.2, p. 28007 (cit. on p. 14).

Wiedermann, Radebach Alexander, Donges Jonathan F., Kurths Jürgen, and Donner Reik V. (May 27, 2016b). "A climate network-based index to discriminate different types of El Niño and La Niña". In: *Geophysical Research Letters* 43.13, pp. 7176–7185. ISSN: 0094-8276. DOI: 10.1002/2016GL069119 (cit. on p. 10).

Wiedermann, Siegmund, J. F., Donges, J. F., Kurths, J., and Donner, R. V. (2017). "Differential imprints of distinct ENSO flavors in global extreme precipitation patterns". In: *arXiv:1702.00218 [physics]* (cit. on p. 41).

Wigley, Jones, P. D., Briffa, K. R., and Smith, G. (1990). "Obtaining sub-grid-scale information from coarse-resolution general circulation model output". In: *Journal of Geophysical Research: Atmospheres* 95.D2, pp. 1943–1953. DOI: 10.1029/JD095iD02p01943 (cit. on p. 80).

Wilby (1994). "Stochastic weather type simulation for regional climate change impact assessment". In: *Water Resources Research* 30.12, pp. 3395–3403. DOI: 10.1029/94WR01840 (cit. on p. 80).

Wilby and Wigley (1997). "Downscaling general circulation model output: a review of methods and limitations". In: *Progress in Physical Geography: Earth and Environment* 21.4, pp. 530–548. DOI: 10.1177/030913339702100403 (cit. on p. 80).

Wills, Schneider, Wallace, J. M., Battisti, D. S., and Hartmann, D. L. (2018). "Disentangling Global Warming, Multidecadal Variability, and El Niño in Pacific Temperatures". In: *Geophysical Research Letters* 45.5, pp. 2487–2496. DOI: 10.1002/2017GL076327. eprint: https://agupubs.onlinelibrary.wiley.com/doi/pdf/10.1002/2017GL076327 (cit. on p. 62).

Woolnough, S. J., Slingo, J. M., and Hoskins, B. J. (2001). "The organization of tropical convection by intraseasonal sea surface temperature anomalies". In: *Quarterly Journal of the Royal Meteorological Society* 127.573, pp. 887–907 (cit. on pp. 10, 29).

Wu, Li, Wang, and Liu (2009). "Can the Southern Hemisphere annular mode affect China winter monsoon?" In: *Journal of Geophysical Research: Atmospheres* 114.D11, p. D11107. DOI: 10.1029/2008JD011501. eprint: https://agupubs.onlinelibrary.wiley.com/doi/pdf/10.1029/2008JD011501 (cit. on p. 63).

Wyrtki, K. (1973). "Teleconnections in the equatorial Pacific Ocean". In: *Science* 180.4081, pp. 66–68 (cit. on pp. 29, 41).

Xie (2004). "Satellite Observations of Cool Ocean–Atmosphere Interaction". In: *Bulletin of the American Meteorological Society* 85.2, pp. 195–208. DOI: 10.1175/BAMS-85-2-195 (cit. on pp. 30, 37).

Xie, Annamalai, H., Schott, F. A., and McCreary, J. P. (2002). "Structure and Mechanisms of South Indian Ocean Climate Variability". In: *Journal of Climate* 15.8, pp. 864–878. DOI: 10.1175/1520-0442(2002)015<0864:SAMOSI>2.0.CO;2 (cit. on p. 36).

Xie and Carton, J. A. (2013). "Tropical Atlantic Variability: Patterns, Mechanisms, and Impacts". In: *Earth's Climate*. American Geophysical Union (AGU), pp. 121–142. ISBN: 9781118665947. DOI: 10.1029/147GM07. eprint: https://agupubs.onlinelibrary.wiley.com/doi/pdf/10.1029/147GM07 (cit. on p. 35).

Xie and Philander, S. G. H. (1994). "A coupled ocean-atmosphere model of relevance to the ITCZ in the eastern Pacific". In: *Tellus A* 46.4, pp. 340–350. DOI: 10.1034/j.1600-0870.1994.t01-1-00001.x (cit. on p. 30).

Yamasaki, K., Gozolchiani, A., and Havlin, S. (2008). "Climate Networks around the Globe are Significantly Affected by El Niño". In: *Physical Review Letters* 100.22, p. 228501. DOI: 10.1103/PhysRevLett.100.228501 (cit. on pp. 9, 10).

Yeh, Cai, Min, S.-K., McPhaden, M. J., Dommenget, D., Dewitte, B., Collins, M., Ashok, K., An, S.-I., Yim, B.-Y., and Kug, J.-S. (2018). "ENSO Atmospheric Teleconnections and Their Response to Greenhouse Gas Forcing". In: *Reviews of Geophysics* 56.1, pp. 185–206. DOI: 10.1002/2017RG000568. eprint: https://agupubs.onlinelibrary.wiley.com/doi/pdf/10.1002/2017RG000568 (cit. on p. 60).

Yiu (2018). "El Niño Southern Oscillation teleconnections and their effects on the Amundsen Sea region". en. Thesis. University of Cambridge. DOI: 10.17863/CAM.23516 (cit. on p. 62).

Zahn, M. and Storch, H. von (2008). "A long-term climatology of North Atlantic polar lows". In: *Geophysical Research Letters* 35.22. DOI: 10.1029/2008GL035769 (cit. on p. 74).

Zebiak, S. E. (1993). "Air–Sea Interaction in the Equatorial Atlantic Region". In: *Journal of Climate* 6.8, pp. 1567–1586. DOI: 10.1175/1520-0442(1993)006<1567:AIITEA>2.0.CO;2 (cit. on p. 35).

Zemp, D. C., Wiedermann, M., Kurths, J., Rammig, A., and Donges, J. F. (2014). "Node-weighted measures for complex networks with directed and weighted edges for studying continental moisture recycling". In: *EPL (Europhysics Letters)* 107.5, p. 58005 (cit. on p. 15).

Zhang, D.-L., Chang, H.-R., Seaman, N. L., Warner, T. T., and Fritsch, J. M. (1986). "A Two-Way Interactive Nesting Procedure with Variable Terrain Resolution". In: *Monthly Weather Review* 114.7, pp. 1330–1339. DOI: 10.1175/1520-0493(1986)114<1330:ATWINP>2.0.CO;2 (cit. on p. 85).

Selbständigkeitserklärung

Ich erkläre, dass ich die vorliegende Arbeit selbständig und nur unter Verwendung der angegebenen Literatur und Hilfsmittel angefertigt habe.

Potsdam, den 23. September 2019 Nikoo Ekhtiari